

WRDC-TR-90-9003  
Volume VI

**UNIFORM THEORY OF DIFFRACTION  
(UTD) SCATTERING FROM STRUCTURES,  
INCLUDING HIGHER ORDER TERMS**

**Volume VI: Overview of  
Accomplishments**

ElectroScience Laboratory  
The Ohio State University  
1320 Kinnear Road  
Columbus, OH 43212

November 1990  
Final Report for Period April 1986 - December 1989

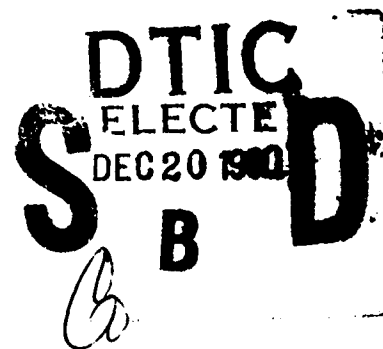
**Approved for Public Release; Distribution is Unlimited**



2

AD-A230 341

Signature Technology Directorate  
Wright Research and Development Center  
Air Force Systems Command  
Wright Patterson Air Force Base, OH 45433-6523

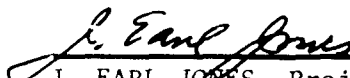


NOTICE

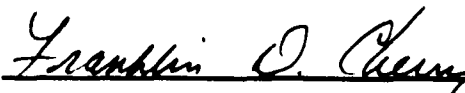
When Government drawings, specifications, or other data are used for any purpose other than in connection with a definitely Government-related procurement, the United States Government incurs no responsibility or any obligation whatsoever. The fact that the government may have formulated or in any way supplied the said drawings, specifications, or other data, is not to be regarded by implication, or otherwise in any manner construed, as licensing the holder, or any other person or corporation; or as conveying any rights or permission to manufacture, use, or sell any patented invention that may in any way be related thereto.

This report is releasable to the National Technical Information Service (NTIS). At NTIS, it will be available to the general public, including foreign nations.

This technical report has been reviewed and is approved for publication.

  
\_\_\_\_\_  
J. EARL JONES, Project Engineer  
Defensive Avionics Division  
Signature Technology Directorate  
  
FOR THE COMMANDER

  
\_\_\_\_\_  
JOSEPH C. FAISON, Chief  
Defensive Avionics Division  
Signature Technology Directorate

  
\_\_\_\_\_  
FRANKLIN D. CHERRY, Director  
Signature Technology Directorate

If your address has changed, if you wish to be removed from our mailing list, or if the addressee is no longer employed by your organization please notify WRDC/SNA, WPAFB, OH 45433-6523 to help us maintain a current mailing list.

Copies of this report should not be returned unless return is required by security considerations, contractual obligations, or notice on a specific document.

UNCLASSIFIED

SECURITY CLASSIFICATION OF THIS PAGE

REPORT DOCUMENTATION PAGE			Form Approved OMB No. 0704-0188		
1a. REPORT SECURITY CLASSIFICATION UNCLASSIFIED		1b. RESTRICTIVE MARKINGS NONE			
2a. SECURITY CLASSIFICATION AUTHORITY N/A		3. DISTRIBUTION/AVAILABILITY OF REPORT Approved for Public Release; Distribution is Unlimited			
2b. DECLASSIFICATION/DOWNGRADING SCHEDULE N/A					
4. PERFORMING ORGANIZATION REPORT NUMBER(S) 718295-16		5. MONITORING ORGANIZATION REPORT NUMBER(S) WRDC-TR-90-9003, Vol. VI			
6a. NAME OF PERFORMING ORGANIZATION Ohio State University ElectroScience Laboratory		6b. OFFICE SYMBOL (if applicable)	7a. NAME OF MONITORING ORGANIZATION Wright Research and Development Center Signature Technology Directorate (WRDC/SNA)		
6c. ADDRESS (City, State, and ZIP Code) 1320 Kinnear Road Columbus, OH 43212		7b. ADDRESS (City, State, and ZIP Code) Wright-Patterson AFB, OH 45433-6523			
8a. NAME OF FUNDING/SPONSORING ORGANIZATION		8b. OFFICE SYMBOL (if applicable)	9. PROCUREMENT INSTRUMENT IDENTIFICATION NUMBER F33615-86-K-1023		
8c. ADDRESS (City, State, and ZIP Code)		10. SOURCE OF FUNDING NUMBERS			
		PROGRAM ELEMENT NO. 61101F	PROJECT NO. ILIR	TASK NO. A6	WORK UNIT ACCESSION NO. 03
11. TITLE (Include Security Classification) UNIFORM THEORY OF DIFFRACTION (UTD) SCATTERING FROM STRUCTURES, INCLUDING HIGHER ORDER TERMS (U); VOLUME VI: Overview of Accomplishments					
12. PERSONAL AUTHOR(S) Brinkley, Timothy J.; Ivriissimtzis, Leonidas P.; and Marhefka, Ronald J.					
13a. TYPE OF REPORT Final		13b. TIME COVERED FROM APR 86 TO DEC 89	14. DATE OF REPORT (Year, Month, Day) November 1990	15. PAGE COUNT 116	
16. SUPPLEMENTARY NOTATION This report volume is Volume VI of six volumes.					
17. COSATI CODES			18. SUBJECT TERMS (Continue on reverse if necessary and identify by block number)		
FIELD	GROUP	SUB-GROUP	Uniform Theory of Diffraction (UTD), Geometric Theory of Diffraction (GTD), Ray Theory, Electromagnetic Scattering, Radar Cross Section, (RCS)		
19. ABSTRACT (Continue on reverse if necessary and identify by block number) This volume summarizes the effort accomplished under Contract F33615-86-K-1023. Theoretical solutions for bistatic first order and higher order Uniform Theory of Diffraction (UTD) terms provide an accurate and efficient means to calculate high frequency scattering from large complex geometries. These techniques have been incorporated into a user-oriented computer code referred to as the Radar Cross Section (RCS) Basic Scattering Code (BSC) (Version 2.0). <i>Version 2.0</i>					
20. DISTRIBUTION/AVAILABILITY OF ABSTRACT <input checked="" type="checkbox"/> UNCLASSIFIED/UNLIMITED <input type="checkbox"/> SAME AS RPT. <input type="checkbox"/> DTIC USERS			21. ABSTRACT SECURITY CLASSIFICATION Unclassified		
22a. NAME OF RESPONSIBLE INDIVIDUAL J. Earl Jones		22b. TELEPHONE (Include Area Code) (513)-255-9335	22c. OFFICE SYMBOL WRDC/SNA		



<b>Accession For</b>	
NTIS GRA&I	<input checked="" type="checkbox"/>
DTIC TAB	<input type="checkbox"/>
Unannounced	<input type="checkbox"/>
Justification	
By _____	
Distribution/	
<b>Availability Codes</b>	
Dist	Avail and/or Special
A-1	

# Contents

<b>List of Figures</b>	<b>v</b>
<b>1 Introduction</b>	<b>1</b>
<b>2 Comparison of Methods for Far Zone Scattering from a Flat Plate and Cube</b>	<b>2</b>
2.1 Introduction . . . . .	2
2.2 Theoretical Background . . . . .	3
2.3 Comparisons . . . . .	9
2.4 Discussion . . . . .	15
2.5 Conclusions . . . . .	20
<b>3 Diffraction of Dipole Excited Edge Waves</b>	<b>21</b>
3.1 Introduction . . . . .	21
3.2 Edge Waves . . . . .	22
3.3 Diffraction formulation . . . . .	24
3.4 The radiation of the edge wave current . . . . .	26
3.5 An equivalent current approach . . . . .	30
3.5.1 Edge wave vertex diffracted field . . . . .	31
3.5.2 Edge wave edge diffracted field . . . . .	34
3.5.3 A heuristic correction factor for the direct edge wave	34
3.6 Discussion and numerical results . . . . .	35
3.7 Summary . . . . .	38
<b>4 Edge Wave Mechanisms for Polyhedral Structures</b>	<b>43</b>
4.1 Introduction . . . . .	43
4.2 Sikta's formulation . . . . .	44

4.3	Edge wave interactions at a polyhedral structure . . . . .	46
4.4	Discussion and numerical results . . . . .	50
<b>5</b>	<b>A Uniform Ray Approximation for the Interaction Between Edges of Three-Dimensional Polyhedral Structures</b>	<b>72</b>
5.1	Introduction . . . . .	72
5.2	A brief review of Michaeli's equivalent currents . . . . .	73
5.3	Higher order terms using non-uniform surface wedge currents	78
5.4	Secondary non-uniform edge equivalent currents . . . . .	86
5.5	Numerical results and discussion . . . . .	91
<b>6</b>	<b>Summary</b>	<b>100</b>
<b>A</b>	<b>Asymptotic Evaluation of an Integral for Edge Waves</b>	<b>102</b>
	<b>Bibliography</b>	<b>104</b>

# List of Figures

2.1	Definition of angles for the Previous Corner Diffraction Coefficients. . . . .	5
2.2	Definition of the Angles used in the New Corner Diffraction Coefficients. . . . .	8
2.3	Two wavelength plate in the x-z plane. . . . .	9
2.4	Backscatter from a 2 wavelength plate ( $\theta = 90^\circ$ pattern). . .	10
2.5	Backscatter from 2 wavelength plate ( $\theta = 90^\circ$ pattern). . . .	11
2.6	Backscatter from 2 wavelength plate ( $\theta = 60^\circ$ pattern). . . .	11
2.7	Backscatter from a 2 wavelength plate ( $\theta = 60^\circ$ pattern). . .	12
2.8	$2\lambda$ square plate in the x-y plane with a fixed source at $\theta^i = 45^\circ$ and $\phi^i = 0$ . . . . .	13
2.9	Co-polarized RCS in the $\phi = 60^\circ$ plane of a $2\lambda$ square plate with a $\hat{\theta}^i$ polarized fixed source at $\theta^i = 45^\circ$ , $\phi^i = 0^\circ$ . . . . .	13
2.10	Co-polarized RCS in the $\phi = 60^\circ$ plane of a $2\lambda$ square plate with a $\hat{\phi}^i$ polarized fixed source at $\theta^i = 45^\circ$ , $\phi^i = 0^\circ$ . . . . .	14
2.11	Cross-polarized RCS in the $\phi = 60^\circ$ plane of a $2\lambda$ square plate with a $\hat{\theta}^i$ polarized fixed source at $\theta^i = 45^\circ$ , $\phi^i = 0^\circ$ . . . . .	14
2.12	Cross-polarized RCS in the $\phi = 60^\circ$ plane of a $2\lambda$ square plate with a $\hat{\phi}^i$ polarized fixed source at $\theta^i = 45^\circ$ , $\phi^i = 0^\circ$ . . . . .	15
2.13	6" Cube tilted $45^\circ$ in the x-z plane. . . . .	16
2.14	H-plane pattern for 6" cube tilted $45^\circ$ in the x-z plane. . . . .	17
2.15	E-plane pattern for 6" cube tilted $45^\circ$ in the x-z plane. . . . .	17
2.16	RCS for the $\theta = 89^\circ$ cut of a $2\lambda$ square plate with a $\hat{\phi}^i$ polarized fixed source at $\theta^i = 45^\circ$ , $\phi^i = 0^\circ$ . . . . .	18
2.17	RCS for the $\theta = 89^\circ$ cut of a $2\lambda$ square plate with a $\hat{\theta}^i$ polarized fixed source at $\theta^i = 45^\circ$ , $\phi^i = 0^\circ$ . . . . .	19
3.1	Dipole excited edge wave. . . . .	23

3.2	Edge wave diffraction at a trihedron. . . . .	25
3.3	Geometry of the edge wave diffraction problem. . . . .	27
3.4	(a) Angular section Geometry. (b) Far region edge and vertex diffracted $\hat{\beta}$ -directed field at the cone $\beta = 85^\circ$ : dotted line - edge wave current solution, solid line - edge wave and fringe current solution. . . . .	39
3.5	Far field $\hat{\beta}$ -directed wave at the azimuthal cut $\phi = 180^\circ$ (normalized to 2.3dB). . . . .	40
3.6	Far field $\hat{\beta}$ -directed wave at the azimuthal cut $\phi = 135^\circ$ (normalized to 1.9dB). . . . .	40
3.7	Far field $\hat{\beta}$ -directed wave at the azimuthal cut $\phi = 45^\circ$ (normalized to -2.0dB). . . . .	41
3.8	Far field $\hat{\phi}$ -directed wave at the azimuthal cut $\phi = 120^\circ$ . . .	41
3.9	Far field $\hat{\beta}$ -directed wave at the azimuthal cut $\phi = 180^\circ$ (normalized to 5dB). . . . .	42
3.10	Far field $\hat{\beta}$ -directed wave at the azimuthal cut $\phi = 150^\circ$ (normalized to 3.0dB). . . . .	42
4.1	Corner excited edge wave. . . . .	44
4.2	Geometry of the corner-to-corner edge wave interaction. . .	45
4.3	Edge wave diffraction for a polyhedral structure. . . . .	47
4.4	$\sigma_{\theta\theta'}$ RCS of Sikta's triangle with $a = 2\lambda$ and $\alpha = 30^\circ$ at $\theta = 90^\circ$ . . . . .	53
4.5	$\sigma_{\theta\theta'}$ RCS of Sikta's triangle with $a = 3\lambda$ and $\alpha = 30^\circ$ at $\theta = 90^\circ$ . . . . .	53
4.6	$\sigma_{\theta\theta'}$ RCS of a $2\lambda$ square plate at $\theta = 30^\circ$ . . . . .	54
4.7	$\sigma_{\phi\theta'}$ RCS of a $2\lambda$ square plate at $\theta = 30^\circ$ . . . . .	54
4.8	$\sigma_{\theta\theta'}$ RCS of a $2\lambda$ square plate at $\theta = 45^\circ$ . . . . .	55
4.9	$\sigma_{\theta\theta'}$ RCS of a $2\lambda$ square plate at $\theta = 60^\circ$ . . . . .	55
4.10	Impulse response of a diamond shape plate at nose-on: (a) measured, (b) calculated. . . . .	56
4.11	Impulse response of a 24" square plate at $\phi = 45^\circ$ and $\theta = 15^\circ$ . Vertical polarization. (a) Measured, (b) Calculated. . .	57
4.12	Impulse response of a 24" square plate at $\phi = 45^\circ$ and $\theta = 30^\circ$ . Vertical polarization. (a) Measured, (b) Calculated. . .	58
4.13	Impulse response of a 24" square plate at $\phi = 45^\circ$ and $\theta = 45^\circ$ . Vertical polarization. (a) Measured, (b) Calculated. . .	59

4.14	Impulse response of a 24" square plate at $\phi = 45^\circ$ and $\theta = 60^\circ$ . Vertical polarization. (a) Measured, (b) Calculated. . .	60
4.15	Impulse response of a 24" square plate at $\phi = 45^\circ$ and $\theta = 75^\circ$ . Vertical polarization. (a) Measured, (b) Calculated. . .	61
4.16	Impulse response of a 24" square plate at $\phi = 45^\circ$ and $\theta = 15^\circ$ . Horizontal polarization. (a) Measured, (b) Calculated.	62
4.17	Impulse response of a 24" square plate at $\phi = 45^\circ$ and $\theta = 30^\circ$ . Horizontal polarization. (a) Measured, (b) Calculated.	63
4.18	Impulse response of a 24" square plate at $\phi = 45^\circ$ and $\theta = 45^\circ$ . Horizontal polarization. (a) Measured, (b) Calculated.	64
4.19	Impulse response of a 24" square plate at $\phi = 45^\circ$ and $\theta = 60^\circ$ . Horizontal polarization. (a) Measured, (b) Calculated.	65
4.20	Impulse response of a 24" square plate at $\phi = 45^\circ$ and $\theta = 75^\circ$ . Horizontal polarization. (a) Measured, (b) Calculated.	66
4.21	Impulse response of a 24" square plate at $\phi = 45^\circ$ and $\theta = 15^\circ$ . Cross polarization. (a) Measured, (b) Calculated. . . .	67
4.22	Impulse response of a 24" square plate at $\phi = 45^\circ$ and $\theta = 30^\circ$ . Cross polarization. (a) Measured, (b) Calculated. . . .	68
4.23	Impulse response of a 24" square plate at $\phi = 45^\circ$ and $\theta = 45^\circ$ . Cross polarization. (a) Measured, (b) Calculated. . . .	69
4.24	Impulse response of a 24" square plate at $\phi = 45^\circ$ and $\theta = 60^\circ$ . Cross polarization. (a) Measured, (b) Calculated. . . .	70
4.25	Impulse response of a 24" square plate at $\phi = 45^\circ$ and $\theta = 75^\circ$ . Cross polarization. (a) Measured, (b) Calculated. . . .	71
5.1	Infinite wedge illuminated by a plane wave. . . . .	73
5.2	Non-uniform component of the current at the wedge. . . . .	74
5.3	Steepest descent paths in the complex $\xi$ plane (from [Pathak and Kouyoumjian, 1971]). . . . .	75
5.4	The complex $\gamma$ plane. . . . .	77
5.5	Non-uniform current excited by an edge and associated ray contributions at a polygonal structure illuminated by a plane wave. . . . .	79
5.6	Geometry for the surface current integration. . . . .	81
5.7	The secondary non-uniform current. . . . .	86
5.8	Non-parallel edges geometry. . . . .	88
5.9	Principal plane RCS $\sigma_{\theta\theta'}$ of a $5\lambda$ square plate. . . . .	94

5.10	Principal plane RCS $\sigma_{\phi\phi'}$ of a $5\lambda$ square plate. . . . .	94
5.11	Bistatic cross section $\sigma_{\theta\theta'}$ of a $5\lambda$ square plate for $\theta' = 45^\circ$ and $\phi' = 0^\circ$ at $\phi = 60^\circ$ . . . . .	95
5.12	Bistatic cross section $\sigma_{\phi\phi'}$ of a $5\lambda$ square plate for $\theta' = 45^\circ$ and $\phi' = 0^\circ$ at $\phi = 60^\circ$ . . . . .	95
5.13	Bistatic cross section $\sigma_{\phi\phi'}$ of a $5\lambda$ square plate for $\theta' = 45^\circ$ and $\phi' = 0^\circ$ at $\phi = 60^\circ$ . . . . .	96
5.14	Bistatic cross section $\sigma_{\theta\phi'}$ of a $5\lambda$ square plate for $\theta' = 45^\circ$ and $\phi' = 0^\circ$ at $\phi = 60^\circ$ . . . . .	96
5.15	Bistatic cross section $\sigma_{\theta\theta'}$ of a $2\lambda$ square plate for $\theta' = 60^\circ$ and $\phi' = 45^\circ$ at $\phi = 60^\circ$ . . . . .	97
5.16	Bistatic cross section $\sigma_{\phi\phi'}$ of a $2\lambda$ square plate for $\theta' = 60^\circ$ and $\phi' = 45^\circ$ at $\phi = 60^\circ$ . . . . .	97
5.17	Bistatic cross section $\sigma_{\phi\phi'}$ of a $2\lambda$ square plate for $\theta' = 60^\circ$ and $\phi' = 45^\circ$ at $\phi = 60^\circ$ . . . . .	98
5.18	Bistatic cross section $\sigma_{\theta\phi'}$ of a $2\lambda$ square plate for $\theta' = 60^\circ$ and $\phi' = 45^\circ$ at $\phi = 60^\circ$ . . . . .	98
5.19	RCS $\sigma_{\theta\theta'}$ of Sikta's triangle with $a = 3\lambda$ and $\alpha = 30^\circ$ at $\theta = 90^\circ$ . . . . .	99
5.20	RCS $\sigma_{\phi\phi'}$ of Sikta's triangle with $a = 3\lambda$ and $\alpha = 30^\circ$ at $\theta = 90^\circ$ . . . . .	99

# Chapter 1

## Introduction

This volume gives a summary the major technical achievements on Contract No. F33615-86-K-1023 for the period April 1986 to December 1989. The overall goals of this contract are to study and determine solutions for bistatic first order and higher order Uniform Geometrical Theory of Diffraction terms, that provide an accurate and efficient means to calculate high frequency scattering from large complex geometries. Algorithms have been developed to incorporate these techniques into a user oriented computer code referred to as the RCS - Basic Scattering Code (RCS-BSC) [1].

This volume presents discussions of theoretical studies that have been completed during this time frame. Chapter 2 discusses various methods for determining the first order scattering from flat plate structures. It presents a newly developed far zone corner (vertex) diffraction coefficient. Complete details are given in References [2,3]. Chapter 3 presents a discussion of a form of edge wave - vertex interaction. It is specifically formulated in this case for a source excitation. This is an intermediate step for determining the far zone edge wave solution. More details are given in References [4,5]. The extension of this work to the far zone edge wave solution is presented in Chapter 4. Other higher order double diffraction interactions across the flat plate faces are discussed in Chapter 5.

## Chapter 2

# Comparison of Methods for Far Zone Scattering from a Flat Plate and Cube

### 2.1 Introduction

The validity of various methods for determining the far zone bistatic scattering from a flat plate and convex flat plate structure such as a cube is presented in this chapter. This is accomplished by comparing the methods in various basic situations. The specific techniques to be compared in this study are the classical equivalent currents with "stripping" [6], the previous corner diffraction coefficient [6], the newly developed equivalent currents by Michaeli [7], and an extension to this method cast in the form of a Uniform Geometrical Theory of Diffraction (UTD) far zone corner diffraction coefficient [2]. In addition, the Method of Moments (MOM) using the Electromagnetic Surface Patch (ESP) code [8] and measurements from The Ohio State University ElectroScience Laboratories compact range are used to further validate the results.

A recent paper by Ludwig [9] compares three methods for backscattering from a cube, that is, the MOM using the Numerical Electromagnetics Code (NEC-MOM), physical optics (PO), and the previous UTD corner diffraction solution. In this chapter, it will be shown that methods which give comparable results for backscatter can differ for bistatic scattering. The emphasis here is to present basic examples that can be used to validate

existing codes and to suggest a numerically efficient and accurate method for convex flat plate structures to first order.

An approximate expression for the far zone field scattered by the vertex of a finite perfectly conducting wedge is presented in this regard. The solution is cast in the form of the UTD and is based on asymptotic equivalent currents found using modified PTD concepts [7,2]. The faces of the wedge must be flat (the normal to each individual face is a constant everywhere on the face except at the edge) and the edges must be straight. For plane wave incidence from an arbitrary direction, the first order contribution from each vertex to the far zone scattered field is obtained.

Since diffraction is a local phenomena at high frequencies the results obtained for a finite wedge may be applied to much more complex bodies made up of simple shapes. The field scattered by a three-dimensional shape constructed from flat plates may be approximated to first order as the sum of the contributions from each individual corner. The first order solution should be reasonably accurate in or near the specular regions as long as the object is convex. A convex body is defined here as a closed surface made up of flat plates such that all of the exterior wedge angles, taken between faces and exterior to the surface, are greater than 180 degrees. A simple example of an object that does not meet this requirement is a corner reflector. In this case, the effect of the interaction between the faces must be taken into account. Higher order effects such as double diffraction [10] and edge waves [11] are not considered in this chapter.

Note that the results presented in this chapter are for a parallel ray type solution, that is, for a radar cross section result. The NEC - Basic Scattering Code (NEC-BSC)[12] is a near zone formulated code, that is it has a finite range involved. The UTD solutions are slightly different for this non-parallel ray case. The capabilities of the NEC-BSC and a comparable far zone code called the RCS-BSC are discussed in Reference [13].

## 2.2 Theoretical Background

There are many approximate solutions to the scattered field from a finite perfectly conducting wedge. Physical Optics and its extension the Physical Theory of Diffraction [14] is surface and edge current based. Geometrical Optics (GO) and its extensions the Geometrical Theory of Diffraction

(GTD) [15] and the Uniform Geometrical Theory of Diffraction [16] are ray based. The Method of Equivalent Currents (MEC) [17] is an intermediate type solution that was developed to handle caustic regions in the GTD. This has been augmented with the concept of stripping to provide better answers for flat plate problems [6]. Recently, Michaeli [18] showed a more rigorous approach in deriving equivalent currents. This was shown to be related to the incremental length method of Mitzner [19] by Knott [20]. These equivalent currents still had singularity problems that have been remedied by Michaeli [7] using a skewed coordinate system. Ufimtsev also derived a similar solution [21,22].

The above solutions can be cast in a corner diffraction coefficient form. These UTD ray type solutions have the advantage of being efficient for far zone flat plate problems since only the fields scattered from the corners need to be added. It also has the advantage that the results correlate to the scattering centers seen in high resolution measurements. Just the corner diffraction coefficient forms are outlined in this section.

A previous diffraction coefficient for a corner formed by the intersection of two straight edges was derived by Burnside and Pathak [6]. It is based on the asymptotic evaluation of the radiation integral containing the equivalent currents of Ryan and Peters [17]. The result was then empirically modified so that the diffraction coefficient would not change sign abruptly as it passes through the false shadow boundaries. It was derived for spherical wave incidence and remains valid for cases when the diffraction point is near the corner since the integral was evaluated for a saddle point near an end point; however, only the far zone result is shown here. The corner diffracted field due to one corner and one edge in the case of plane wave incidence and a far zone receiver is given by

$$\begin{bmatrix} E_{\beta_o}^c \\ E_{\phi}^c \end{bmatrix} = - \begin{bmatrix} E_{\beta_o}^i(Q_c) D_s^c(\phi, \phi', \beta_o, \beta_{oc}) \\ E_{\phi}^i(Q_c) D_h^c(\phi, \phi', \beta_o, \beta_{oc}) \end{bmatrix} \frac{e^{-jks}}{s} \quad (2.1)$$

$$\begin{bmatrix} D_s^c \\ D_h^c \end{bmatrix} = \mp \begin{bmatrix} C_s(Q_c) \\ C_h(Q_c) \end{bmatrix} \frac{\sqrt{\sin \beta_o \sin \beta_{oc}}}{(\cos \beta_{oc} + \cos \beta_o)} \frac{e^{-j\frac{\pi}{4}}}{\sqrt{2\pi k}} \quad (2.2)$$

$$C_{s,h}(Q_c) = \frac{-e^{-j\frac{\pi}{4}}}{2n\sqrt{2\pi k} \sin \beta_o} \{ [D_o^c(\phi - \phi') + D_n^c(\phi - \phi')] \mp [D_o^c(\phi + \phi') + D_n^c(\phi + \phi')] \} \quad (2.3)$$

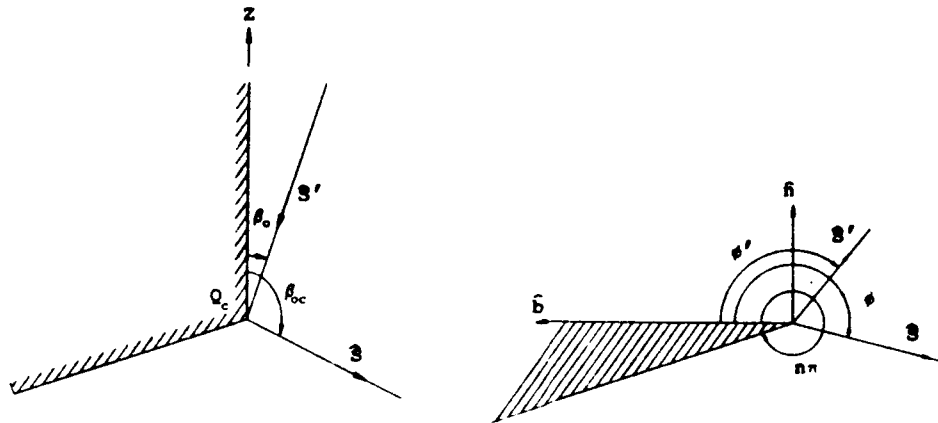


Figure 2.1: Definition of angles for the Previous Corner Diffraction Coefficients.

$$D_{o,n}^c(\psi) = D_{o,n}(\psi) \left| F \left[ \frac{\sin^2 \beta_a a^\mp(\psi)}{2\pi a (\beta_{oc} + \beta_o)} \right] \right| \quad (2.4)$$

$$a(\beta) = 2 \cos^2 \left( \frac{\beta}{2} \right), \quad a^\mp(\psi) = 2 \cos^2 \left( \frac{2n\pi N^\mp - \psi}{2} \right) \quad (2.5)$$

where  $N^\mp$  is the integer which most nearly satisfies  $2n\pi N^\mp - \psi = \mp\pi$ , and

$$D_{o,n}(\psi) = \cot \left[ \frac{\pi \mp \psi}{2n} \right] \quad (2.6)$$

$$\beta_a = \frac{\pi + \beta_o - \beta_{oc}}{2} \quad (2.7)$$

$$F(x) = 2j |\sqrt{x}| e^{jx} \int_{|\sqrt{x}|}^{\infty} e^{-j\tau^2} d\tau \quad (2.8)$$

where the angles are shown in Figure 2.1. The sign on the diffraction coefficient may be plus or minus depending on which endpoint of the edge is being considered. The correct sign in front of the  $C_{s,h}$  terms in Equation (2.2) is chosen based on the direction of the edge vector shown in Figure 2.1.

It is assumed that the incident field, and therefore the scattered field, is a time harmonic field with time dependence given by  $e^{j\omega t}$ , which is suppressed.

The new far zone corner diffraction solution is based on the PTD and cast into the form of the MEC and then into a UTD diffraction coefficient. This is done as follows. The PO is first used to approximate the currents resulting in a double integral over the surface. Stokes theorem is then applied to reduce the equation to a line integral [23,24]. The Michaeli currents are added to produce a total first order MEC result. This integral is then evaluated using the method of stationary phase to obtain the contribution from each corner [25].

The new corner diffraction coefficients are given in a form similar to previous expressions for diffraction coefficients:

$$\begin{bmatrix} E_{\beta}^c \\ E_{\phi}^c \end{bmatrix} = \begin{bmatrix} D_s^c & D_h^c \\ 0 & D_h^c \end{bmatrix} \begin{bmatrix} E_{\beta'}^i \\ E_{\phi'}^i \end{bmatrix} \frac{e^{-jk_s}}{s} \quad (2.9)$$

$$D_{s,h,2}^c = \pm \frac{j}{4\pi k} \left( \frac{1}{\cos \beta - \cos \beta'} \right) [d_{s,h,2}^{LPO} + d_{s,h,2}^{UTD} - d_{s,h,2}^{PO}] \quad (2.10)$$

where the plus or minus sign is chosen depending on which endpoint contribution is being calculated. The minus sign is used for the corner contribution associated with the negative t-axis, while the plus sign is used for the corner contribution associated with the positive t-axis. The edge fixed coordinates shown in Figure 2.2 are chosen such that  $\hat{n}$  is the outward normal of the O-face,  $\hat{t}$  is tangent to the edge, the positive b-axis lies on the O-face, and  $\hat{t} = \hat{b} \times \hat{n}$ . The expressions for  $d_{s,h,2}^{LPO}$ ,  $d_{s,h,2}^{UTD}$ , and  $d_{s,h,2}^{PO}$  are given by (O-face contribution only)

$$\begin{aligned} d_{s,h,2}^{LPO} &= \frac{1}{2} U^i c_{s,h,2}(\gamma, \phi') \left\{ \left[ \cot \left( \frac{\pi - (\gamma - \phi')}{4} \right) - \cot \left( \frac{\pi + (\gamma - \phi')}{4} \right) \right] \right. \\ &\quad \mp \left. \left[ \cot \left( \frac{\pi - (\gamma + \phi')}{4} \right) - \cot \left( \frac{\pi + (\gamma + \phi')}{4} \right) \right] \right\} \quad (2.11) \end{aligned}$$

$$\begin{aligned} d_{s,h,2}^{UTD} &= \frac{1}{n} c_{s,h,2}(\alpha, \pi - \alpha) \left[ \cot \left( \frac{\pi - (\alpha - \phi')}{2n} \right) \right. \\ &\quad \mp \left. \cot \left( \frac{\pi - (\alpha + \phi')}{2n} \right) \right] \quad (2.12) \end{aligned}$$

$$d_{s,h,2}^{PO} = \frac{1}{2} U^i c_{s,h,2}(\alpha, \phi') \left\{ \left[ \cot \left( \frac{\pi - (\alpha - \phi')}{4} \right) - \cot \left( \frac{\pi + (\alpha - \phi')}{4} \right) \right] \right\}$$

$$\mp \left[ \cot \left( \frac{\pi - (\alpha + \phi')}{4} \right) - \cot \left( \frac{\pi + (\alpha + \phi')}{4} \right) \right] \quad (2.13)$$

$$c_s(\delta, \epsilon) = -\frac{\sin \beta}{\sin \beta'} \quad (2.14)$$

$$c_h(\delta, \epsilon) = \frac{\sin \phi}{\sin \delta} \quad (2.15)$$

$$c_2(\delta, \epsilon) = -\frac{\sin \beta}{\sin \delta} (\cot \beta \cos \phi + \cot \beta' \cos \epsilon) \quad (2.16)$$

$$\cos \gamma = \frac{\sin \beta \cos \phi}{\sin \beta'} + \frac{(\cos \beta - \cos \beta')^2}{\sin \beta' (\sin \beta \cos \phi + \sin \beta' \cos \phi')} \quad (2.17)$$

$$\cos \alpha = \frac{\sin \beta \cos \phi}{\sin \beta'} + \frac{(\cos \beta - \cos \beta') \cos \beta'}{\sin^2 \beta'} \quad (2.18)$$

$$\cos^{-1} \mu = -j \ln \left( \mu + \sqrt{\mu^2 - 1} \right) \quad (2.19)$$

$$\sqrt{\mu^2 - 1} = \begin{cases} -|\sqrt{\mu^2 - 1}| & \mu < -1 \\ j|\sqrt{1 - \mu^2}| & -1 \leq \mu \leq 1 \\ |\sqrt{\mu^2 - 1}| & \mu > 1 \end{cases} \quad (2.20)$$

$$U^i = \begin{cases} 0 & , \pi - \phi' < 0 \\ 1 & , \pi - \phi' > 0 \end{cases} \quad (2.21)$$

where the + sign is associated with  $d_h^{LPO}$ ,  $d_2^{LPO}$ ,  $d_h^{UTD}$ ,  $d_2^{UTD}$ ,  $d_h^{PO}$ , and  $d_2^{PO}$  while the - sign is associated with the  $d_s^{LPO}$ ,  $d_s^{UTD}$ , and  $d_s^{PO}$  terms. The angles are defined in Figure 2.2. Since only convex structures are considered here proper shadowing of the rays is fairly simple. The shadowing of the incident field is accounted for by  $\vec{E}_\beta^i$  and  $\vec{E}_\phi^i$ , which are the components of the GO incident field. The shadowing of the diffracted ray is more complicated. The contributions from the LPO and PO components,  $d_{h,s,2}^{LPO}$  and  $d_{h,s,2}^{PO}$ , are present everywhere. The UTD components,  $d_{h,s,2}^{UTD}$ , are shadowed like diffracted fields. They do not contribute if the observation point is inside the wedge ( $\phi > n\pi$ ).

For the special case of a flat plate ( $n = 2$ ) the contribution from both faces may be found using

$$d_{h,2}^{LPO} = \frac{1}{2} S^i c_{h,2}(\gamma, \phi') \left\{ \left[ \cot \left( \frac{\pi - (\gamma - \phi')}{4} \right) - \cot \left( \frac{\pi + (\gamma - \phi')}{4} \right) \right] \right\}$$

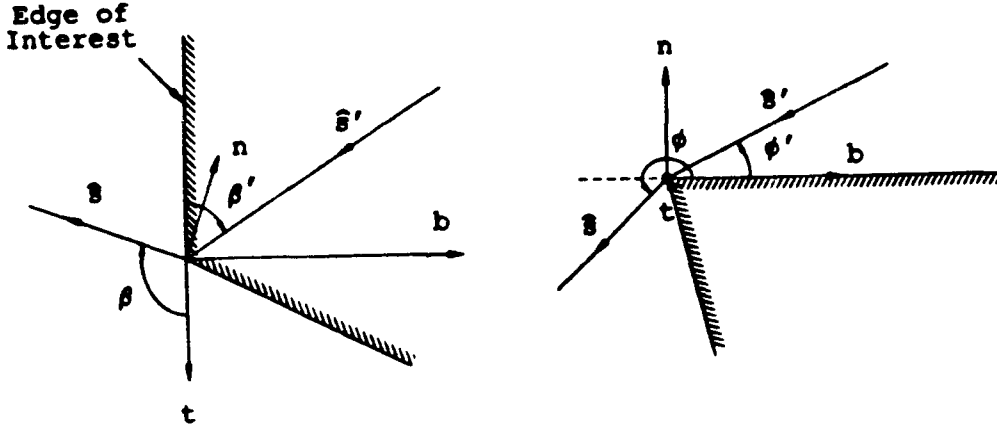


Figure 2.2: Definition of the Angles used in the New Corner Diffraction Coefficients.

$$\mp \left[ \cot \left( \frac{\pi - (\gamma + \phi')}{4} \right) - \cot \left( \frac{\pi + (\gamma + \phi')}{4} \right) \right] \quad (2.22)$$

$$d_{h,2}^{UTD} = \frac{1}{n} c_{h,2}(\alpha, \pi - \alpha) \left\{ \left[ \cot \left( \frac{\pi - (\alpha - \phi')}{4} \right) + \cot \left( \frac{\pi + (\alpha - \phi')}{4} \right) \right] \right. \\ \left. \mp \left[ \cot \left( \frac{\pi - (\alpha + \phi')}{4} \right) + \cot \left( \frac{\pi + (\alpha + \phi')}{4} \right) \right] \right\} \quad (2.23)$$

$$d_{h,2}^{PO} = \frac{1}{2} S^i c_{h,2}(\alpha, \phi') \left\{ \left[ \cot \left( \frac{\pi - (\alpha - \phi')}{4} \right) - \cot \left( \frac{\pi + (\alpha - \phi')}{4} \right) \right] \right. \\ \left. \mp \left[ \cot \left( \frac{\pi - (\alpha + \phi')}{4} \right) - \cot \left( \frac{\pi + (\alpha + \phi')}{4} \right) \right] \right\} \quad (2.24)$$

$$S^i = \begin{cases} -1 & , \pi - \phi' < 0 \\ 1 & , \pi - \phi' > 0 \end{cases} \quad (2.25)$$

where  $\gamma$ ,  $\alpha$ , and the other variables have been defined previously.

It is interesting to note that by writing the equations for the Michaeli equivalent currents and the new corner diffraction coefficients in cotangent form provides more insight into the connection of the new solutions with the previous methods. The new parameters separate out the optics currents and diffraction currents. This separation manifests itself in new parameters for the  $\phi$  angles. They arise from the asymptotic evaluation of the currents

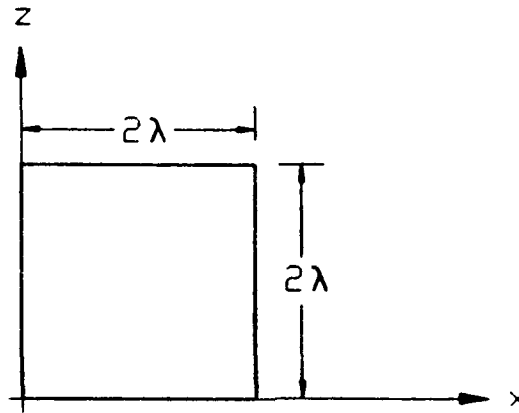


Figure 2.3: Two wavelength plate in the x-z plane.

in the skewed coordinate system chosen in physically meaningful directions. The LPO factor ( $\gamma$ ) is related to the projection of the average of the incident and diffraction planes on to the plane of the plate [2]. The PO and UTD factor ( $\alpha$ ) relates to the projection of the Keller diffraction cone on to the plane of the plate. It is easy to see in this form that in the Keller directions the LPO and PO cancel, leaving the UTD result formally used in many solutions.

### 2.3 Comparisons

The first example compares the Ryan and Peters equivalent currents, the previous and new corner diffraction solutions. The simple example of backscatter from a two wavelength square plate lying in the x-z plane, as shown in Figure 2.3, is used. This illustrates that for backscatter these different methods produce very similar results, except for the very low level regions.

The co-polarized fields, in the principal plane, calculated using the three different methods are shown in Figures 2.4 and 2.5. All three methods give essentially the same results for the principal plane pattern cuts shown

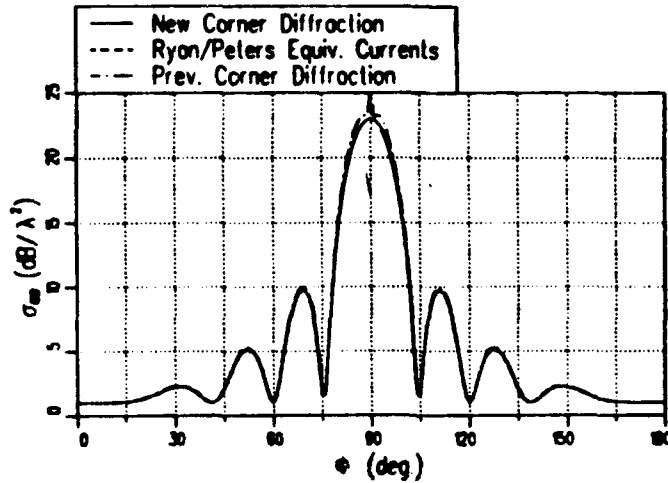


Figure 2.4: Backscatter from a 2 wavelength plate ( $\theta = 90^\circ$  pattern).

here. This is not surprising since the major contributions to the fields are the scattering from the two edges in their Keller cone directions. The new corner diffraction solution reduces to the Ryan and Peters equivalent current solution for points on the Keller cone [2], and the previous corner diffraction solution is essentially the same as Ryan and Peters equivalent current solution for most regions of space. The results in Figure 2.5 are for the horizontal ( $\sigma_{\phi\phi}$ ) polarization. For a knife edged plate such as this, the scattered field should be zero in the plane of the plate. Note that this is not the case in these first order results. The higher order terms (i.e. the double, triple etc. diffractions) produce the null for this polarization when they are included.

For patterns away from the principal plane, the higher levels are the same but the lower levels differ. This is illustrated by taking a conical cut ( $\theta = 60^\circ$ ) for the two wavelength plate. The results for the same three methods used previously are shown in Figures 2.6 and 2.7. In this case the methods agree well for the main lobe, however, they differ in the lower levels of the pattern.

The differences in the three methods mentioned earlier are greatly increased for bistatic scattering problems. The bistatic scattering from a square plate two wavelengths on a side is examined to illustrate this point.

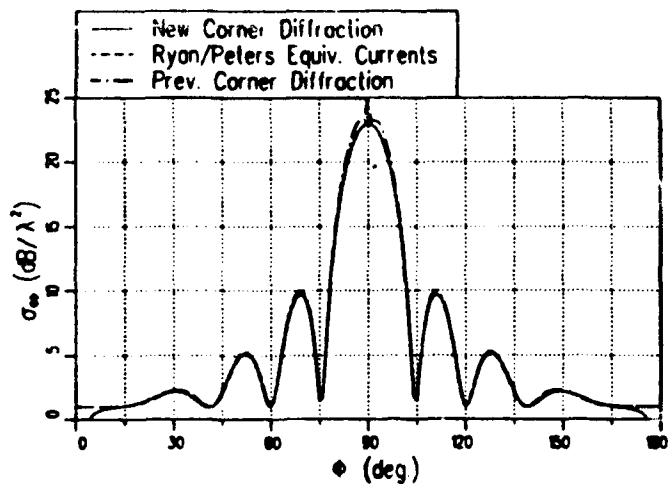


Figure 2.5: Backscatter from 2 wavelength plate ( $\theta = 90^\circ$  pattern).

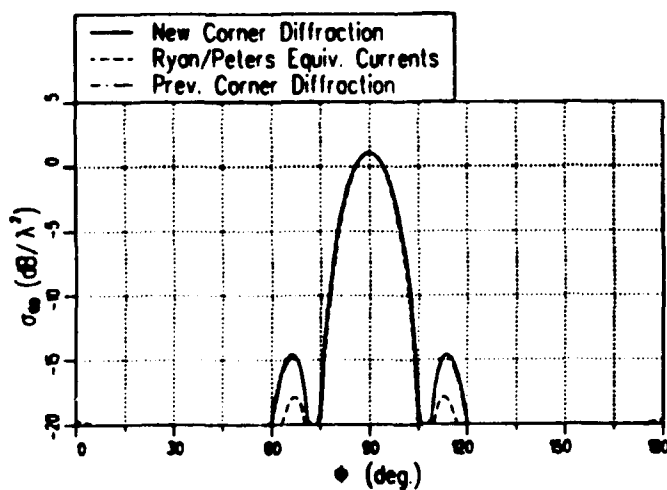


Figure 2.6: Backscatter from 2 wavelength plate ( $\theta = 60^\circ$  pattern).

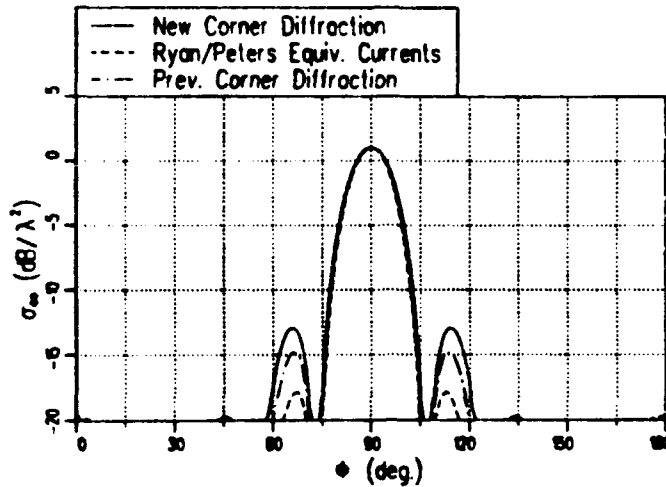


Figure 2.7: Backscatter from a 2 wavelength plate ( $\theta = 60^\circ$  pattern).

The complete scattering matrix (all four values of  $\sigma$ ) is found for a plate in the x-y plane with a fixed source located at  $\theta^i = 45^\circ$  and  $\phi^i = 0^\circ$  as shown in Figure 2.8. The results for the  $\phi = 60^\circ$  pattern cut are compared with the previous corner diffraction solution and Method of Moment calculations for co-polarized fields in Figures 2.9 and 2.10. Similarly the results for the cross-polarized fields are given in Figure 2.11 and Figure 2.12. Overall the new solution agrees well with the Method of Moment calculations and does not exhibit the discontinuities which appear near  $\theta = 240^\circ$  and  $\theta = 300^\circ$  in the previous corner diffraction solution. The discontinuities in the previous corner diffraction solution are caused by the so called false shadow boundaries where the associated two-dimensional problem passes through a shadow boundary, but the three-dimensional problem in reality does not. The Ryan and Peters equivalent current results are not shown here, but they behave differently for similar reasons; that is, the solution still contains two dimension information in regions that it should not. In the region from  $\theta \approx 60^\circ$  to  $120^\circ$  (i.e. near the plane of the plate) the new solution and the Method of Moments solution differ by more than 10 dB. It is suspected that most of these differences are due to the effects of higher order terms (double and triple diffraction, edge waves) which are not included in the new solution.

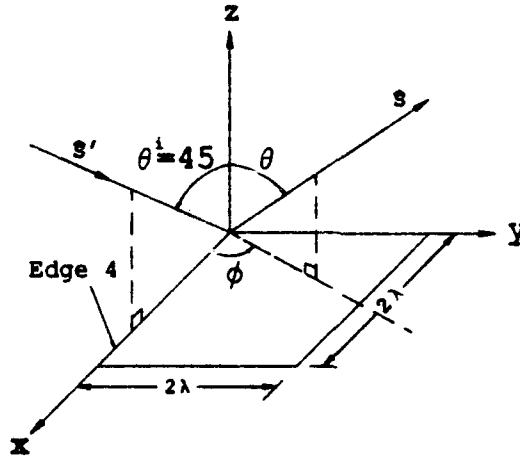


Figure 2.8:  $2\lambda$  square plate in the  $x$ - $y$  plane with a fixed source at  $\theta^i = 45^\circ$  and  $\phi^i = 0$ .

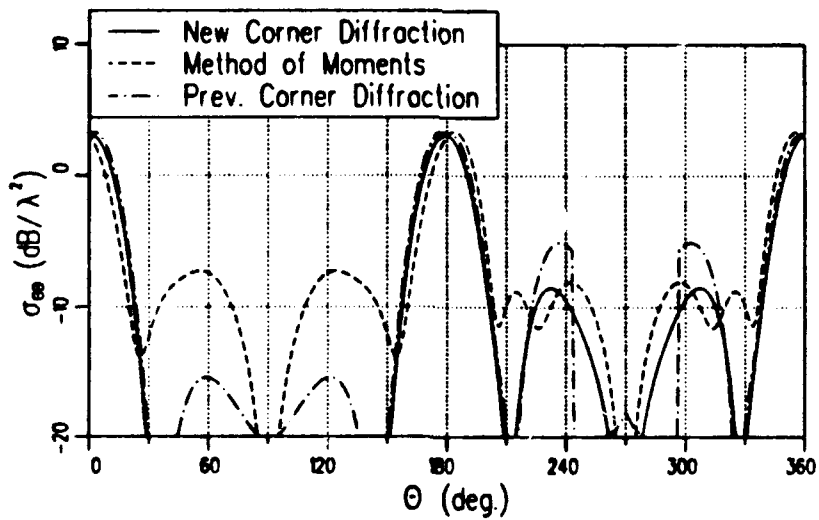


Figure 2.9: Co-polarized RCS in the  $\phi = 60^\circ$  plane of a  $2\lambda$  square plate with a  $\hat{\theta}^i$  polarized fixed source at  $\theta^i = 45^\circ$ ,  $\phi^i = 0^\circ$ .

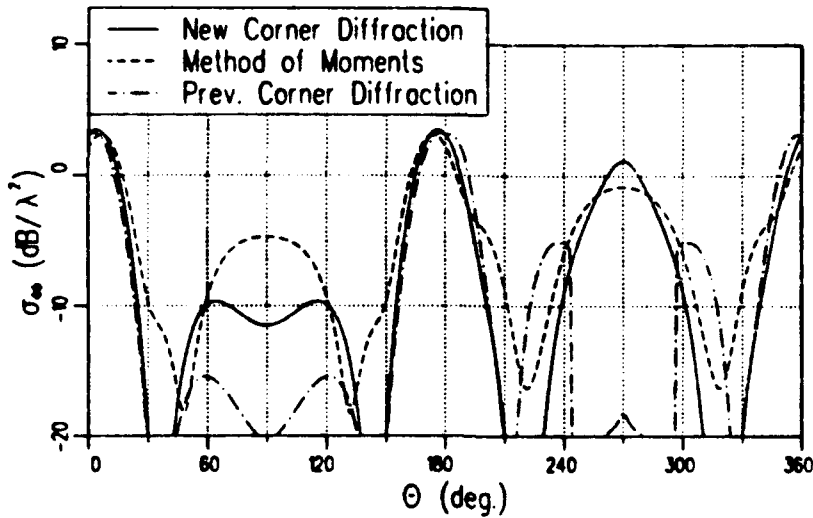


Figure 2.10: Co-polarized RCS in the  $\phi = 60^\circ$  plane of a  $2\lambda$  square plate with a  $\hat{\phi}^i$  polarized fixed source at  $\theta^i = 45^\circ$ ,  $\phi^i = 0^\circ$ .

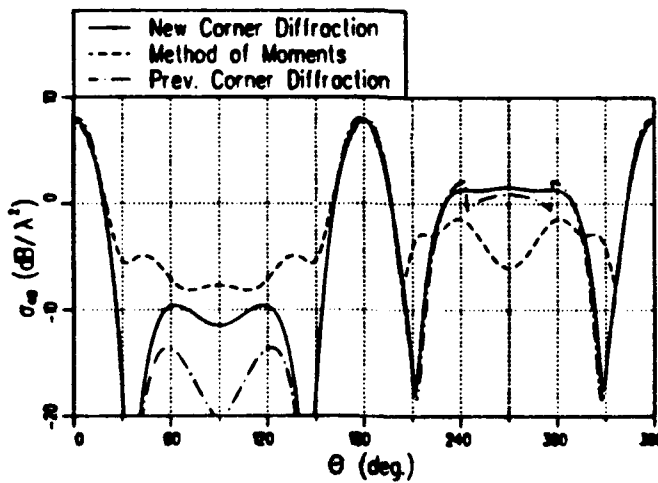


Figure 2.11: Cross-polarized RCS in the  $\phi = 60^\circ$  plane of a  $2\lambda$  square plate with a  $\hat{\theta}^i$  polarized fixed source at  $\theta^i = 45^\circ$ ,  $\phi^i = 0^\circ$ .

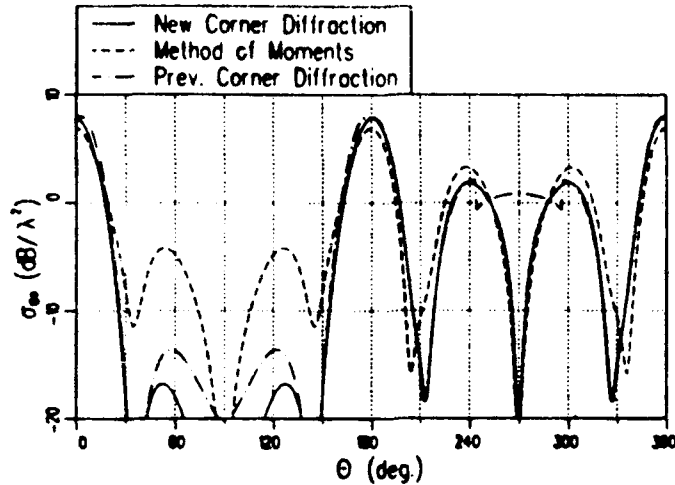


Figure 2.12: Cross-polarized RCS in the  $\phi = 60^\circ$  plane of a  $2\lambda$  square plate with a  $\hat{\phi}^i$  polarized fixed source at  $\theta^i = 45^\circ$ ,  $\phi^i = 0^\circ$ .

In this example the new solution is compared to backscatter measurements [26] made at 10 GHz on a 6" cube. The geometry of the cube, tilted  $45^\circ$  in the  $x$ - $z$  plane, is illustrated in Figure 2.13. The results for the H-plane and E-plane patterns taken in the  $x$ - $y$  plane are given in Figures 2.14 and 2.15, respectively. The results agree well to first order over most regions of the pattern. The discrepancies are probably due to a combination of higher order terms not being included in the analysis and in measurements errors. The error in the measurements is likely two fold. First the faces of the cube model were misaligned slightly so they did not form edges as sharp as may be required. Secondly, it seems that there was some deviation from the desired pattern cuts as can be seen from the lack of symmetry in the measured patterns. In any case, they confirm the validity of the new corner diffraction solution within first order accuracy for wedge type structures.

## 2.4 Discussion

The new corner diffraction coefficient in the above examples has been shown to provide improved results over other methods, especially in bistatic sit-

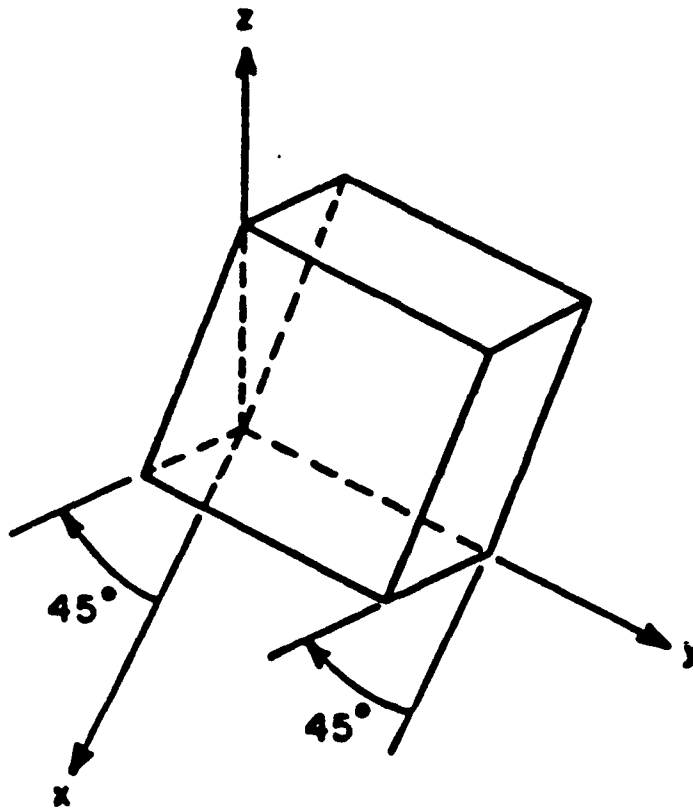


Figure 2.13: 6" Cube tilted 45° in the x-z plane.

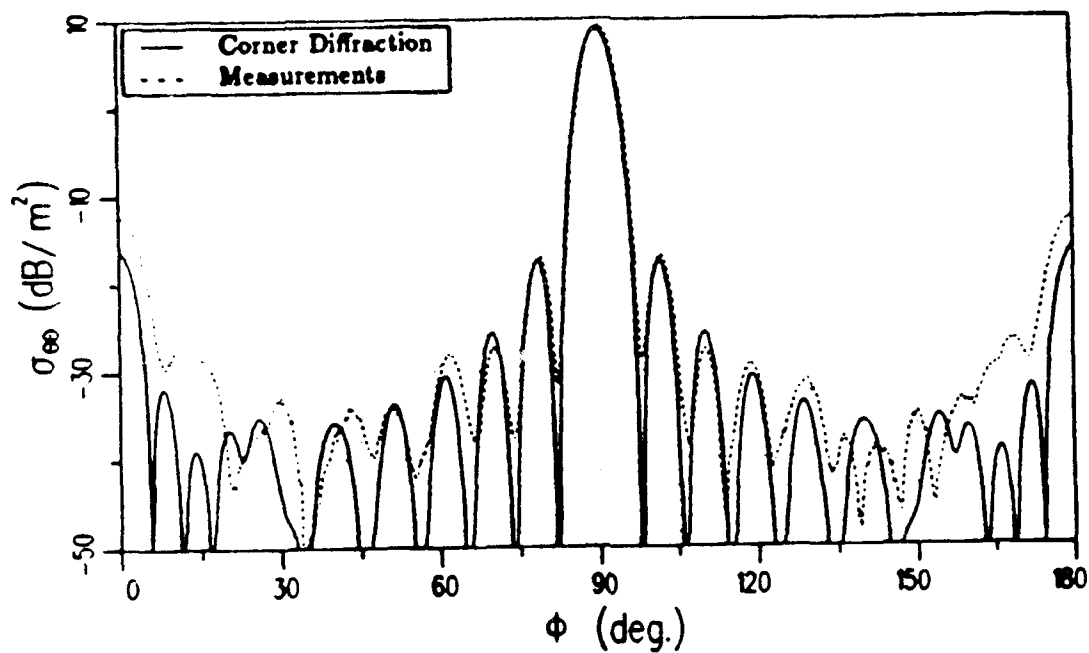


Figure 2.14: H-plane pattern for 6" cube tilted 45° in the x-z plane.

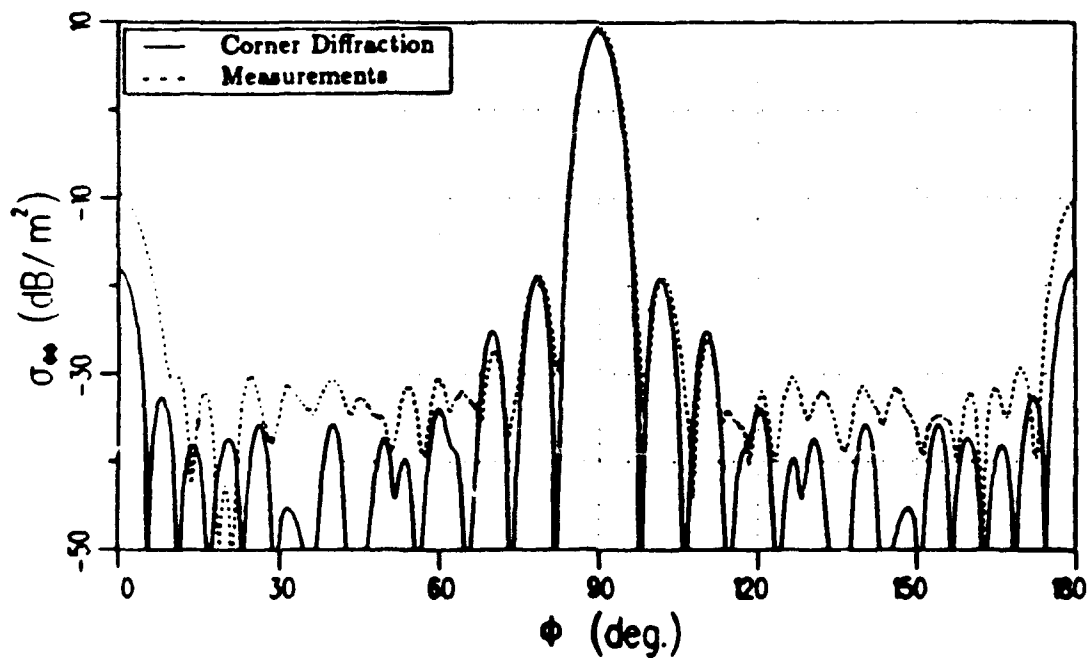


Figure 2.15: E-plane pattern for 6" cube tilted 45° in the x-z plane.

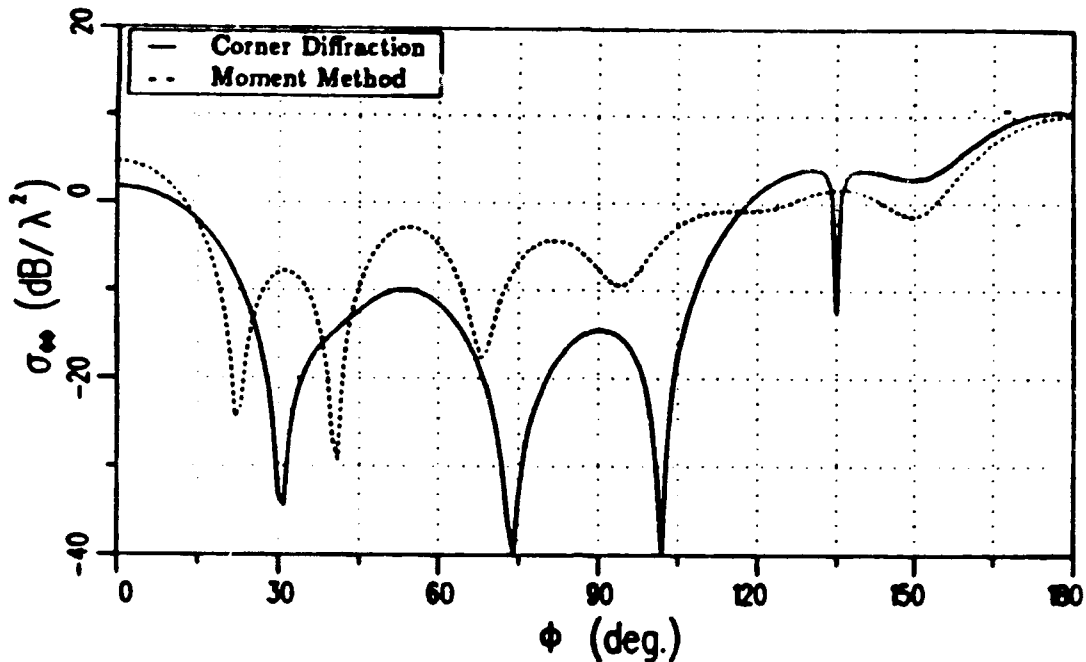


Figure 2.16: RCS for the  $\theta = 89^\circ$  cut of a  $2\lambda$  square plate with a  $\hat{\phi}^i$  polarized fixed source at  $\theta^i = 45^\circ$ ,  $\phi^i = 0^\circ$ .

uations. The Michaeli equivalent currents have not been shown since they provide the same results as the new corner diffraction coefficient. Certain properties of these new solutions, however, may still cause patterns taken in some regions of space to be discontinuous.

It has been shown [7,2] that  $D_2^c$  and  $D_h^c$  do not tend to definite limits as  $\hat{s} \rightarrow \hat{\sigma}$  (i.e. the intersection of the associated half-plane and the Keller cone), where  $\hat{\sigma} = \hat{i} \sin \beta' + \hat{b} \cos \beta'$ , but they remain bounded. In practice, this means that both  $D_2^c$  and  $D_h^c$ , and therefore  $E_\beta^c$  and  $E_\phi^c$ , are discontinuous at this point in the pattern. A simple example illustrates how this discontinuity can affect a pattern. The bistatic RCS from the flat plate shown earlier in Figure 2.8 is considered. The source, linearly polarized in the  $\hat{\phi}^i$  direction, remains fixed at  $\theta^i = 45^\circ$  and  $\phi^i = 0^\circ$  while the pattern is taken near the x-y plane ( $\theta = 89^\circ$ ). The bistatic RCS is given in Figures 2.16 and 2.17 for the co-polarized and cross-polarized fields, respectively. The abrupt null at  $\phi \approx 135^\circ$  in the co-polarized pattern and the spike at the same location in the cross-polarized pattern are due to discontinuities in the contribution from edge 4 (indicated in Figure 2.8).

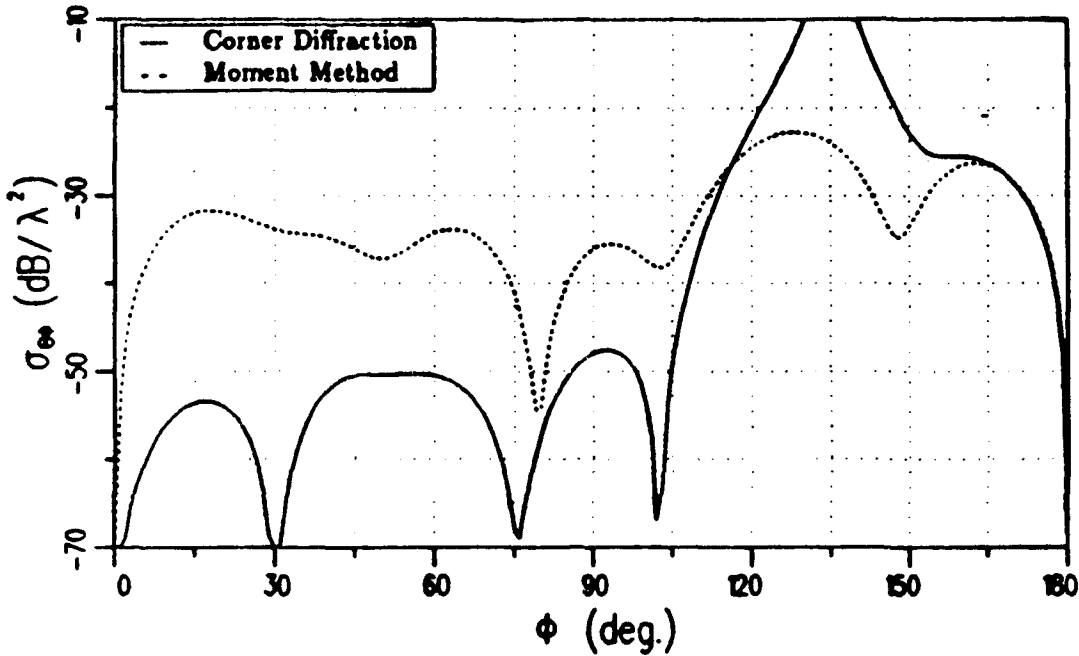


Figure 2.17: RCS for the  $\theta = 89^\circ$  cut of a  $2\lambda$  square plate with a  $\hat{\phi}^i$  polarized fixed source at  $\theta^i = 45^\circ$ ,  $\phi^i = 0^\circ$ .

The point  $\phi \approx 135^\circ$  coincides with  $\beta_4 = \beta'_4$  and  $\phi_4 \approx 0$  where  $\beta_4$ ,  $\beta'_4$ , and  $\phi_4$  are the edge fixed coordinates for edge 4. Due to the geometry  $\hat{\beta}_4 \approx \hat{\phi}$  and  $\hat{\phi}_4 \approx \hat{\theta}$  so the discontinuity in  $\sigma_{\phi\phi}$  is due to the discontinuity in  $D_2^c$  and, likewise, the discontinuity in  $\sigma_{\theta\phi}$  is due to the discontinuity in  $D_h^c$ .

Therefore, the discontinuity in the new diffraction coefficients at the intersection of the Keller cone and the infinite half plane associated with the edge ( $\beta = \beta'$  and  $\phi = 0$ ) may be expected to cause discontinuities or narrow spikes depending on the polarization and the pattern cut. As the examples illustrate these disturbances only affect a typical pattern cut for around  $5^\circ$  to  $10^\circ$ . In addition, they are in the low level regions of the returns.

It is easily seen that the diffraction coefficients  $D_2^c$  and  $D_h^c$  are discontinuous as the source passes through the half plane  $\phi' = \pi$ . In the general case of bistatic scattering, these discontinuities in the sign of the field scattered by a corner will result in discontinuities in the total scattered field. However, the diffraction coefficients are continuous here ( $\phi' = \pi$ ) for the special case of backscatter.

## 2.5 Conclusions

The objective of this chapter has been to compare different methods for the analysis of the high frequency far zone scattering from flat plate and convex flat plate type structures. Ryan and Peters equivalent currents and the previous corner diffraction coefficient are compared with the Michaeli equivalent currents and the new corner diffraction coefficient. The method of moments and measurements are also used to validate the solutions.

It has been shown that for backscatter all the methods compare reasonably within engineering accuracy. For bistatic scattering, however, the two dimensional nature of the old methods lead to inaccuracies. The newer methods, based on more rigorous three dimensional analysis, remove most of these problems.

A new corner diffraction coefficient is presented that provides an efficient and accurate solution to within first order. It provides the same level of accuracy as the Michaeli equivalent currents with the added benefit of not needing integrations for flat plates. All the optics and edge scattering effects have been lumped into the corners of the plate with nice physical interpretations.

## Chapter 3

# Diffraction of Dipole Excited Edge Waves

### 3.1 Introduction

The diffraction of acoustical waves by a conducting elliptic cone and a quarter plane were studied by Krauss and Levine [27] and Radlow [28,29], respectively. Satterwhite and Kouyoumjian [30] analyzed the vector electromagnetic problem and developed a Green's dyadic for a source radiating in the presence of an angular sector. However, their solution, expressed in terms of non-closed form Lamé functions, is cumbersome for numerical calculations. Furthermore, it has not so far appeared possible to asymptotically identify a "tip diffraction coefficient" from this eigenfunction representation.

Burnside and Pathak proposed in [31] a corner diffraction coefficient which successfully predicted the corner effect of several plate structures. Their solution is based on the asymptotic evaluation of the radiation integral involving the equivalent currents that would exist in the absence of the corner. A corner diffraction term is then established by empirically modifying the final result. Sikta [11] applied a limiting process to identify the wave diffracted by the corner and propagating along one of the edges of a polygonal plate. Further, introducing an empirically established "reflection coefficient", he utilized his expression to the calculation of multiple diffractions between adjacent corners of a flat plate.

In this Chapter, the vertex and edge diffraction of an electromagnetic

wave guided along one of the edges of a semi-infinite wedge is studied asymptotically. Explicit expressions of the edge wave are presented in Section 3.2, deduced from the limiting behavior of the Green's dyadic for an infinite wedge [32,33].

A first approximation of the vertex diffracted field is developed in Section 3.4, based on the radiation of the surface current that would be induced by the edge wave for an infinite wedge, which is subsequently truncated. The asymptotic evaluation of the surface current's radiation integral appropriately encounters the edge wave singularity, consistent with Meixner's edge condition. To the field expressions thus derived, a fringe current effect, which is asymptotically incorporated in the radiation integral of Michaeli's fringe edge equivalent currents [7], is superimposed. Edge wave vertex and edge diffraction coefficients can then be established from the asymptotic field expressions. The pertinent analysis is developed in Section 3.5.

The validity of the approach is confirmed via comparison with Method of Moments results and pattern measurements for a small dipole radiating in the close vicinity of one of the edges of a polygonal plate.

## 3.2 Edge Waves

The term "edge waves" in the present work defines waves strongly coupled with the edge of a wedge. The edge wave is a Maxwellian field guided by the edge, exhibits the proper edge singularity and can be excited either by a plane wave at grazing incidence, or by a dipole radiating in the close vicinity of the edge. The vertex of a polyhedron illuminated by a plane or spherical field can also excite an edge wave. Independent of the excitation, but sufficiently far from its source, the edge wave is and can be treated as a ray optical field, i.e., its phase is proportional to the distance from the source (reference) to the observation point and its amplitude varies in such a way that the energy within a tube originated at the source point is preserved. Further, its Poynting vector is radially directed. Application of ray optical techniques is, however, not straightforward, mainly due to the singular behavior of the paraxial fields.

Let us consider the canonical problem of a point electric source  $\vec{j}^e = \vec{p}^e \delta(\vec{r} - \vec{r}')$  that radiates in the presence of a perfectly conducting infinite wedge. The field produced by this dipole-wedge configuration is formally

written

$$\vec{E}(\vec{r}) = j\omega_0\mu_0\vec{\Gamma}(\vec{r};\vec{r}') \cdot \vec{p}^e, \quad (3.1)$$

where  $\vec{\Gamma}(\vec{r};\vec{r}')$  is the Green's dyadic for the wedge [32]. For convenience,

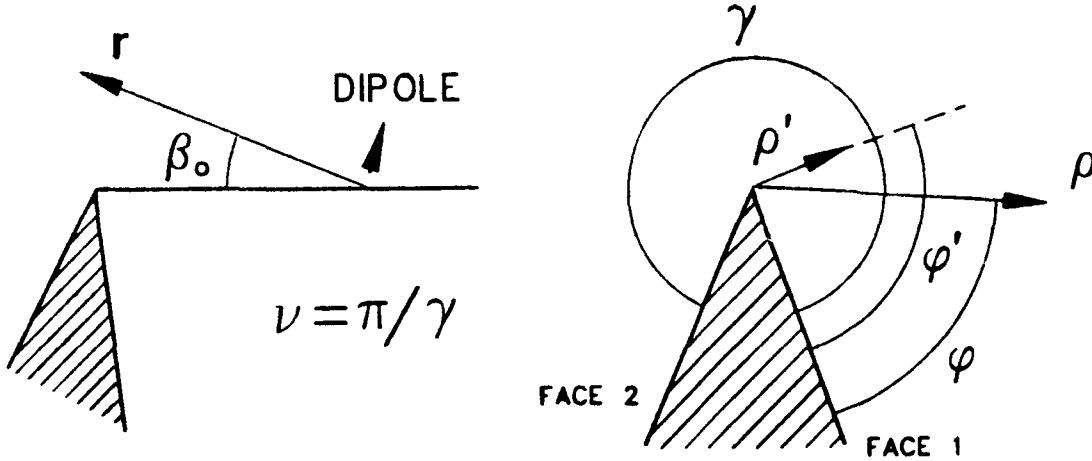


Figure 3.1: Dipole excited edge wave.

the source point is located at  $r' = \rho'$ ,  $\beta' = \pi/2$  in the reference coordinates, with the  $z$ -axis being coincident with the edge and the  $x$ -axis parallel to face 1 of the wedge (Fig. 3.1). The related system of spherical coordinates is  $(r, \beta_0, \phi)$ . The limiting form of the field in eq. (3.1) for small values of the parameter  $\epsilon = k\rho' \sin \beta_0$  is of interest here. Specifically, the Green's dyadic assumes the power series expansion

$$\vec{\Gamma}(\vec{r};\rho',\phi') = \epsilon^{\nu-1} \sum_{m=0}^{\infty} \sum_{n=0}^{\infty} \vec{\Gamma}_{mn}(\vec{r};\rho',\phi') \epsilon^{m\nu+n}, \quad (3.2)$$

where  $\nu = \pi/\gamma$  and  $\gamma$  is the external wedge angle. The dyadic terms  $\vec{\Gamma}_{mn}(\vec{r};\rho',\phi')$ ,  $m = 0, 1, \dots$ ,  $n = 0, 1, \dots$ , can be derived in a straightforward manner, if one substitutes the series expansion of the Hankel functions in the eigenfunction representation of  $\vec{\Gamma}(\vec{r};\vec{r}')$ . At the limit  $\epsilon \rightarrow 0$ , one can retain the leading term in eq. (3.2) to approximate the total field which, for  $kr \gg 1$ , is given by

$$\vec{E}^{ew}(\vec{r}) = jZ_0 k^\nu C(\nu) A_\nu^e(\rho',\phi') \sin^{\nu-1} \beta_0$$

$$(\hat{\beta}_0 \cos \beta_0 \sin \nu \phi + \hat{\phi} \cos \nu \phi) \frac{\exp(-jk r)}{r}, \quad (3.3)$$

where

$$C(\nu) = \frac{j\nu \exp(j\nu\pi/2)}{\pi 2^\nu \Gamma(\nu)} \quad (3.4)$$

and

$$A_\nu^e(\rho', \phi') = (\rho')^{\nu-1} (p_{\rho'}^e \sin \nu \phi' + p_{\phi'}^e \cos \nu \phi') \quad (3.5)$$

is a constant source factor. Eq. (3.3) defines an edge guided wave, which dominates in the paraxial region, revealing the strong coupling between the dipole source and the edge. It is a spherical wave that satisfies Maxwell's equations, the boundary conditions on the perfectly conducting surface, as well as Meixner's edge condition.

In the case of a plane wave at grazing incidence, which is essentially a quasi-two dimensional situation, one can implement a similar limiting procedure on the cylindrical harmonic expansion of the total field [33] to extract the edge wave. In particular, with  $\beta' \rightarrow 0$ , the dominant term in the series expansion of the total field in the neighborhood of the edge equals

$$\vec{E}^{ew}(\vec{\rho}) = -4\pi C(\nu) S(\beta', \phi') (k\rho)^{\nu-1} (\hat{\rho} \sin \nu \phi + \hat{\phi} \cos \nu \phi) \exp(-jkz), \quad (3.6)$$

where  $S(\beta', \phi') = \sin^{\nu-1} \beta' (E_{0\rho'} \sin \nu \phi' + E_{0\phi'} \cos \nu \phi')$  is again an excitation related factor.

Both forms (3.3) and (3.6), although derived from a limiting rather than asymptotic estimation, agree in the paraxial region with the leading term in the asymptotic analysis of Pearson [34].

### 3.3 Diffraction formulation

The study of edge guided waves at an infinite wedge, outlined in the previous section, is not adequate to describe the radiation of a dipole in the close vicinity of one of the edges of a realistic flat plate structure. For instance, regarding the simple trihedral configuration depicted in Fig. 3.2, in addition to a direct field associated with the interaction of the dipole and the neighboring edge, diffracted rays initiated at the tip and the adjacent edges should be introduced in an accurate high frequency solution. Namely, an improved approximation of the total field can be expressed as

$$\vec{E}^t \approx \vec{E}^{ew} \cdot \vec{T} + \vec{E}_1^e + \vec{E}_2^e + \vec{E}^c. \quad (3.7)$$

In the above equation,  $\vec{E}^{ew} \cdot \vec{T}$  constitutes the dipole and guiding edge interaction; in essence, it is a multiplicative correction of the edge wave given by eq. (3.3), by the transition dyadic  $\vec{T}$  to be determined, thus assuring a finite field when  $\beta \approx 0$ , i.e., at the paraxial region of the extension of the edge in free space. In addition,  $\vec{E}_{1,2}^e$  denote edge diffracted fields, while  $\vec{E}^c$  designates the ray emanating from the tip.

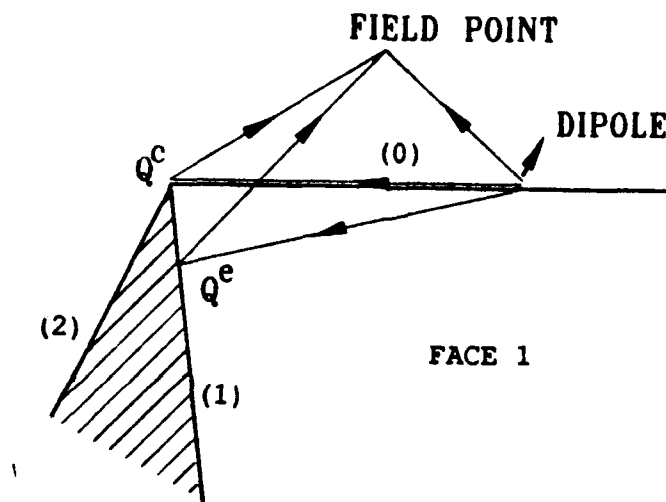


Figure 3.2: Edge wave diffraction at a trihedron.

In principle, if  $\vec{j}(\vec{r}')$  is the total current flowing over the surface  $S$  of the conducting trihedron, then the scattered field can be evaluated via the radiation integral, which, in the Fresnel or Fraunhofer region of the surface, has the form

$$\vec{E}(\vec{s}_c) = jkZ_0 \int \int_S \hat{R} \times \hat{R} \times \vec{j}(\vec{r}') \frac{\exp(-jkR)}{4\pi R} ds' . \quad (3.8)$$

Asymptotic expansion of the above integral by the method of stationary phase [35], in terms of the large parameter  $k$ , should result in isolated mechanisms associated with specific parts of the object and, in our case, corresponding to the diffraction terms in the right hand side of eq. (3.7). However, use of the radiation integral in field calculations, requires a prior knowledge (at least approximate) of the current  $\vec{j}(\vec{r}')$  on  $S$ .

Two successive estimates of the current, resulting in different levels of approximation are introduced. First, it is postulated that, on the faces of the trihedron grazed by the edge wave,  $\vec{j}(\vec{r}')$  can be satisfactorily approximated by the actual induced current (edge wave current) that would flow if the wedge was infinite, while it is presumed zero at the shadowed face of the structure. In particular, for face 1 (Fig. 3.3(a)), we presume

$$\vec{j}_1(\vec{r}') \approx \vec{j}_1^{ew}(\vec{r}') = \hat{n}_1 \times \vec{H}^{ew}(\vec{r}')|_{S_1}, \quad (3.9)$$

where  $\vec{H}^{ew}(\vec{r}')$  is the edge wave at an infinite wedge and  $\hat{n}_1$  is the unit vector normal to face 1.

The asymptotic reduction of the surface integral in eq. (3.8) to a line integral along edges (1) and (2) in Fig. 3.3(b) reveals an equivalence between the radiation of the edge wave surface current (eq. (3.9)) and the Physical Optics equivalent currents in [7], proportional at each point on the edge to the incident edge wave (rather than a plane wave, for which they have been originally developed). Based on this observation, to the truncation effect which results from eq. (3.8), a non-uniform (fringe) current effect induced by edges (1) and (2) is superimposed in a rather indirect way: via the radiation of Michaeli's fringe equivalent currents for edge wave incidence.

In a consistent rationale, one should include a tip excited non-uniform current. But the latter can not be extracted from existing representations of the corner diffraction phenomenon and remains unknown. Numerical results indicate, however, that the present depiction of the currents is sufficient to approximate the diffracted edge waves at the vertex.

### 3.4 The radiation of the edge wave current

Let us consider the radiation of the edge wave current flowing over face 1 of the trihedron. The results for face 2 can be derived by means of a simple transformation. One may introduce the oblique system of coordinates  $(u, t_1)$  associated with edge (1) in Fig. 3.3(a) and defined by the unit vectors

$$\hat{u} = \hat{z}, \quad \hat{t}_1 = \hat{x} \sin \alpha_1 - \hat{z} \cos \alpha_1,$$

with  $\alpha_1$  denoting the angle formed by the guiding edge and edge (1). Sufficiently far from the dipole and employing the results of Section 3.2, one

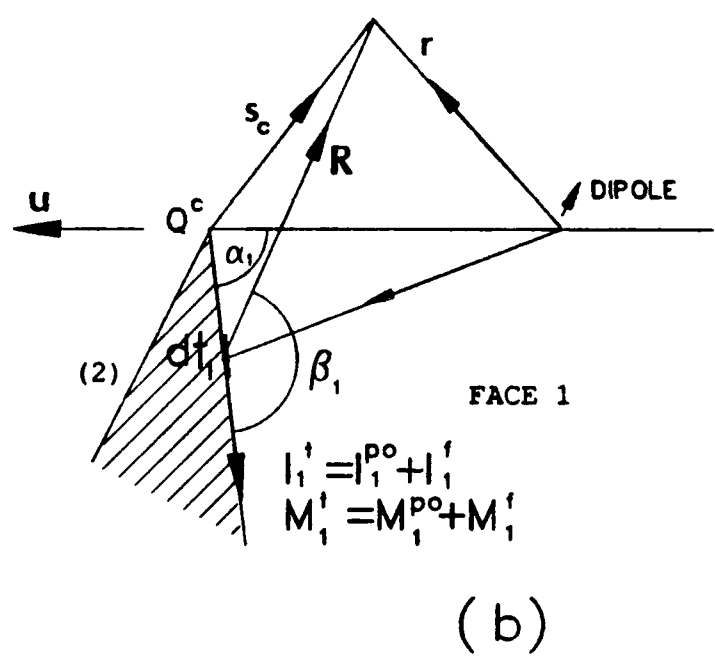
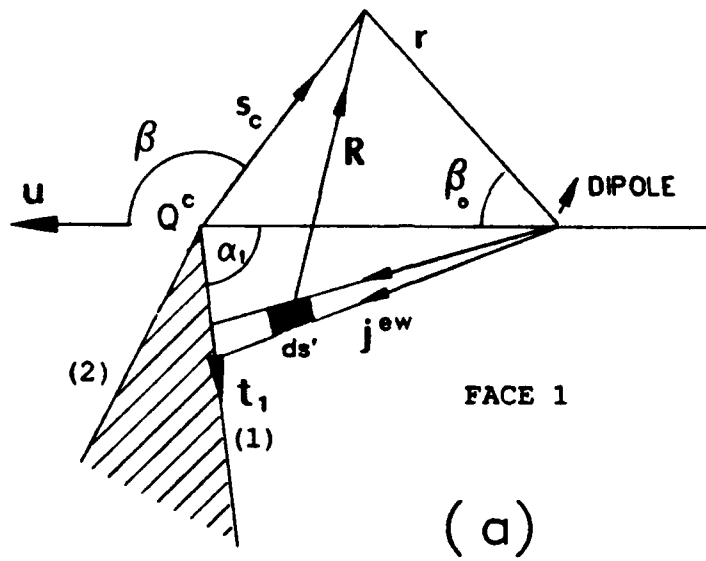


Figure 3.3: Geometry of the edge wave diffraction problem.

observes that

$$\vec{j}_1^{cw}(u, t_1) \approx jk^\nu C(\nu) A_\nu^c(\rho', \phi') \sin^{\nu-1} \theta_0 \frac{\exp(-jk r_0)}{r_0} (\hat{x} \sin \theta_0 + \hat{z} \cos \theta_0), \quad (3.10)$$

in which

$$r_0 = \sqrt{t_1^2 \sin^2 \alpha_1 + (u - t_1 \cos \alpha_1 + s'_c)^2},$$

$$\sin \theta_0 = t_1 \sin \alpha_1 / r_0, \quad \cos \theta_0 = (u - t_1 \cos \alpha_1 + s'_c) / r_0,$$

$s'_c$  is the distance of the dipole source from the vertex and the constant  $C(\nu)$  is defined by eq. (3.4).

The vertex diffracted field of the wedge can be identified asymptotically as the end point contribution to the radiation integral in eq. (3.8). Classically, employing a quadrature expansion of the phase function, one obtains

$$\vec{E}_1^{c,ew}(\vec{s}_c) \approx -\frac{jk^\nu Z_0 \sin^\nu \alpha_1 C(\nu) A_\nu^c(\rho', \phi') F(2kL_c \sin^2 \frac{\beta}{2})}{4\pi s_c (s'_c)^{\nu+1} (1 - \cos \beta)} \cdot \left\{ [s'_c \sin \beta I_{-\nu}^0(k) - (\sin \beta \cos \alpha_1 + \sin \alpha_1 \cos \beta \cos \phi) I_{-\nu-1}^0(k)] \hat{\beta} + \sin \alpha_1 \sin \phi I_{-\nu-1}^0(k) \hat{\phi} \right\}. \quad (3.11)$$

In the above expression,  $I_{-p}^0(k)$  signifies the end point contribution to the integral

$$I_{-p}(k) = \int_0^\infty t^{p-1} \exp\{-jk(R + r_0)|_{u=0}\} dt,$$

which is studied in Appendix A.

For the specific semi-infinite wedge geometry  $I_{-p}^0(k)$  can be approximated by

$$I_{-p}^0(k) \approx \Gamma(p) k^{-p} \exp(jp\pi/2) \exp\{-jk(s_c + s'_c)\} \frac{F_{-p}^c[k a_1^2(\vec{s}_c; s'_c)]}{[\sin \alpha_1 \sin \beta \cos \phi + \cos \alpha_1 (1 - \cos \beta)]^p}, \quad (3.12)$$

in which

$$a_1(\vec{s}_c; s'_c) = -\text{sign}(\pi - \alpha_1 - \beta_1) \left| \sqrt{(s'_c + s_c) - (s'_1 + s_1)} \right| \quad (3.13)$$

and  $s'_1, s_1$  are the distances of the dipole source point and the receiver from the origin  $Q_1^c$  of the Keller cone of diffracted rays initiated at edge (1). The branch of the bracketed expression in the denominator of eq. (3.12) should be chosen according to  $(-1)^p = \exp(jp\pi)$ . The factor  $F(\cdot)$  is the familiar edge transition function of the Uniform Theory of Diffraction (UTD) [16], while the edge wave transition function  $F_{-p}^c(|\cdot|)$  is defined by

$$F_{-p}^c(x) = \exp(jp\pi/4) (2x)^{p/2} \exp(jx/2) \mathcal{D}_{-p}[\exp(j\pi/4)\sqrt{2x}], \quad (3.14)$$

with  $\mathcal{D}_{-p}(\cdot)$  denoting the parabolic cylinder function of order  $-p$  (eq. (A.4)). For  $x > 0$  small we have

$$F_{-p}^c(x) \approx \sqrt{\pi} \exp(jp\pi/4) x^{p/2} \exp(jx/2) \cdot \left[ \frac{1}{\Gamma(\frac{p+1}{2})} - \frac{2 \exp(j\pi/4)}{\Gamma(\frac{p}{2})} \sqrt{x} + \frac{j(p-1/2)}{\Gamma(\frac{p+1}{2})} x + \dots \right] \quad (3.15)$$

and for  $x$  large

$$F_{-p}^c(x) \approx 1 - \frac{p(p+1)}{4jx} - \frac{p(p+1)(p+2)(p+3)}{32x^2} + \dots \quad (3.16)$$

Retaining only the dominant term in the expression of the vertex diffracted wave (dominant with respect to the parameter  $2ks'_c$ ) and with the approximation [36]

$$s'_{1,2} + s_{1,2} \approx (s'_c + s_c) - L_c [1 + \cos(\alpha_{1,2} + \beta_{1,2})],$$

for large values of the distance parameter  $L_c = s_c s'_c / (s_c + s'_c)$ , one obtains the following expression for the vertex diffracted field, in terms of the edges (1) and (2) fixed coordinate systems  $(s_c, \beta_1, \phi_1)$  and  $(s_c, \beta_2, \phi_2)$ , respectively:

$$\begin{aligned} \vec{E}^{c,ew}(\vec{s}_c) \approx & \frac{\exp(j\nu\pi/2) \Gamma(\nu) C(\nu)}{k} \frac{E_{\beta',\phi'}^i(Q^c) \sin \nu\phi' + E_{\phi'}^i(Q^c) \cos \nu\phi'}{\sin^{1-\nu} \beta'} \\ & \cdot \cot \frac{\beta}{2} F(2kL_c \sin^2 \frac{\beta}{2}) \left\{ \frac{\sin^\nu \alpha_1 F_{-\nu}^c[2kL_c \cos^2(\frac{\alpha_1 + \beta_1}{2})]}{(\cos \alpha_1 + \cos \beta_1)^\nu} \right. \\ & \left. + \frac{\sin^\nu \alpha_2 F_{-\nu}^c[2kL_c \cos^2(\frac{\alpha_2 + \beta_2}{2})]}{(\cos \alpha_2 + \cos \beta_2)^\nu} \right\} \frac{\exp(-jk s_c)}{s_c} \hat{\beta}. \quad (3.17) \end{aligned}$$

In eq. (3.17),  $E_{\beta',\phi'}^i(Q^c)$  represent the components of the free space dipole field at  $Q^c$  in the guiding edge fixed coordinate system.

### 3.5 An equivalent current approach

The surface radiation integral in eq. (3.8) asymptotically reduces to a line integral along edges (1) and (2) of the trihedral structure. Thus, the high frequency approximation of the edge and vertex diffracted fields can be viewed as the stationary phase and end point contribution, respectively, of the radiation integral of equivalent line sources "excited" by the impinging edge wave. As far as the edge wave current effect developed in Section 3.4 is concerned, the same expression for the field, excluding the factor  $F[2kL_c \sin^2(\beta/2)]$ , can be obtained via the asymptotic approximation of the line radiation integral of the physical optics components of Michaeli's equivalent currents along edges (1) and (2) and being proportional at each point to the tangential components of the incident edge wave. This observation suggests the addition of a fringe effect to the edge wave current related diffracted field which is, analogously, described by the radiation integral of Michaeli's fringe currents. Although the latter have been derived for plane wave incidence, reasonable results are obtained if one generalizes the concept for arbitrary (non-uniform) ray optical wave fronts and, hence, for an edge wave.

As before, our attention is restricted to face 1 of the wedge. The equivalent edge currents presented in [7] for grazing edge wave incidence at the point  $Q_1$  of edge (1) may be expressed in the form

$$I_1(Q_1) = \frac{2j}{k} \frac{\vec{H}^{ew}(Q_1) \cdot \hat{t}_1}{2} i_1(Q_1), \quad (3.18)$$

$$M_1(Q_1) = \frac{2jZ_0}{k} \frac{\vec{H}^{ew}(Q_1) \cdot \hat{t}_1}{2} m_1(Q_1), \quad (3.19)$$

$\hat{t}_1$  is the unit vector tangent to the edge at  $Q_1$  and  $i_1$ ,  $m_1$  are known and slowly varying functions of the observer's location and the distance of  $Q_1$  from the tip  $Q^c$  of the trihedron. A factor of 1/2 has been also introduced due to grazing incidence.

It is presumed that the edge and vertex diffracted edge wave associated with face 1 of the wedge can be approximated by the radiation integral of the equivalent currents  $I_1(Q_1)$ ,  $M_1(Q_1)$  "flowing" along edge (1), which, in the Fresnel or the Fraunhofer region of the edge, can be explicitly written

as

$$\begin{aligned} \vec{E}_1^d(\vec{s}_c) &\approx jk^\nu Z_0 \sin^\nu \alpha_1 C(\nu) A_\nu^e(\rho', \phi') s'_c \\ &\cdot \int_0^\infty [\hat{R} \times \hat{R} \times \hat{t}_1 i_1(\vec{s}_c; t_1) + \hat{R} \times \hat{t}_1 m_1(\vec{s}_c; t_1)] \\ &\cdot t_1^{\nu-1} \frac{\exp\{-jk(R+r_1)\}}{4\pi R r_1^{\nu+1}} dt_1, \end{aligned} \quad (3.20)$$

with  $R = \|\vec{s}_c - t_1 \hat{t}_1\|$  and  $\hat{R} = (\vec{s}_c - t_1 \hat{t}_1)/R$ .

### 3.5.1 Edge wave vertex diffracted field

The phase of the integrand in (3.20) exhibits a stationary phase point in the neighborhood of an end point, the latter being coincident with the branch singularity of the integrand. Therefore, for large values of the parameter  $k$  the asymptotic evaluation of the integral reveals a vertex contribution as well as an edge diffracted term, if

$$\cos \alpha_1 (1 - \cos \beta) + \sin \alpha_1 \sin \beta \cos \phi > 0,$$

i.e., if  $Q_1^c$  lies on edge (1) itself rather than on its extension. From the leading term in the asymptotic expansion of the integral in (3.20), one obtains the following approximation of the vertex diffracted field (associated with face 1):

$$\begin{aligned} \vec{E}_1^c(\vec{s}_c) &\approx \exp\{j(\nu+1)\pi/2\} \Gamma(\nu) C(\nu) Z_0 A_\nu^e(\rho', \phi') \\ &\cdot \frac{\exp\{-jk(s_c + s'_c)\}}{4\pi s_c (s'_c)^\nu} \frac{\vec{G}_1^c(\vec{s}_c) F_{-\nu}^c[ka_1^2(\vec{s}_c; s'_c)]}{[\cot \alpha_1 (1 - \cos \beta) + \sin \beta \cos \phi]^\nu}, \end{aligned} \quad (3.21)$$

in which we have substituted

$$\vec{G}_1^c(\vec{s}_c) = \hat{s}_c \times \hat{s}_c \times \hat{t}_1 i_1(Q^c) + \hat{s}_c \times \hat{t}_1 m_1(Q^c). \quad (3.22)$$

The previous discussion also suggests the decomposition

$$\left\{ \begin{array}{l} i_1(Q^c) \\ m_1(Q^c) \end{array} \right\} = \left\{ \begin{array}{l} i_1^f(Q^c; \mu_1^f) \\ m_1^f(Q^c; \mu_1^f) \end{array} \right\} + \left\{ \begin{array}{l} i_1^{po}(Q^c; \mu_1^{po}) \\ m_1^{po}(Q^c; \mu_1^{po}) \end{array} \right\}. \quad (3.23)$$

$i_1(Q^c)$ ,  $m_1(Q^c)$ ,  $i_1^{po,f}(Q^c; \mu_1^{po,f})$ ,  $m_1^{po,f}(Q^c; \mu_1^{po,f})$  can be found in [7] along with the definitions (3.18), (3.19).

The parameters  $\mu_1^{po,f}$  involved in the expressions of the edge equivalent currents depend on the choice of the edge fixed coordinate system and, in particular, on the angle between the tangent to the edge at  $Q_1$  and the unit vector  $\hat{\sigma}$  tangent to face 1 at  $Q_1$  which may be chosen arbitrarily. When the currents are truncated to reveal an end point effect, one should be cautious about the choice of the parameters  $\mu_1^{po,f}$ , i.e., the choice of the edge fixed coordinate system, so that the terminated equivalent edge currents represent correctly the end point effect of the truncated, by the edges of the trihedron, true surface induced currents. Within this context, a correct choice of the parameter  $\mu_1^{po}$  for the physical optics component of the equivalent currents is

$$\mu_1^{po} = \frac{\sin \alpha_1 \sin \beta_1 \cos \phi_1 + \cos \alpha_1 (\cos \beta_1 + \cos \alpha_1)}{\sin^2 \alpha_1}, \quad (3.24)$$

so that the unit vector  $\hat{\sigma}$  is parallel to the guiding edge, whereas for the fringe currents the proper choice is

$$\mu_1^f = \frac{\sin \alpha_1 \sin \beta_1 \cos \phi_1 - \cos \alpha_1 (\cos \beta_1 + \cos \alpha_1)}{\sin^2 \alpha_1} \quad (3.25)$$

and now  $\hat{\sigma}$  is parallel to the edge diffracted ray from  $Q^c$  that grazes face 1.

Not surprisingly, using eq. (3.24) for the definition of the parameter  $\mu_1^{po}$  in the expressions of the physical optics equivalent edge currents one finds

$$\vec{G}_1^{c,ew}(\vec{s}_c) = -\hat{\beta} \cot \frac{\beta}{2}, \quad (3.26)$$

so that the vertex diffracted field assumes the approximation

$$\vec{E}_1^c(\vec{s}_c) \approx \vec{E}_1^{c,ew}(\vec{s}_c) + \vec{E}_1^{c,f}(\vec{s}_c) \quad (3.27)$$

in which  $\vec{E}_1^{c,ew}(\vec{s}_c)$  is identical with the term associated with face 1 in (3.17), while the fringe current related wave equals

$$\begin{aligned} \vec{E}_1^{c,f}(\vec{s}_c) \approx & \exp\{j(\nu + 1)\pi/2\} \Gamma(\nu) C(\nu) Z_0 A_\nu^c(\rho', \phi') \sin^\nu \alpha_1 \\ & \frac{\exp\{-jk(s_c + s'_c)\} \vec{G}_1^{c,f}(\vec{s}_c) F(2kL_c \sin^2 \frac{\theta}{2}) F_{-\nu}^c[ka_1^2(\vec{s}_c; s'_c)]}{4\pi s_c (s'_c)^\nu (\cos \alpha_1 + \cos \beta_1)^\nu}. \end{aligned} \quad (3.28)$$

The vector function  $\vec{G}_1^{c,f}(\vec{s}_c)$  is related with Michaeli's equivalent currents at  $Q^c$  via the equation

$$\vec{G}_1^{c,f}(\vec{s}_c) = i_1^f(Q^c; \mu_1^f) \hat{s}_c \times \hat{s}_c \times \hat{t}_1 + m_1^f(Q^c; \mu_1^f) \hat{s}_c \times \hat{t}_1. \quad (3.29)$$

The above expressions simplify considerably for the case of the plane angular sector, with  $\alpha_1 = \alpha_2 = \alpha$ ,  $a_1 = a_2 = a$ . Without presenting the details of the derivation, which involves only elementary manipulations, for the field related with the fringe currents one finds

$$\begin{aligned} \vec{E}^{c,f}(\vec{s}_c) &\approx \frac{-jZ_0}{\sqrt{2}\pi} A_{1/2}^c(\rho', \phi') \frac{\exp\{-jk(s_c + s'_c)\}}{4\pi s_c \sqrt{s'_c}} \\ &\cdot \frac{\vec{G}^{c,f}(\vec{s}_c; \alpha) F(2kL_c \sin^2 \frac{\beta}{2}) F_{-1/2}^c[ka^2(\vec{s}_c; s'_c)]}{\sqrt{\cot \alpha(1 - \cos \beta) + \sin \beta \cos \phi}}, \end{aligned} \quad (3.30)$$

where the function  $G^{c,f}(\vec{s}_c)$  is given by

$$\vec{G}^{c,f}(\vec{s}_c) = \frac{1}{\cos(2\alpha) + \cos \delta} \left[ -\hat{\beta} \sin \beta + \frac{\hat{\beta} e_\beta(\beta, \phi) + \hat{\phi} e_\phi(\beta, \phi)}{\sin^2 \alpha \sin \beta_1 \cos(\delta/2)} \right], \quad (3.31)$$

with

$$\cos \delta = \sin(2\alpha) \sin \beta \cos \phi - \cos(2\alpha) \cos \beta, \quad (3.32)$$

$$\begin{aligned} e_\beta(\beta, \phi) &= -(\cos \alpha + \cos \beta_1) (\sin \alpha \cos \beta \cos \phi + \cos \alpha \sin \beta) \\ &\cdot [\sin \alpha \cos \phi_1 (1 - \cos \alpha \cos \beta_1) - \cos^2 \alpha \sin \beta_1] \\ &+ \sin^5 \alpha \sin \phi \sin \phi_1, \end{aligned} \quad (3.33)$$

$$\begin{aligned} e_\phi(\beta, \phi) &= \sin \alpha \sin \phi (\cos \alpha + \cos \beta_1) \\ &\cdot [\sin \alpha \cos \phi_1 (1 - \cos \alpha \cos \beta_1) - \cos^2 \alpha \sin \beta_1] \\ &+ \sin^4 \alpha \sin \phi_1 (\sin \alpha \cos \beta \cos \phi + \cos \alpha \sin \beta). \end{aligned} \quad (3.34)$$

For the particular case of the right angle sector ( $\alpha = \pi/2$ ), it readily follows that

$$\vec{G}^{c,f}(\vec{s}_c; \pi/2) = \hat{\beta} \left( \cot \frac{\beta}{2} - \csc \frac{\beta}{2} \right) \quad (3.35)$$

and the total tip diffracted field assumes the simple representation

$$\vec{E}^c(\vec{s}_c) \approx \frac{-jZ_0}{\sqrt{2}\pi} A_{1/2}^c(\rho', \phi') \frac{\exp\{-jk(s_c + s'_c)\}}{4\pi s_c \sqrt{s'_c}} \cdot \frac{F(2kL_c \sin^2 \frac{\beta}{2})}{\sin \frac{\beta}{2}} \frac{F_{-1/2}^c[kL_c(1 - \sqrt{1 - \sin^2 \beta \cos^2 \phi})]}{\sqrt{\sin \beta \cos \phi}} \hat{\beta}. \quad (3.36)$$

### 3.5.2 Edge wave edge diffracted field

It can be shown that the edge diffracted field, i.e., the stationary phase contribution to the radiation integral of Michaeli's equivalent currents, is the edge diffracted edge wave predicted by UTD, multiplicatively corrected by the transition function

$$F_{\nu-1}^c[2kL_{e_1} \cos^2 \left( \frac{\alpha_1 + \beta_1}{2} \right)],$$

where

$$F_{\nu-1}^c(\cdot) = [F_{\nu-1}^c(\cdot)]^* \quad (3.37)$$

with the star denoting complex conjugate. The large parameter  $L_{e_1}$  equals

$$L_{e_1} = \frac{s_1 s'_1}{s_1 + s'_1}. \quad (3.38)$$

The transition function  $F_{\nu-1}^c(\cdot)$  guarantees the finiteness of the edge diffracted edge wave as  $Q_1^e \rightarrow Q^c$  and the uniformity (continuity) of the total field as the "shadow boundary" of the edge diffracted rays (the cone  $[\cot \alpha_1(1 - \cos \beta) + \sin \beta \cos \phi] = 0$ ) is crossed. It appears as a type of caustic correction factor in the sense that it compensates the singularity of the edge diffracted field at the extension of the guiding edge. However, in our case the singularity arises from the behavior of the incident field on the edge rather than the focusing of the diffracted rays into a caustic.

### 3.5.3 A heuristic correction factor for the direct edge wave

As already pointed out, the rigorous solution of the radiation of a dipole in the presence of an infinite wedge predicts a singular field at the edge

of the wedge, in consistency with Meixner's edge condition. However, for a semi-infinite structure (trihedron), the singularity of the edge wave at the extension of the guiding edge ( $\beta \approx 0$ ) in free space is not physically acceptable. To overcome this discrepancy, the multiplicative correction of the edge wave associated with a semi-infinite or finite edge with the use of a suitable transition function (in general a dyadic) has been suggested. Such a transition function can be empirically derived by requiring the continuity of the total field at the shadow boundaries of the direct wave (edge wave), namely at the planes  $\phi_{1,2} = \pi$ . This continuity was guaranteed by the UTD evaluation of the edge diffracted field, but it is violated in the paraxial region after the introduction of the function  $F_{\nu-1}^e$ , which assures the uniformity of the total diffracted field. Obviously, the edge wave can be multiplied by a similar transition function so that the total field retains its continuity in the paraxial region as well as outside of it, where the transition function approaches unity. In addition, such a multiplicative correction would yield a finite total field along the extension of the edge in free space.

In particular, for the plane angular sector, a convenient modification of the edge wave, in the extension of the guiding edge, reads

$$\begin{aligned} \vec{E}^{ew}(\vec{s}_c) \approx & -\frac{\sqrt{k}Z_0 \exp(j\pi/4)}{2\pi\sqrt{2\pi}} A_{1/2}^e(\rho', \phi') \\ & \cdot [\hat{\beta}_0 \cos \beta_0 \sin(\phi/2) + \hat{\phi} \cos(\phi/2)] \frac{F_{-1/2}^e[2kL_e \sin^2 \frac{\beta_0}{2}] \exp(-jk s_0)}{\sqrt{\sin \beta_0} s_0}, \end{aligned} \quad (3.39)$$

with  $s_0$  denoting the distance of the observation point from the dipole and  $\beta_0$  is the elevation angle of the observer in the guiding edge fixed coordinate system centered at the point of the projection of the dipole onto the edge.

### 3.6 Discussion and numerical results

The edge wave vertex diffracted field is a higher order term with respect to the large parameter  $k$  in the asymptotic solution of the radiation of a dipole in the vicinity of the edge of a trihedron. Nonetheless, it contributes significantly to the  $\hat{\beta}$ -directed component of the field, especially in the paraxial

region of the guiding edge and along its extension. This is due to the accumulation of electric current flow lines in the vicinity of the guiding edge excited by the ray optical edge wave.

The solution, based on Michaeli's equivalent currents, is essentially an asymptotic PTD (Physical Theory of Diffraction) approach, in that a fringe current effect due to the terminating edges is added to the edge wave currents, cast finally into a UTD form. Although, the derivation of the fringe edge currents assume an infinite edge and uniform plane wave illumination, the field is expected to retain its singular behavior in the vicinity of the vertex, which, moreover, does not contradict the "tip condition" (i.e., the behavior of the field in the neighborhood of a vertex) as investigated by several authors. It should be emphasized that the approximations attempted in Sections 3.4 and 3.5 by no means present a complete rigorous representation of the tip diffracted field, but it merely includes the information of the truncation of known components of the currents flowing over the wedge surface.

The patterns of the total diffracted field predicted from the edge wave current radiation integral and the equivalent source approximation, for the configuration shown in Fig. 3.4(b), are compared in Fig. 3.4(a). Clearly, the tip effect of the edge wave currents does not compensate the discontinuity of the edge wave edge diffracted field. On the other hand, the equivalent currents result yields a continuous pattern across the shadow boundary cone of the terminating edge diffracted rays, and appears as a more complete representation of the diffraction effects.

Comparisons of the calculated field (which includes only the two edge wave tip diffracted terms corresponding to the two adjacent corners added to the modified direct edge wave) via Michaeli's equivalent currents (denoted as MEC on the graphs) and the edge wave current approach (EWC) with Method of Moments results (MM) are made in Figs. 3.5-3.7, for a  $4\lambda$  square plate. The dipole has been placed in the close vicinity of one of the edges ( $\rho' = 0.01\lambda$ ) of the plate and sufficiently far from its corners ( $s'_c = 2\lambda$ ). The direct edge wave (EW) (eq. (3.3)) is also plotted so that the effect of the corner diffracted fields is better illustrated. Note that in Fig. 3.7 (where  $\phi = 45^\circ$ ) the edge wave edge diffracted fields should be also added to the corner diffracted fields. The agreement is good, especially in regions where contributions from other diffraction mechanisms other than the corner adjacent to the guiding edge are known to be negligible. In fact,

as shown in Figs. 3.5–3.7, the agreement between the Method of Moments data and the calculated field progressively improves for larger values of the  $\phi$  angle. For  $\phi = 45^\circ$  (Fig. 3.7), other mechanisms such as diffraction from the remote corners of the square plate as well as double and triple edge diffraction may contribute significantly to the pattern. Our approximation also improves when the paraxial region is approached ( $\beta \rightarrow 0^\circ, 180^\circ$ ), where, as a matter of fact, the total field is stronger. The latter justifies the validity of the asymptotic analysis which resulted in the multiplication of two transition functions as well as the choice of the correction factor for the direct dipole field. Unfortunately, the  $\hat{\phi}$ -directed field does not exhibit an analogous agreement (Fig. 3.8), at lower azimuthal cuts, mainly due to the fact that other mechanisms contribute significantly to the pattern of that polarization. However, the small angular variation of the pattern, which is a typical  $\hat{\phi}$  component pattern for  $\phi > 90^\circ$ , indicates that the corner associated  $\hat{\phi}$ -directed fields are sufficiently weaker compared with the  $\hat{\phi}$  component of the direct edge wave and can be neglected in practical calculations.

The results also reveal a small variation of the total field with respect to the azimuthal coordinate (angle  $\phi$ ), in contrast with the relative large changes of the calculated pattern in the elevation plane. The  $\phi$  dependence becomes significant only at lower cuts where the contribution from the opposite edge and its two adjacent corners is appreciable.

The second example examined also involves the radiation of a small monopole in the close vicinity of one of the edges of a rectangular plate ( $\rho' = 0.01\lambda$ ), but now with different distances from the two adjacent corners ( $s'_{c_1} = 2\lambda$ ,  $s'_{c_2} = 3\lambda$ ). The calculated field, which again includes two tip diffracted rays in addition to the direct edge wave, is compared with Method of Moments results as well as measured data, as shown in Figs. 3.9 and 3.10 in the azimuthal planes  $\phi = 180^\circ$  and  $\phi = 150^\circ$ , respectively. The accuracy of the measurement deteriorated at smaller azimuthal angles, where the support structure influenced significantly the measured radiation pattern. The measured data in Fig. 3.9 was obtained with an absorbing material (RAM) around the remote corners and the opposite edge of the rectangular plate, so that the pattern is more closely related to the calculated field, which again includes two adjacent tip diffracted rays in addition to the direct edge wave. Clearly, the agreement is better in this case, in contrast with the results of Fig. 3.10 where the RAM has been removed.

It should be noted that neither the edge wave current solution nor the equivalent source formulation are expected to yield accurate results for small angular sector angles ( $\alpha \ll \pi/2$ ). In this case a strong coupling between the two edges forming the sector occurs, which is not encountered in the evaluation of the radiation integral of the currents flowing along the edge (1). Moreover, when  $\alpha \rightarrow \pi$ , the edge wave currents associated tip diffracted field vanishes and the total solution reduces to the edge wave over an infinite wedge, whereas the same property is not true for the equivalent current formulation of the vertex diffracted field. The latter, therefore, fails in cases of very wide angles, which require a more careful treatment.

It should be finally noted that the analysis related with a dipole excited edge wave can be easily extended to treat the diffraction of an edge wave of the form (3.6). However, the problem of a plane wave at grazing incidence on an infinite or semi-infinite wedge is of rather less practical importance than that of edge-on incidence for a finite structure.

### 3.7 Summary

Our major objective was to describe approximately the edge wave diffraction mechanisms associated with the interaction of an edge wave and the vertex of a trihedron as a first step towards the study of more complex geometries. To approximate the vertex diffracted wave a UTD solution was developed based on a PTD like approach to defining the currents. The addition of a fringe current component flowing in the vicinity of the terminating edges yields a continuous radiation pattern across the shadow boundaries of the edge diffracted waves. Although, the approach is neither rigorous nor complete from a PTD point of view it yields comparable results with the Method of Moments as well measured data and can be used as a first approximation to the edge wave diffraction problem.

The extension of the results of this Chapter for the case of tip excited edge waves and the study of the edge wave diffraction mechanisms associated with an edged body illuminated by a plane wave, which are of particular importance when edge-on incidence is approached, is investigated in Chapter 4.

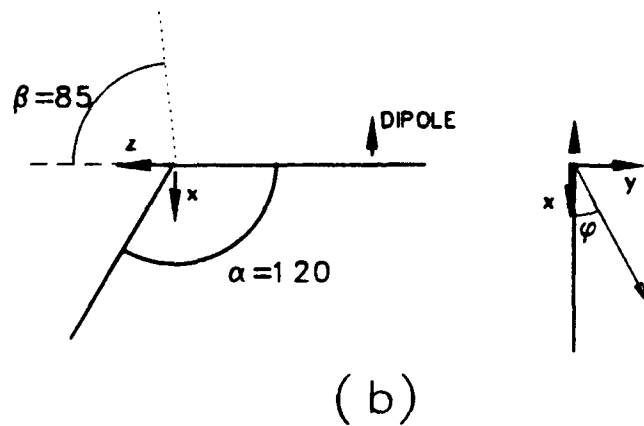
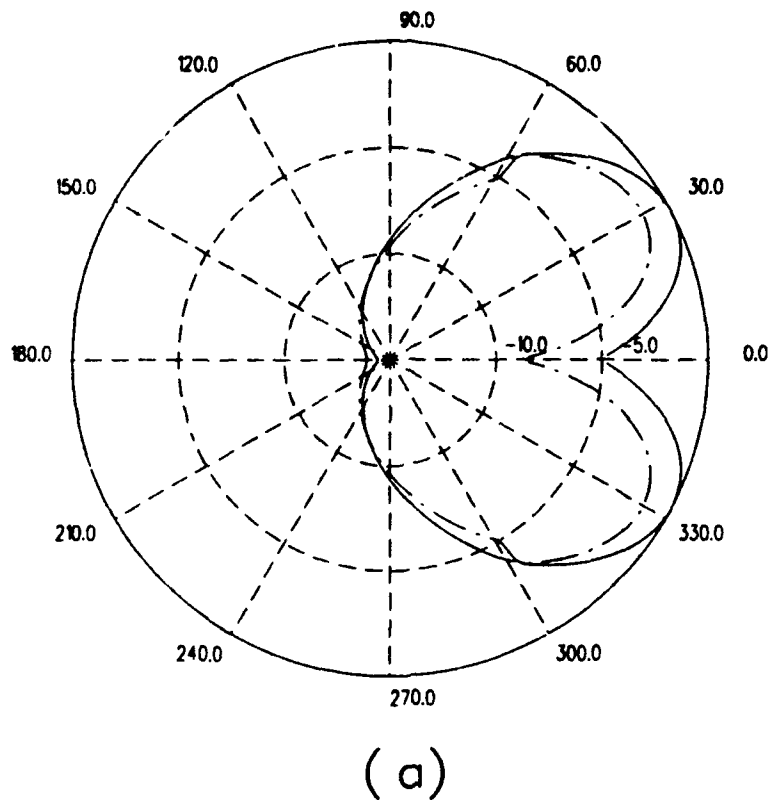


Figure 3.4: (a) Angular section Geometry. (b) Far region edge and vertex diffracted  $\hat{\beta}$ -directed field at the cone  $\beta = 85^\circ$ : dotted line - edge wave current solution, solid line - edge wave and fringe current solution.

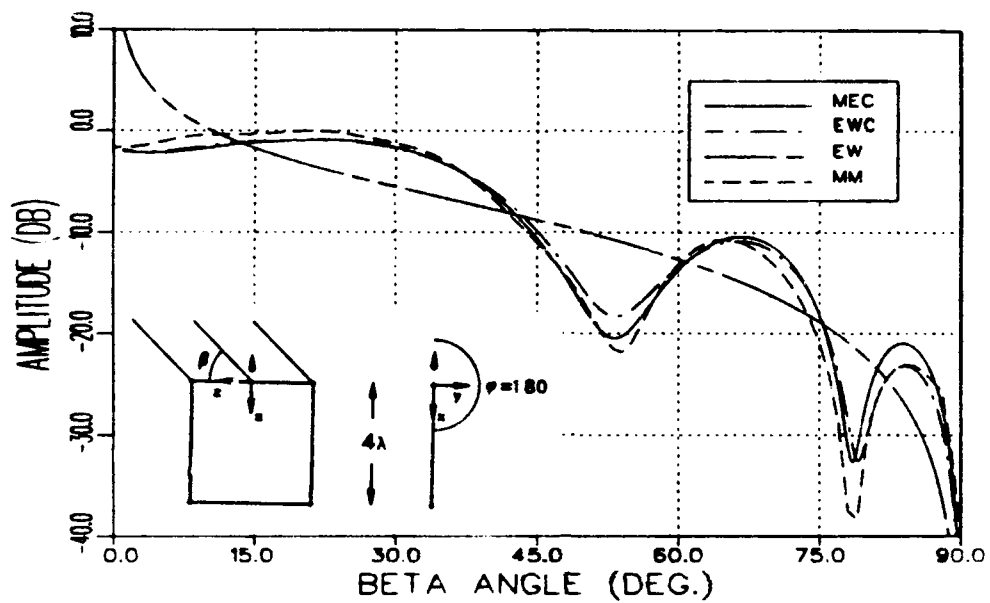


Figure 3.5: Far field  $\hat{\beta}$ -directed wave at the azimuthal cut  $\phi = 180^\circ$  (normalized to 2.3dB).

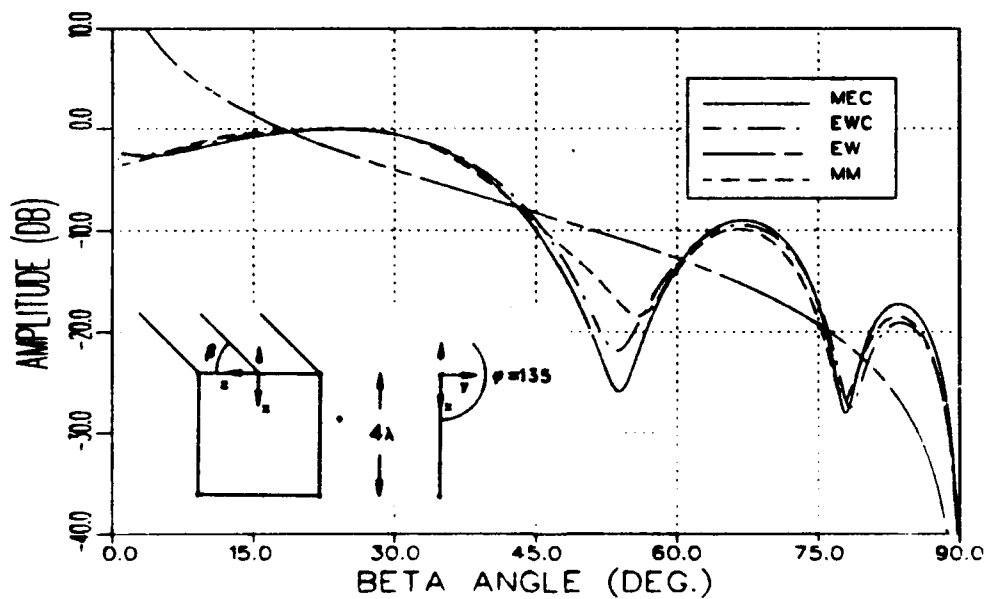


Figure 3.6: Far field  $\hat{\beta}$ -directed wave at the azimuthal cut  $\phi = 135^\circ$  (normalized to 1.9dB).

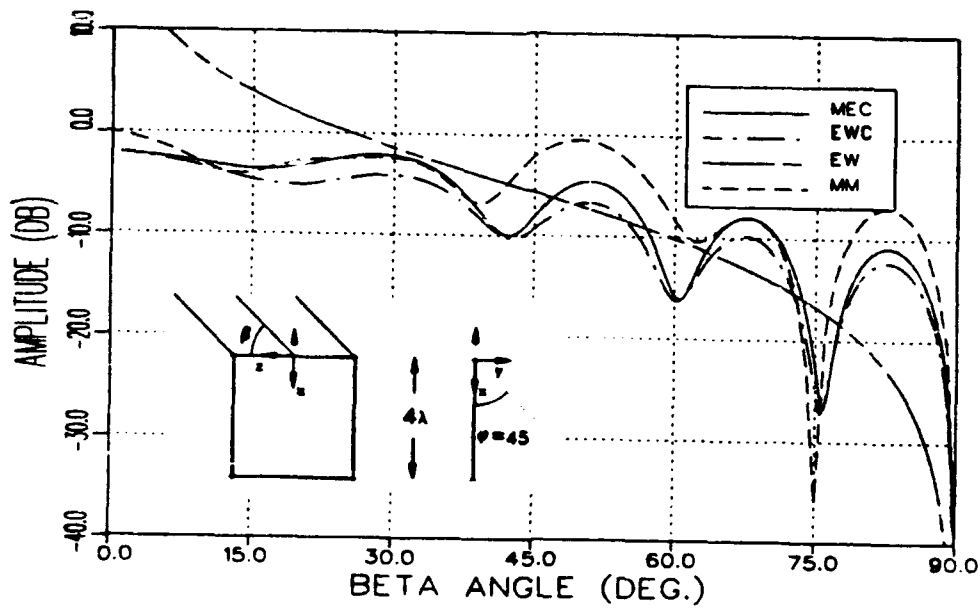


Figure 3.7: Far field  $\hat{\beta}$ -directed wave at the azimuthal cut  $\phi = 45^\circ$  (normalized to -2.0dB).

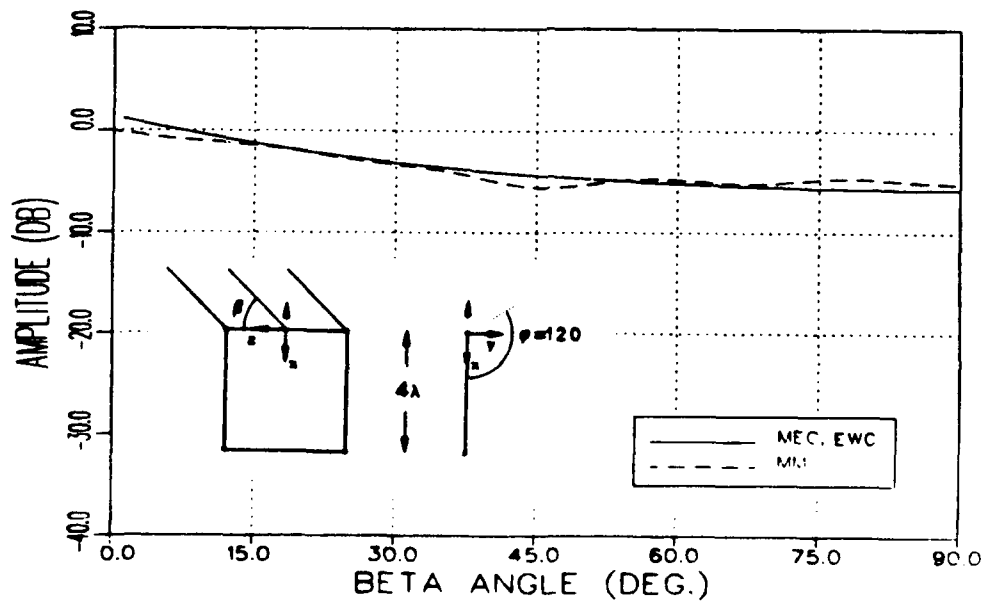


Figure 3.8: Far field  $\hat{\phi}$ -directed wave at the azimuthal cut  $\phi = 120^\circ$ .

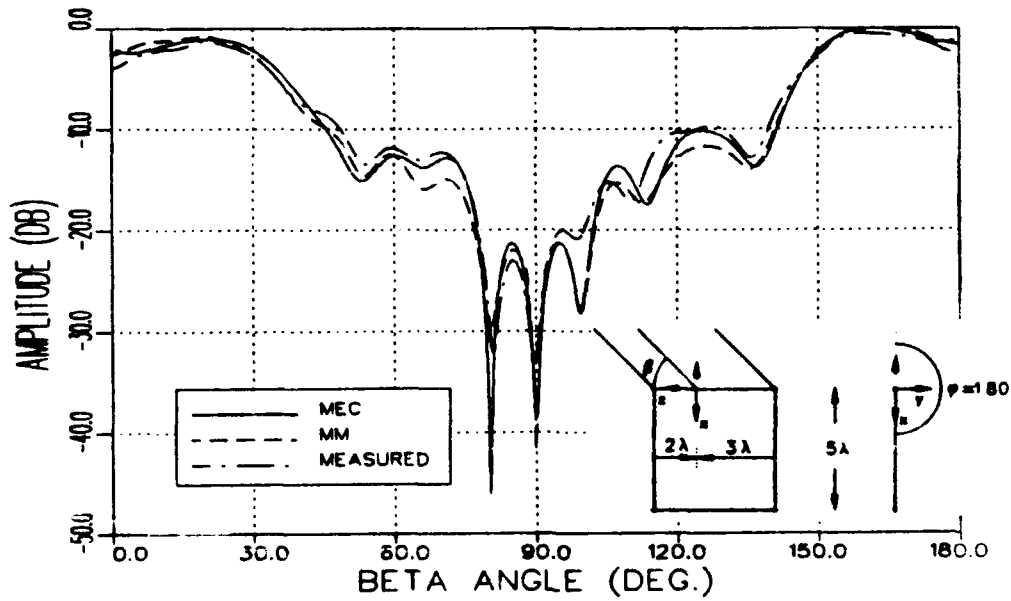


Figure 3.9: Far field  $\hat{\beta}$ -directed wave at the azimuthal cut  $\phi = 180^\circ$  (normalized to 5dB).

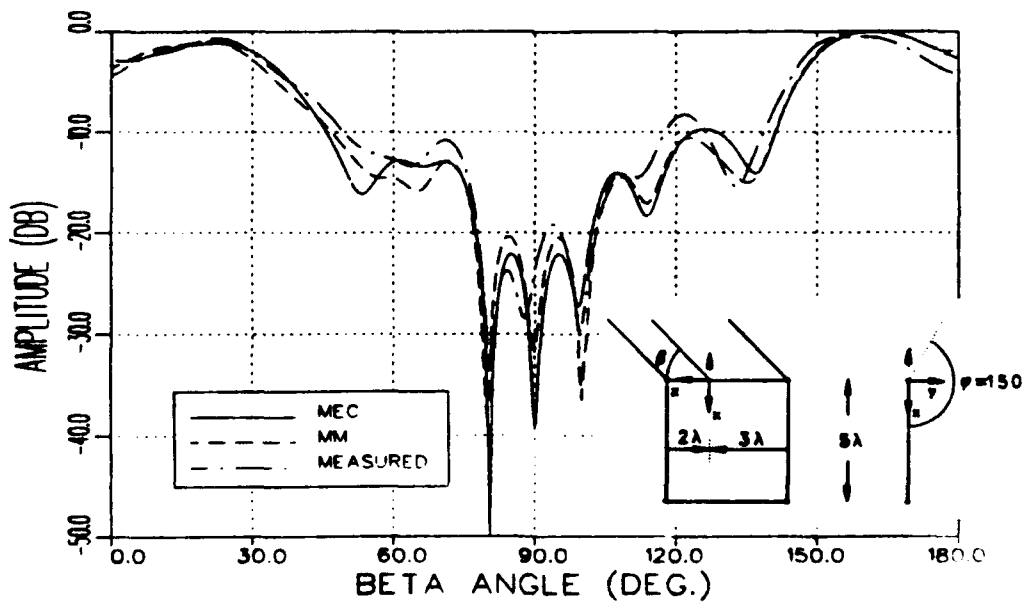


Figure 3.10: Far field  $\hat{\beta}$ -directed wave at the azimuthal cut  $\phi = 150^\circ$  (normalized to 3.0dB).

## Chapter 4

# Edge Wave Mechanisms for Polyhedral Structures

### 4.1 Introduction

Experimental evidence (e.g., impulse response of a square plate) indicates that edge wave diffraction mechanisms become significant when edge on incidence is approached and, in many circumstances, dominate the lower level regions of the monostatic and bistatic cross section of edged structures. Therefore, the incorporation of this type of mechanisms in cross section computations serve as an additive correction to the corner diffraction solution developed by Brinkley and Marhefka [2].

The edge wave diffraction phenomenon on flat plates has been recently studied by Sikta [11]. His solution, although it provided reasonable agreement in several cases, is based, as already pointed out, on an empirical corner diffraction expression, while his study of multiple interactions required the heuristic introduction of a "reflection coefficient". A brief outline of his formulation of the problem is presented in Section 4.2, so that comparisons against the present development can be made.

In Section 4.3 the tip excited edge wave and the associated interactions between two adjacent vertices of a polyhedral structure are examined, employing the more complete depiction of the corner effect developed in Chapter 3, along with reciprocity, and based on plausible heuristic arguments. Specifically, in high frequencies the vertex formed by the intersection of three plates can be considered as the tip of an ideal trihedron (semi-infinite

wedge). Hence, when a ray optical field impinges onto the tip, an edge wave is excited that can be determined via reciprocity from the expressions of the edge wave vertex diffracted field. The edge wave itself is ray optical and hitting an adjacent corner it is rediffracted accordingly.

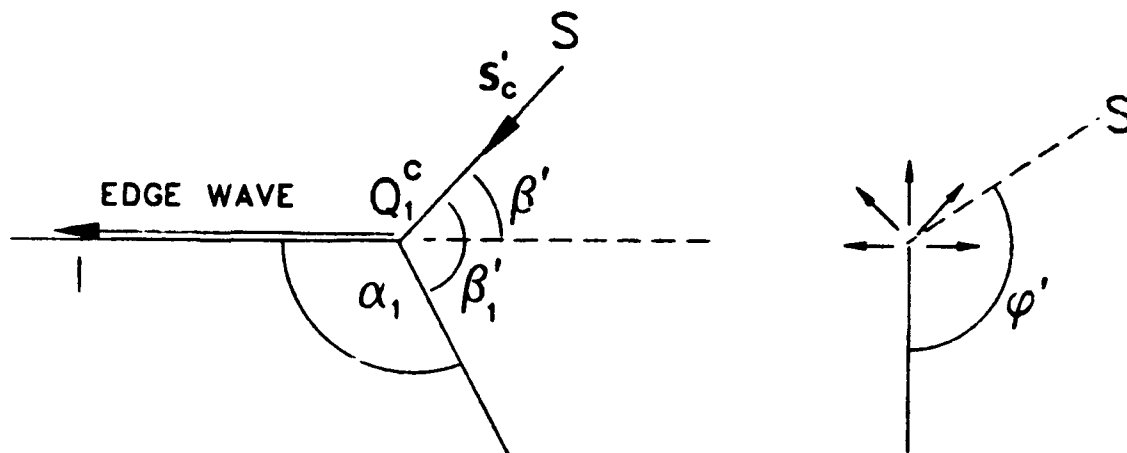


Figure 4.1: Corner excited edge wave.

## 4.2 Sikta's formulation

The edge wave excited by the tip  $Q_1^c$  and propagating along the edge of the plate is as shown in Fig 4.1. According to Sikta, it is determined to be

$$\begin{Bmatrix} E_{\rho_e}^{ew} \\ E_{\phi}^{ew} \end{Bmatrix} = \begin{Bmatrix} E_{\beta'}^i, D_s^{ew}(s'_c; l, \phi_e) \\ E_{\beta_1'}^i, D_h^{ew}(s'_c; l, \phi_e) \end{Bmatrix} \sqrt{\frac{s'_c}{l(l+s'_c)}} \exp(-jkl), \quad (4.1)$$

in which the edge wave launching coefficients  $D_{s,h}^{ew}$  are defined by

$$D_s^{ew}(s'_c; l, \phi_e) = \frac{\exp(-j\pi/4)}{2\sqrt{2\pi k}} \frac{1 + \cos \beta'}{\sin(\beta'/2)} \cdot F \left( 2kL'_c \sin^2 \frac{\beta'}{2} \right) \begin{Bmatrix} \sin(\phi'/2) \sin(\phi_e/2) \\ \cos(\phi'/2) \cos(\phi_e/2) \end{Bmatrix}. \quad (4.2)$$

In the above expressions

$$L'_c = \frac{l s'_c}{l + s'_c}, \quad (4.3)$$

$s'_c, \beta', \phi'$  are the coordinates of a dipole source in the edge fixed coordinate centered at  $Q^{c1}$ , while  $l$  is the length along the edge from the tip and  $\phi_e$  is the azimuth angle of a point close to the edge. Note that Sikta's expression, although it appears to have the correct  $\phi_e$  and  $l$  dependence characteristic of an edge wave, it does not exhibit the proper edge singularity.

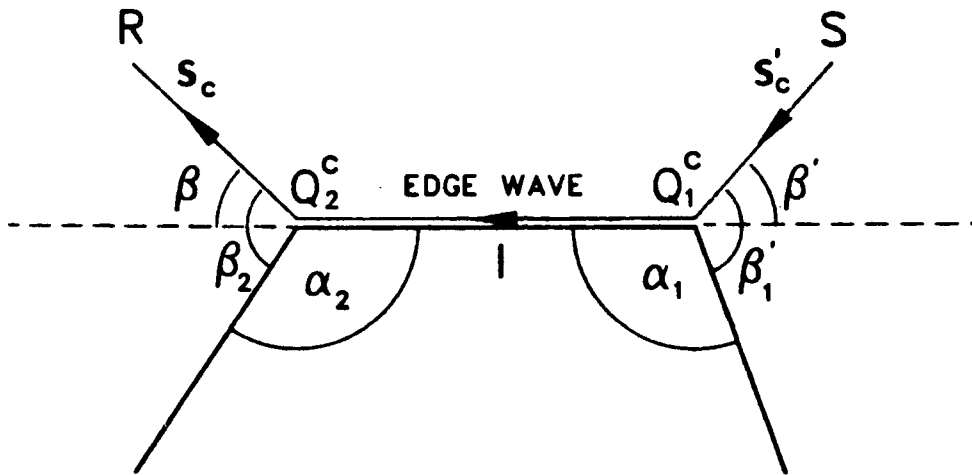


Figure 4.2: Geometry of the corner-to-corner edge wave interaction.

Two adjacent corners of a flat plate, along with the involved geometric quantities, are illustrated in Fig. 4.2. The source point is again located at  $S(s'_c, \beta', \phi')$  with respect to the guiding edge fixed spherical coordinate system centered at the tip  $Q^{c1}$ , while the location  $R(s_c, \beta, \phi)$  of the receiver is defined in terms of an edge fixed coordinate system with its origin at the point  $Q^{c2}$ . The field  $\vec{E}^{c1c2}$ , produced by edge wave diffraction at  $Q^{c2}$ , the edge wave being excited by the tip  $Q^{c1}$  due to source illumination and guided along the edge, is of interest here. It is noted that the total double corner interaction should include also a ray  $\vec{E}^{c2c1}$  along the path  $SQ^{c2}Q^{c1}R$ .

The far field analysis of the edge wave mechanisms, always in the context of Sikta's analysis, involves the multiplication of the incident field

$E_{\beta'}^i, E_{\phi'}^i$ , with the diffraction coefficients in eq. (4.2) and a reflection coefficient, which, for a right angled corner, should read

$$R = \frac{\exp(-j\pi/4)}{\sqrt{2\pi kl}}. \quad (4.4)$$

Specifically, the edge wave diffraction by two adjacent corners in a rectangular plate becomes

$$\begin{aligned} \vec{E}^{c_1 c_2} = & \left\{ \begin{array}{cc} D_s^{ew}(\vec{s}_c; l, \frac{\pi}{2}) R D_s^{ew}(\vec{s}'_c; l, \frac{\pi}{2}) & D_s^{ew}(\vec{s}_c; l, \frac{\pi}{2}) R D_h^{ew}(\vec{s}'_c; l, 0) \\ D_h^{ew}(\vec{s}_c; l, 0) R D_s^{ew}(\vec{s}'_c; l, \frac{\pi}{2}) & D_h^{ew}(\vec{s}_c; l, 0) R D_h^{ew}(\vec{s}'_c; l, 0) \end{array} \right\} \\ & \cdot \left\{ \begin{array}{c} E_{\beta'}^i(Q^{c_1}) \\ E_{\phi'}^i(Q^{c_1}) \end{array} \right\} \frac{\exp[-jk(l + s_c)]}{s_c}. \end{aligned} \quad (4.5)$$

Explicitly,

$$\begin{aligned} \left\{ \begin{array}{c} E_{\beta}^{c_1 c_2} \\ E_{\phi}^{c_1 c_2} \end{array} \right\} = & \frac{-\exp(j\pi/4) \exp(-jk(l + s_c))}{(2\pi k)^{3/2} s_c \sqrt{l}} \\ & \cdot \frac{\cos^2(\beta/2) F[2kl \sin^2(\beta/2)] \cos^2(\beta'/2) F[2kl \sin^2(\beta'/2)]}{\sin(\beta/2) \sin(\beta'/2)} \\ & \cdot \left\{ \begin{array}{cc} \sin(\phi/2) \sin(\phi'/2) & \sqrt{2} \sin(\phi/2) \cos(\phi'/2) \\ \sqrt{2} \cos(\phi/2) \sin(\phi'/2) & 2 \cos(\phi/2) \cos(\phi'/2) \end{array} \right\} \left\{ \begin{array}{c} E_{\beta'}^i(Q^{c_1}) \\ E_{\phi'}^i(Q^{c_1}) \end{array} \right\}. \end{aligned} \quad (4.6)$$

### 4.3 Edge wave interactions at a polyhedral structure

Assuming that the point  $Q^{c_1}$  is the tip of a semi-infinite wedge, which is justifiable as long as diffraction is a local phenomenon (i.e., when the length of the edge is sufficiently large in terms of the wavelength), the field excited by this corner and propagating along edge (1) can be obtained via reciprocity from eq. (3.27) along with eqs. (3.17) and (3.28). Hence, considering a point electric source with moment  $\vec{p}^2$  located at the close neighborhood of  $Q^{c_2}$ , then it has been shown that the edge wave this dipole excites is diffracted by the tip  $Q^{c_1}$  and is evaluated at  $S$  according to

$$\vec{E}^{c_2, ew} = Z_0 \exp[j(\nu + 1)\pi/2] \Gamma(\nu) C(\nu)$$

$$\frac{p_r^e \sin(\phi_e/2) + p_\phi^e \cos(\phi_e/2)}{\rho_e^{1-\nu}} \frac{\exp[-jk(s'_c + l)]}{4\pi s'_c l^\nu} \vec{G}^c(\vec{s}'_c; l; \alpha_{e1}, n_{e1}; \alpha_{f1}, n_{f1}), \quad (4.7)$$

where  $(\rho_e, \phi_e)$  are the cylindrical coordinates of the point source at the

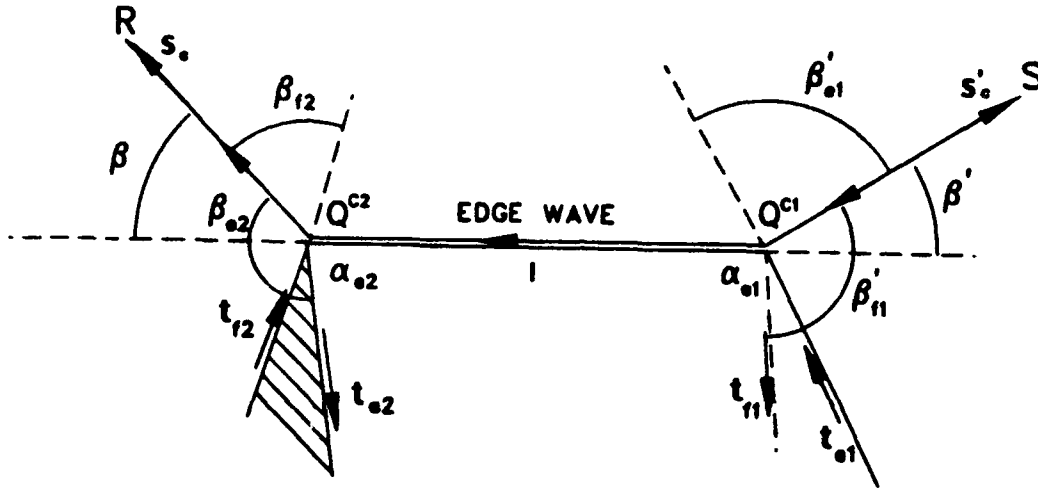


Figure 4.3: Edge wave diffraction for a polyhedral structure.

guiding edge associated coordinate system, while

$$\vec{G}(\vec{s}'_c; l; \alpha_{e1}, n_{e1}; \alpha_{f1}, n_{f1}) = F[2kL'_c \sin^2(\beta/2)] \left[ \frac{\sin^\nu \alpha_{e1} \vec{G}_{e1}^c(\vec{s}'_c) F_{-\nu}^c\{kL'_c[1 - \cos(\alpha_{e1} - \beta'_{e1})]\}}{(\cos \alpha_{e1} - \cos \beta'_{e1})^\nu} + \frac{\sin^\nu \alpha_{f1} \vec{G}_{f1}^c(\vec{s}'_c) F_{-\nu}^c\{kL'_c[1 + \cos(\alpha_{f1} + \beta'_{f1})]\}}{(\cos \alpha_{f1} + \cos \beta'_{f1})^\nu} \right] \quad (4.8)$$

and

$$\vec{G}_{e1, f1}^c(\vec{s}'_c) = -\cot(\beta'/2) \hat{\beta}' + \vec{G}_{e1, f1}^{c, f}(\vec{s}'_c) \quad (4.9)$$

with  $\vec{G}_{e1, f1}^{c, f}$  defined by eq. (3.29), adapted to the coordinate systems related to edges (e1) and (f1). It is reminded that  $\nu = 1/n$ , with  $n$  denoting the

guiding wedge number. Further,  $n_{e1, f1}$  and, later,  $n_{f2, e2}$  are used to denote the wedge number associated with the adjacent edges (e1), (f1) and (e2), (f2), respectively. The parameter  $L'_e$  is defined by eq. (4.3). It should be finally noted that the angles  $\beta'_{e1, f1}$  are the elevation angle of  $S$  in edges (e1) and (f1) fixed coordinate systems as shown in Fig. 4.3.

Considering a dipole source with moment  $\vec{p}^s = p_{\beta}^s \hat{\beta}' + p_{\phi}^s \hat{\phi}'$  located at  $S$  and applying the reciprocity theorem the corner excited edge wave at the location of the point source  $\vec{p}^s$  equals

$$\begin{aligned} \vec{E}^{ew} &= Z_0 \exp[j(\nu + 1)\pi/2] \Gamma(\nu) C(\nu) \frac{\hat{\rho}_e \sin(\phi_e/2) + \hat{\phi}_e \cos(\phi_e/2)}{\rho_e^{1-\nu}} \\ &\quad \cdot \frac{\exp[-jk(s'_c + l)]}{4\pi s'_c l^\nu} \vec{G}^c(\vec{s}'_c; l; \alpha_{e1}, n_{e1}; \alpha_{f1}, n_{f1}) \cdot \vec{p}^s \\ &= \frac{-\exp(j\nu\pi/2) \Gamma(\nu) C(\nu)}{k} \frac{\hat{\rho}_e \sin(\nu\phi_e) + \hat{\phi}_e \cos(\nu\phi_e)}{\rho_e^{1-\nu}} \\ &\quad \cdot \frac{\exp(-jkl)}{l^\nu} \vec{G}^c(\vec{s}'_c; l; \alpha_{e1}, n_{e1}; \alpha_{f1}, n_{f1}) \cdot \vec{E}^i(Q^{c1}). \end{aligned} \quad (4.10)$$

It is reminded that the paraxial edge wave excited by a point source radiating in the vicinity of the edge of a half plane and evaluated at the point  $(\rho_e, \phi_e, l)$  with  $kl \gg 1$  can be approximated by

$$\vec{E}^{ew} = jZ_0 k^\nu C(\nu) A^{eq} \frac{\hat{\rho}_e \sin(\nu\phi_e) + \hat{\phi}_e \cos(\nu\phi_e)}{\rho_e^{1-\nu}} \frac{\exp(-jkl)}{l^\nu}, \quad (4.11)$$

where  $A^{eq}$  is a source related factor in view of eq. (3.5). Upon comparison of eqs. (4.10) and (4.11) one readily obtains

$$\begin{aligned} A^{eq} &= A^{eq}(\vec{s}'_c; l; \alpha_{e1}, n_{e1}; \alpha_{f1}, n_{f1}) \\ &= \frac{jY_0 \exp(j\nu\pi/2) \Gamma(\nu)}{k^{\nu+1}} \vec{G}^c(\vec{s}'_c; l; \alpha_{e1}, n_{e1}; \alpha_{f1}, n_{f1}) \cdot \vec{E}^i(Q^{c1}), \end{aligned} \quad (4.12)$$

thus, defining a fictitious equivalent point source located at the tip  $Q^{c1}$  and exciting the edge wave given by eq. (4.10). One then considers the diffraction of the edge wave produced by the equivalent point source at the corner  $Q^{c2}$ . Referring to eq. (3.21) one writes

$$\vec{E}^{c1c2} = Z_0 \exp[j(\nu + 1)\pi/2] \Gamma(\nu) C(\nu) A^{eq}$$

$$\frac{\exp[-jk(s'_c + l)]}{4\pi s_c l^\nu} \vec{G}^c(\vec{s}_c; l; \alpha_{e2}, n_{e2}; \alpha_{f2}, n_{f2}), \quad (4.13)$$

Upon incorporation of eq. (4.12) into the above relation one derives the the following expression for the edge wave diffracted field:

$$\vec{E}^{c_1 c_2} = \overline{\overline{D}}^c(\vec{s}'_c, \vec{s}_c; l, \alpha_1, \alpha_2) \cdot \vec{E}^i(Q^{c_1}) \frac{\exp\{-jk(l + s_c)\}}{s_c \sqrt{l}}, \quad (4.14)$$

where the dyadic diffraction coefficient is given by

$$\begin{aligned} \overline{\overline{D}}^c(\vec{s}'_c, \vec{s}_c; l, \alpha_1, \alpha_2) &= -\frac{\exp(j\nu\pi)[\Gamma(\nu)]^2 C(\nu)}{4\pi k(kl)^\nu} \\ &\vec{G}^c(\vec{s}_c; l; \alpha_{e2}, n_{e2}; \alpha_{f2}, n_{f2}) \vec{G}^c(\vec{s}'_c; l; \alpha_{e1}, n_{e1}; \alpha_{f1}, n_{f1}). \end{aligned} \quad (4.15)$$

In the case of a flat plate we have

$$\begin{aligned} \vec{G}^c(\vec{s}_c; l; \alpha_{e2}, n_{e2}; \alpha_{f2}, n_{f2}) &= 2\vec{G}_0^c(\vec{s}_c; l, \alpha_2) \\ &= 2[-\cot(\beta/2)\hat{\beta} + \vec{G}^{c,f}(\vec{s}_c)], \\ \vec{G}^c(\vec{s}'_c; l; \alpha_{e1}, n_{e1}; \alpha_{f1}, n_{f1}) &= 2\vec{G}_0^c(\vec{s}'_c; l, \alpha_1) \\ &= 2[-\cot(\beta'/2)\hat{\beta}' + \vec{G}^{c,f}(\vec{s}'_c)], \end{aligned}$$

where  $\vec{G}^{c,f}$  is defined by eq. (3.31)-(3.34), and

$$C(\nu) = C(1/2) = \frac{j \exp(j\pi/4)}{2\pi\sqrt{2\pi}}.$$

Hence, eq. (4.15) becomes

$$\overline{\overline{D}}^c(\vec{s}'_c, \vec{s}_c; l, \alpha_1, \alpha_2) = \frac{\exp(j\pi/4)}{(2\pi k)^{3/2}} \vec{G}^c(\vec{s}_c; l, \alpha_2) \vec{G}^c(\vec{s}'_c; l, \alpha_1). \quad (4.16)$$

The above can be further simplified in the case of two adjacent right angled vertices. In particular, the corner-to-corner edge wave interaction becomes

$$\begin{aligned} E_{\beta}^{c_1 c_2} &= \frac{\exp(j\pi/4)}{(2\pi k)^{3/2}} E_{\beta'}^i(Q^{c_1}) \frac{\exp(-jk(l + s_c))}{\sqrt{l s_c}} \\ &\frac{F[2kl \sin^2(\beta/2)]}{\sin(\beta/2)} \frac{F_{-1/2}^c[2kl(1 - \sqrt{1 - \sin^2 \beta \cos^2 \phi})]}{\sqrt{\sin \beta \cos \phi}} \\ &\frac{F[2kl \sin^2(\beta'/2)]}{\sin(\beta'/2)} \frac{F_{-1/2}^c[2kl(1 - \sqrt{1 - \sin^2 \beta' \cos^2 \phi'})]}{\sqrt{\sin \beta' \cos \phi'}}. \end{aligned} \quad (4.17)$$

Note that eq. (4.17) predicts a dominant  $\hat{\beta}$  directed field which is physically justifiable, since the edge wave currents are accumulated in the vicinity of the guiding edge. The same is not true with the corrected Sikta's expression (4.6). The two equations indicate also a different azimuth dependence and a different elevation angle variation approximately by a factor of  $\sqrt{\csc\beta' \csc\beta}$ . As a matter of fact, eq. (4.17) is expected to predict a stronger field when edge on incidence is approached. Further, the transitional behavior of the two expressions is different.

It should be reminded that the corner diffracted edge wave is discontinuous at the shadow boundary of the edge diffracted edge wave in such a manner that the total field remains continuous. In the same context, in addition to the tip-to-tip edge wave diffraction demonstrated above, tip-to-edge and, vice versa, edge-to-tip diffracted ray contributions may occur at certain aspects of incidence and observation. The discontinuity of these rays when the tip and the edge diffraction point coalesce should be normally compensated by an analogous discontinuous behavior of double corner diffracted edge wave. The analysis pertinent to this type of rays is similar and it is not repeated here. It simply involves the multiplication of the edge wave in eq. (4.11), excited by the equivalent point source by the proper edge wave edge diffraction coefficient in view of the development in Section 3.5.

#### 4.4 Discussion and numerical results

The diffraction by two adjacent corners of a polyhedral structure has been studied as a second order additive correction to the corner diffracted fields in a high frequency presentation of the scattering by conducting edged bodies. A double corner-to-corner edge wave dyadic coefficient was deduced, which can be used as a first engineering approximation in higher order UTD computations. It involves the multiplication of two transition factors expressed in terms of the parabolic cylinder function of order  $-\nu$  and the ordinary Fresnel integral, that appear in the first order theory, in an analogous manner that the double edge diffraction is described via ordinary UTD calculations. Outside its transition domains (i.e., when the source or the observer are lined up with the edge), the edge wave diffraction coefficient is proportional to  $k^{-3/2}$ , while it decays with the inverse distance from the tip along the edge. Therefore, it represents one of the next higher order

mechanisms in a high frequency depiction of the fields, in addition to the corner diffracted rays.

The effect of the introduction of edge waves as a higher order mechanism has been evaluated via RCS computations of flat plates. The corner diffraction is represented as the truncation effect of the Physical Optics and non-uniform component of the currents on the plate. Two flat plate examples, where the edge wave contribution have been expected to be of particular importance have been investigated: (i) the off principal plane RCS of a  $2\lambda$  square plate and (ii) Sikta's triangle. Specifically, Figs. 4.6-4.9 demonstrate the effect of the superposition of edge wave mechanisms in the echo of a  $2\lambda$  square plate. For comparison, the corner diffraction solution [2] is also shown.

Sikta's triangle (Fig. 4.4 and 4.5) is another case where edge waves become important, especially, at nose-on incidence. Indeed, incorporation of the edge wave mechanisms appears to improve the calculated RCS at regions where they are expected to be significant. It should be emphasized that corner-to-edge (and vice versa) edge wave mechanisms which may be important in certain aspects of observation have not incorporated in the calculations. Therefore, a discontinuity may appear at observation directions corresponding to the shadow boundaries of the corner-to-edge diffracted rays. Further research should investigate these mechanisms and their transitional behavior as well as their relation with the rays arising from the asymptotic integration of the non-uniform components of the currents studied in Chapter 5.

In general, due to the non-availability of a rigorously derived corner diffraction coefficient, one is difficult to assess the contribution of higher order mechanisms from RCS pattern studies. Therefore, time-domain mechanism extraction has been investigated [37] in the identification and quantitative analysis of the doubly diffracted ray contributions that constitute the echo of a large edged body. It has thus been observed that the edge waves, at least outside the transition regions where more than one mechanisms coalesce, are adequately predicted with the present solution. In transitions regions, e.g. at edge on incidence or at the shadow boundaries of corner-to-edge and edge-to-corner diffracted rays a more careful investigation is required. Fig. 4.10 depicts the measured and calculated impulse response of a diamond shape plate. Further investigation of the edge wave mechanisms has been focused in the evaluation of the several mechanisms

appearing in the impulse response of a 24" square plate for several aspects of illumination, which are illustrated in Figs. 4.11-4.25. The corner diffracted rays are denoted by C1-C4, while possible edge wave mechanisms are indicated by E1-E4 and double diffractions with D1-D4. The support structure returns are S1 and S2.

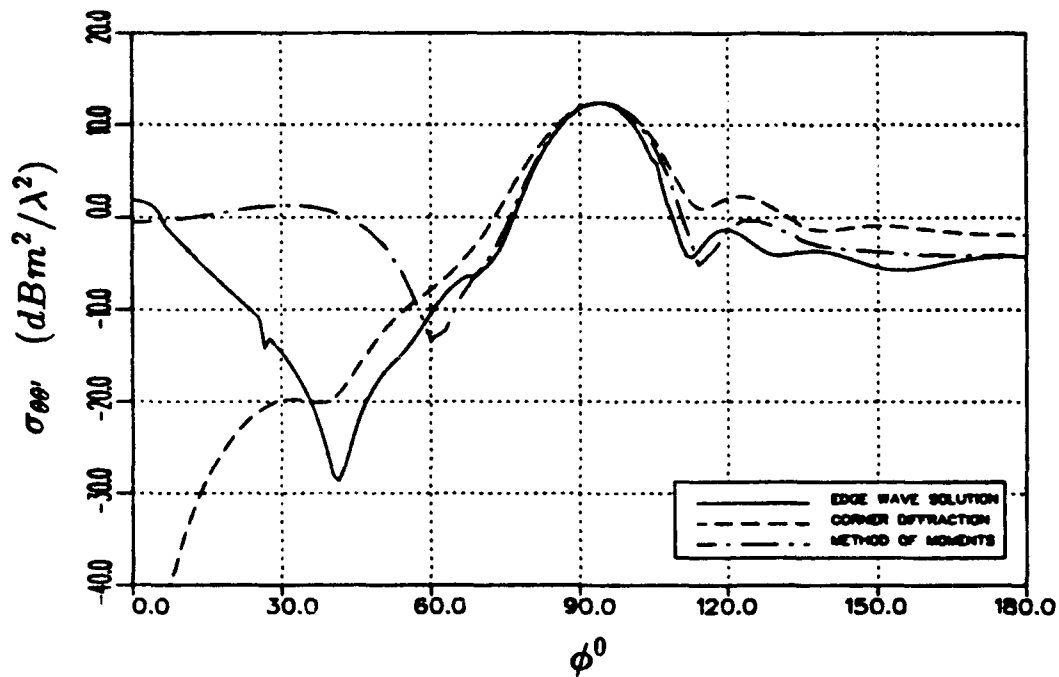


Figure 4.4:  $\sigma_{ee'}$  RCS of Sikta's triangle with  $a = 2\lambda$  and  $\alpha = 30^\circ$  at  $\theta = 90^\circ$ .

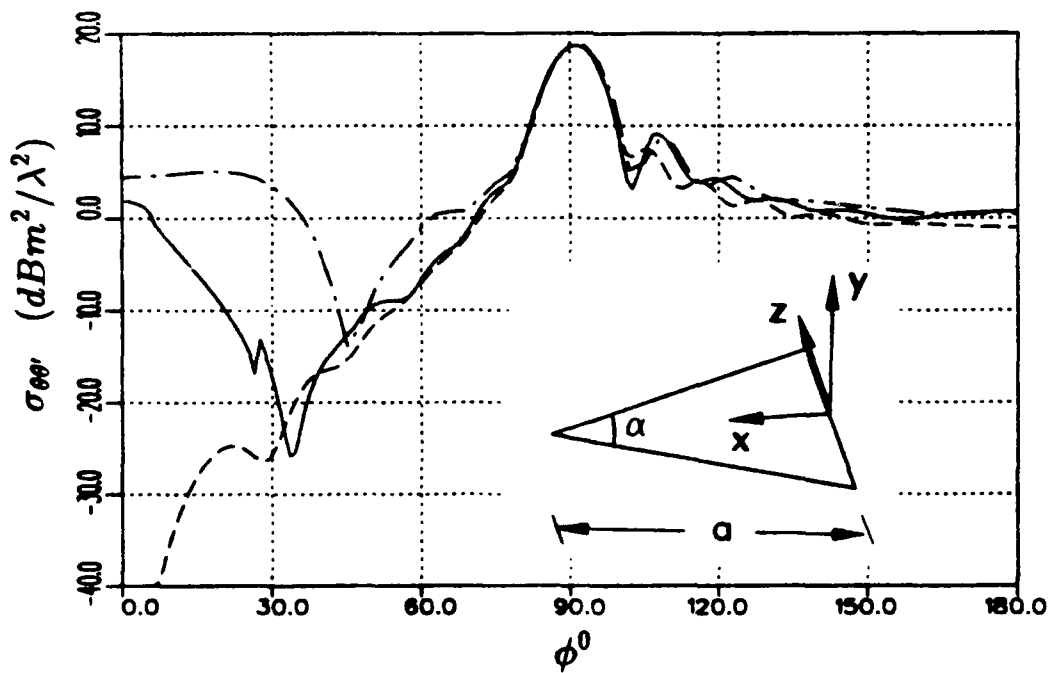


Figure 4.5:  $\sigma_{ee'}$  RCS of Sikta's triangle with  $a = 3\lambda$  and  $\alpha = 30^\circ$  at  $\theta = 90^\circ$ .

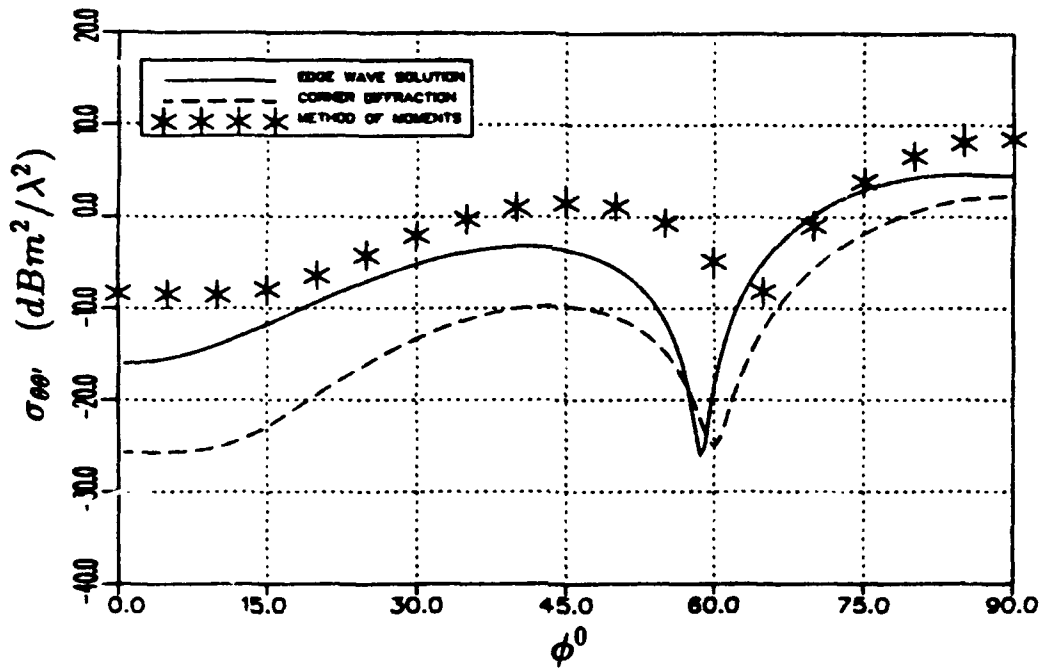


Figure 4.6:  $\sigma_{ee'}$  RCS of a  $2\lambda$  square plate at  $\theta = 30^\circ$ .

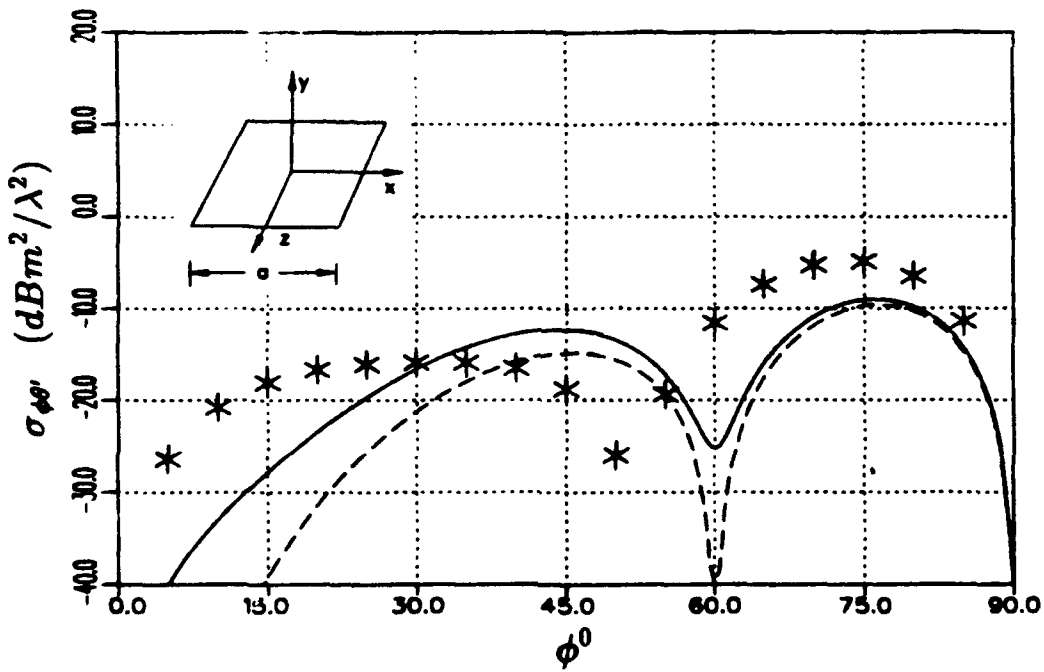


Figure 4.7:  $\sigma_{\phi\phi'}$  RCS of a  $2\lambda$  square plate at  $\theta = 30^\circ$ .

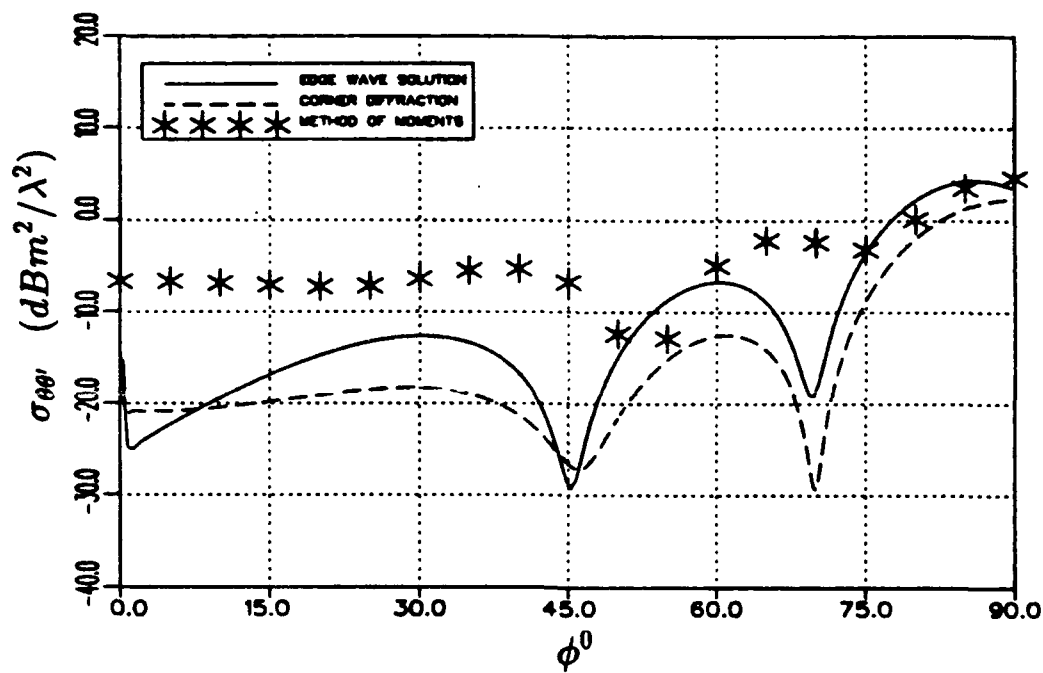


Figure 4.8:  $\sigma_{ee'}$  RCS of a  $2\lambda$  square plate at  $\theta = 45^\circ$ .

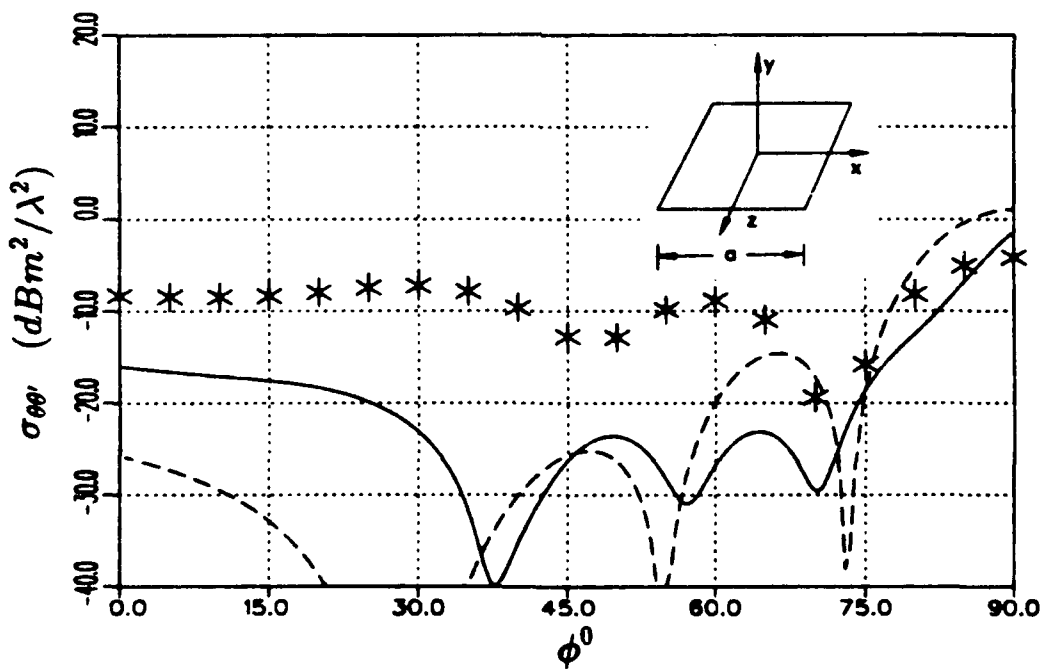
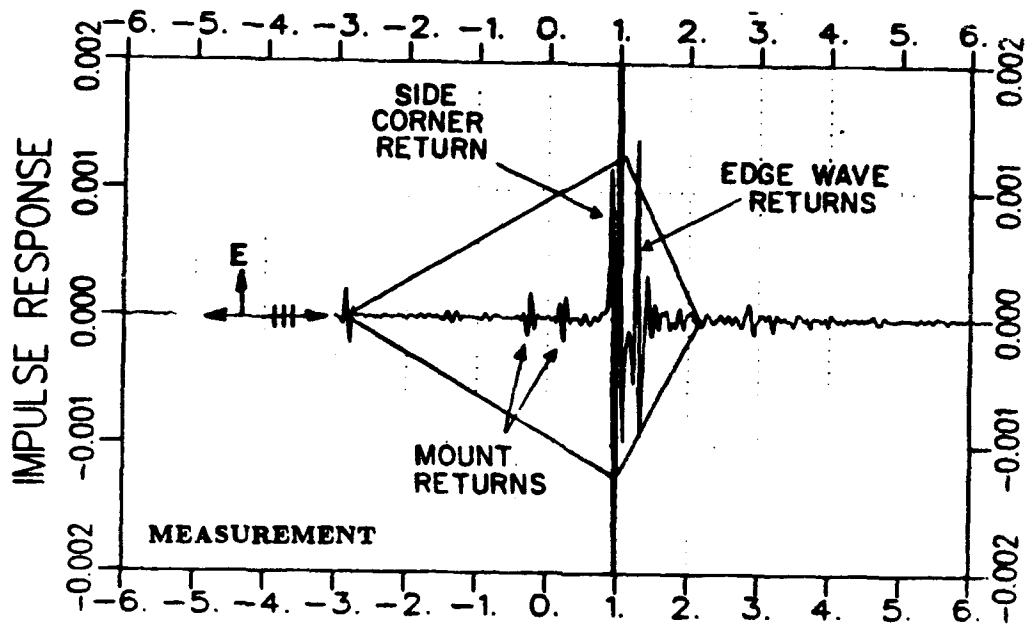
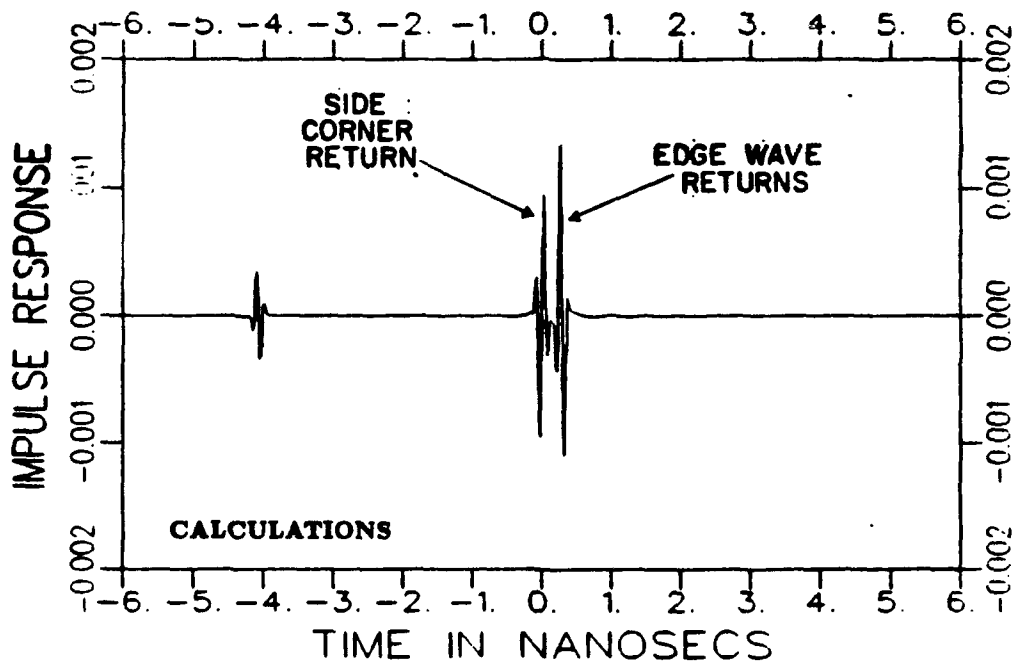


Figure 4.9:  $\sigma_{ee'}$  RCS of a  $2\lambda$  square plate at  $\theta = 60^\circ$ .



(a)



(b)

Figure 4.10: Impulse response of a diamond shape plate at nose-on: (a) measured, (b) calculated.

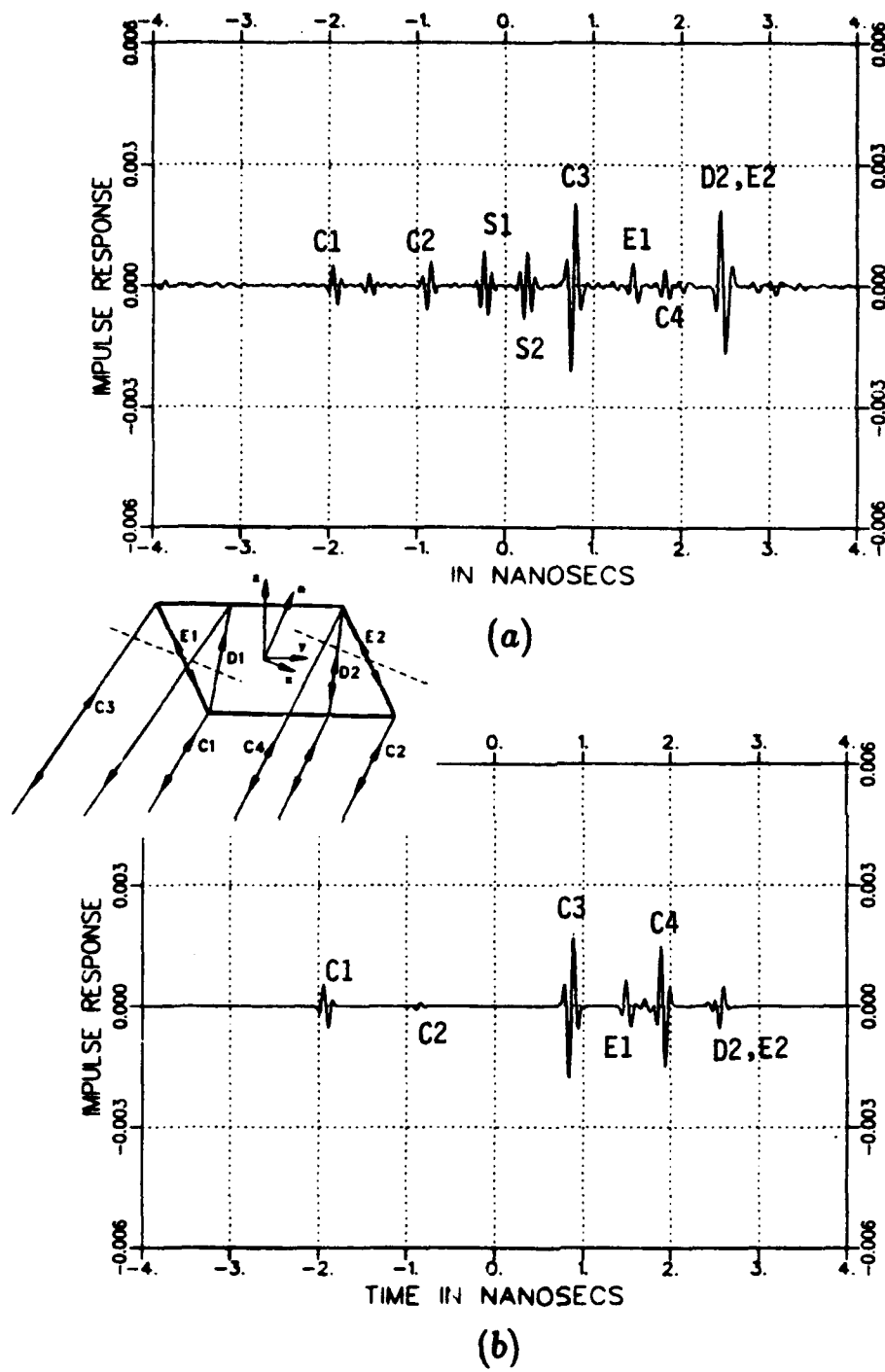


Figure 4.11: Impulse response of a 24" square plate at  $\phi = 45^\circ$  and  $\theta = 15^\circ$ . Vertical polarization. (a) Measured, (b) Calculated.

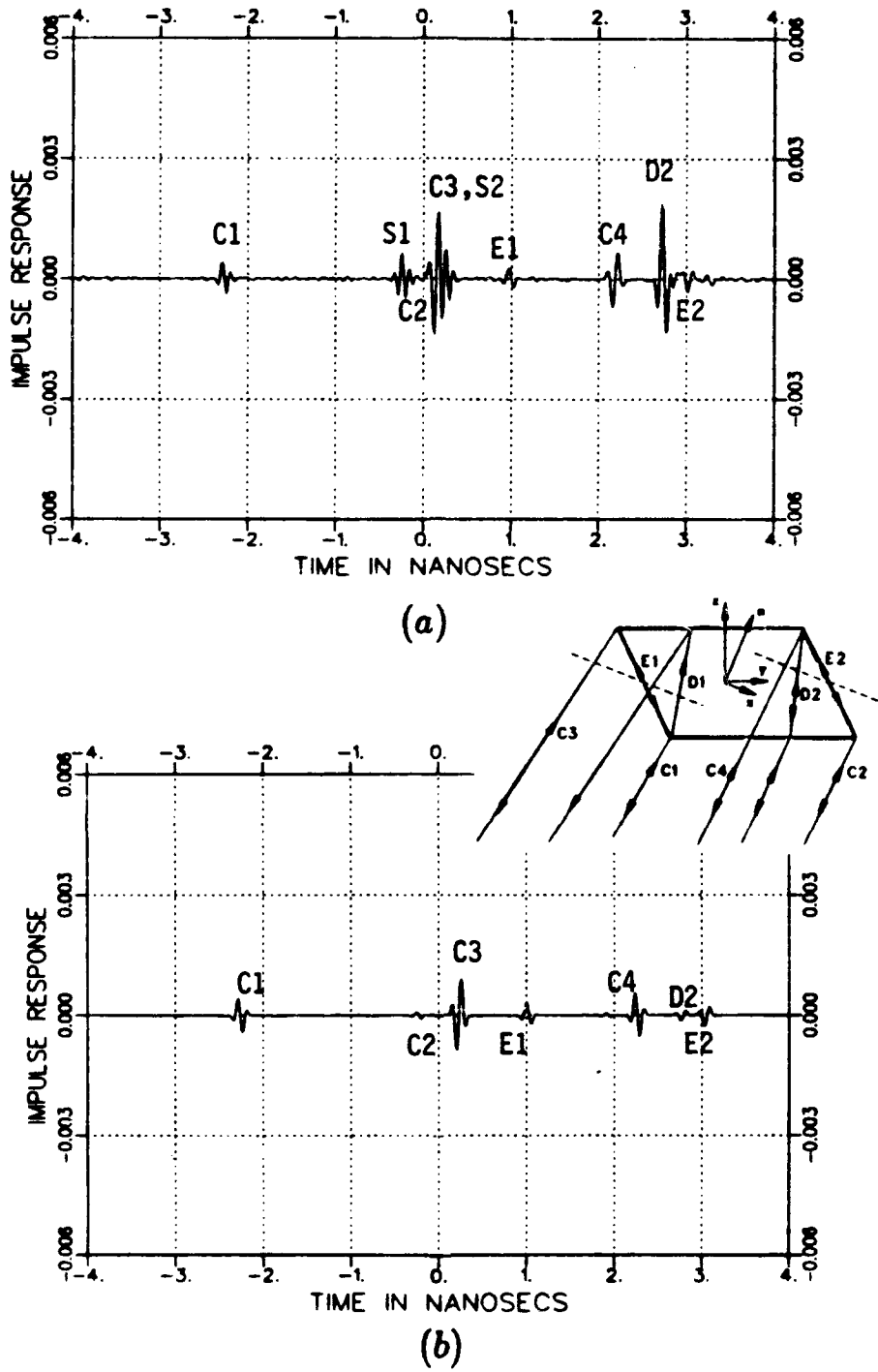


Figure 4.12: Impulse response of a 24" square plate at  $\phi = 45^\circ$  and  $\theta = 30^\circ$ . Vertical polarization. (a) Measured, (b) Calculated.

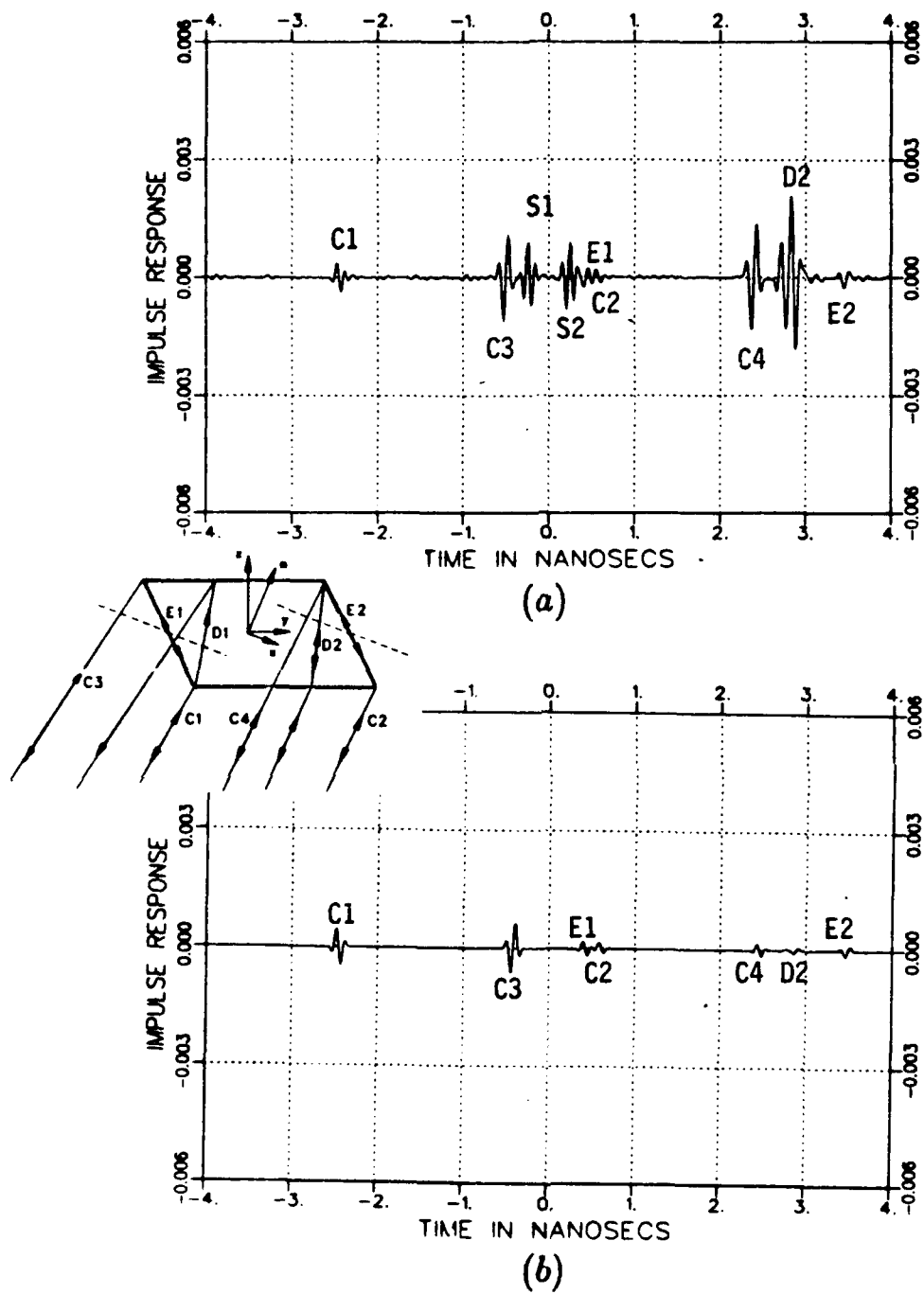


Figure 4.13: Impulse response of a 24" square plate at  $\phi = 45^\circ$  and  $\theta = 45^\circ$ . Vertical polarization. (a) Measured, (b) Calculated.

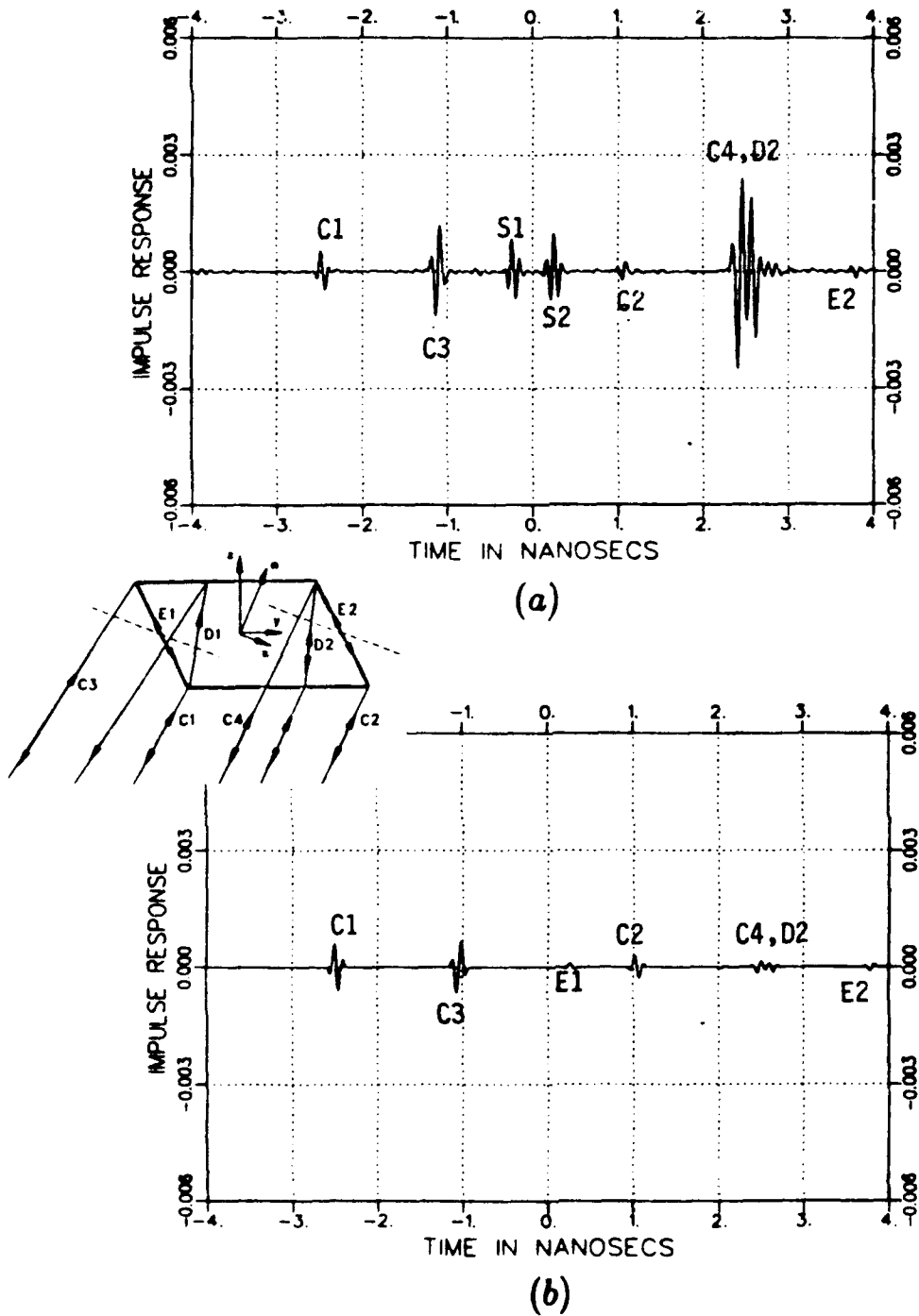


Figure 4.14: Impulse response of a 24" square plate at  $\phi = 45^\circ$  and  $\theta = 60^\circ$ . Vertical polarization. (a) Measured, (b) Calculated.

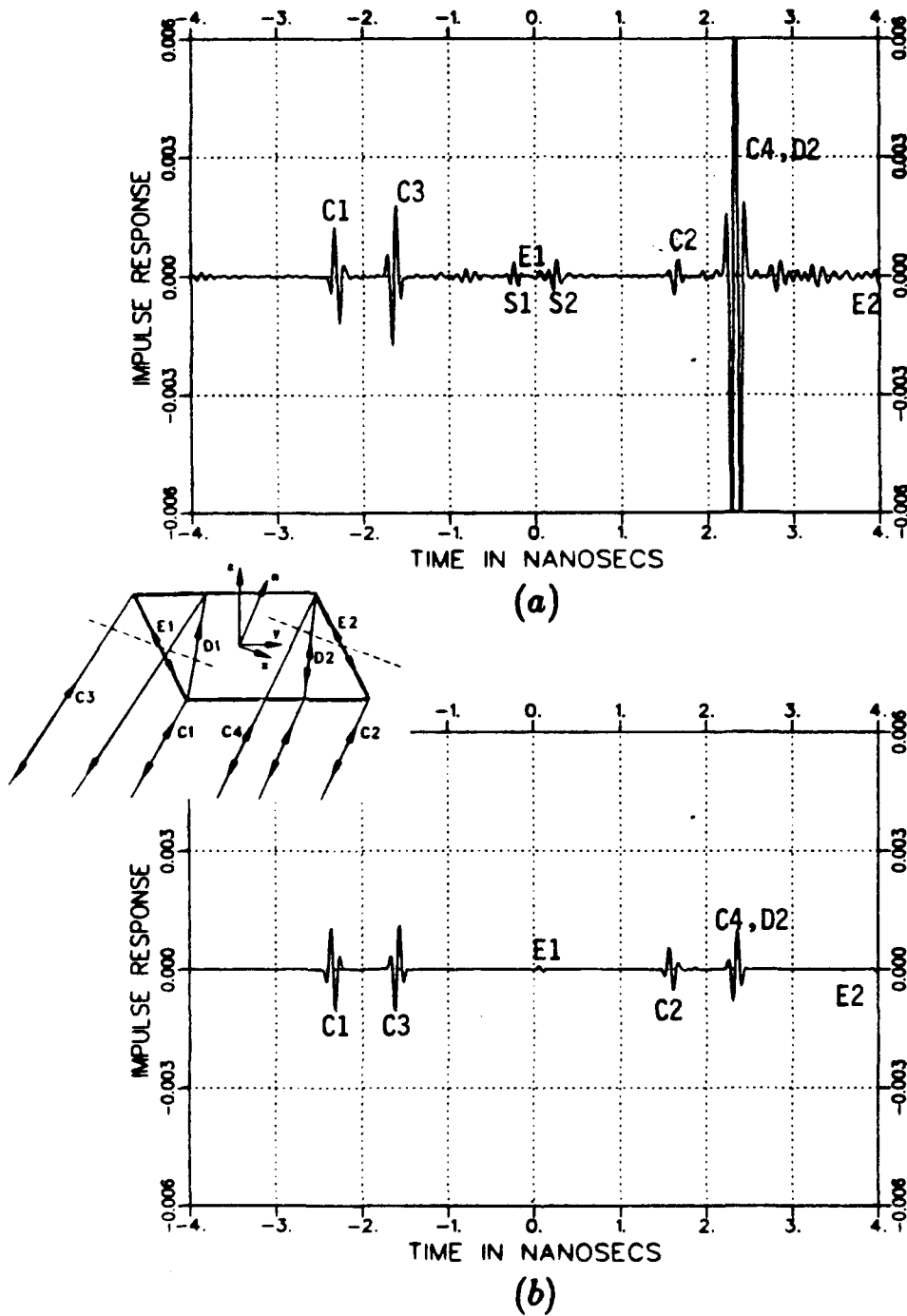


Figure 4.15: Impulse response of a 24" square plate at  $\phi = 45^\circ$  and  $\theta = 75^\circ$ . Vertical polarization. (a) Measured, (b) Calculated.

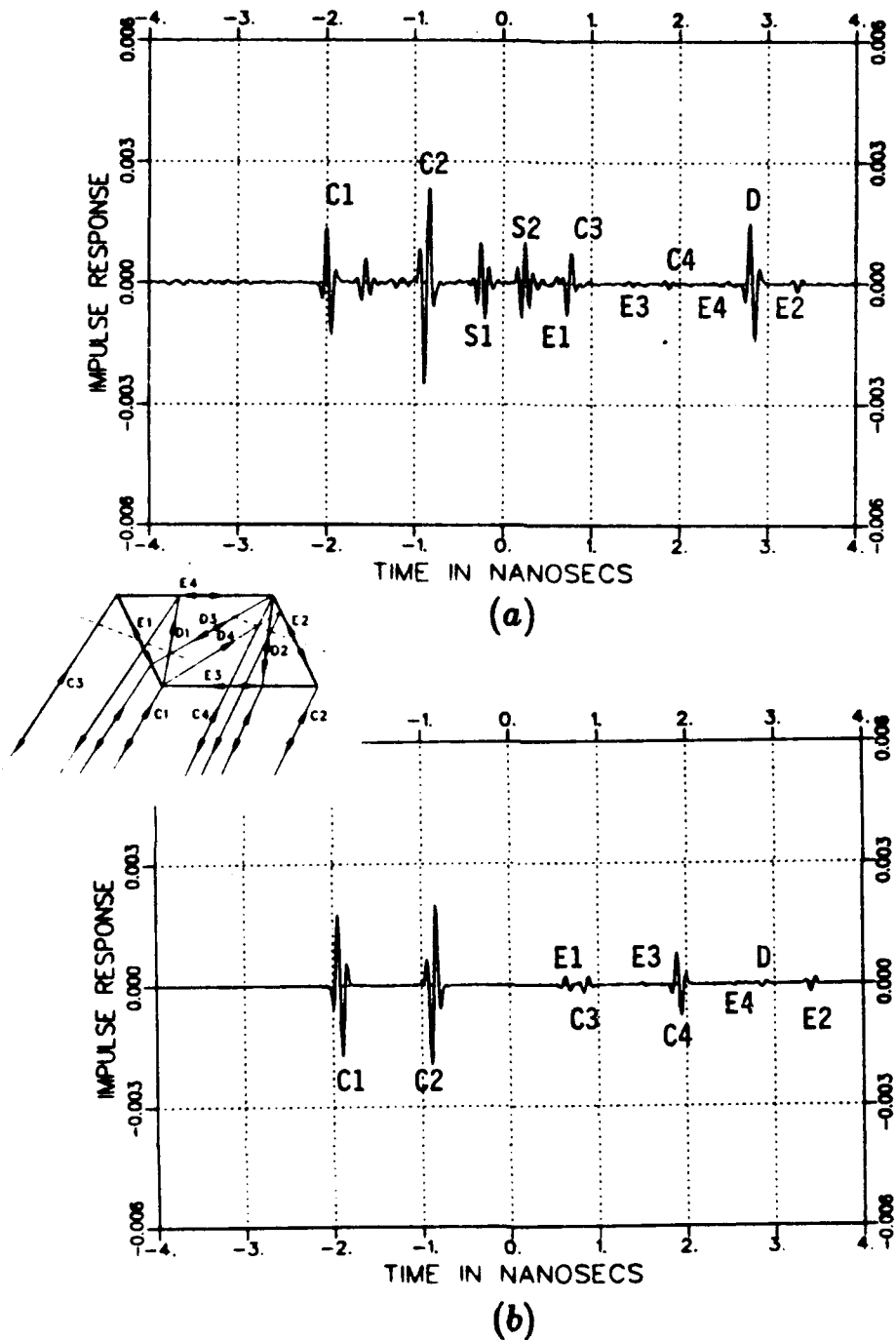


Figure 4.16: Impulse response of a 24" square plate at  $\phi = 45^\circ$  and  $\theta = 15^\circ$ . Horizontal polarization. (a) Measured, (b) Calculated.

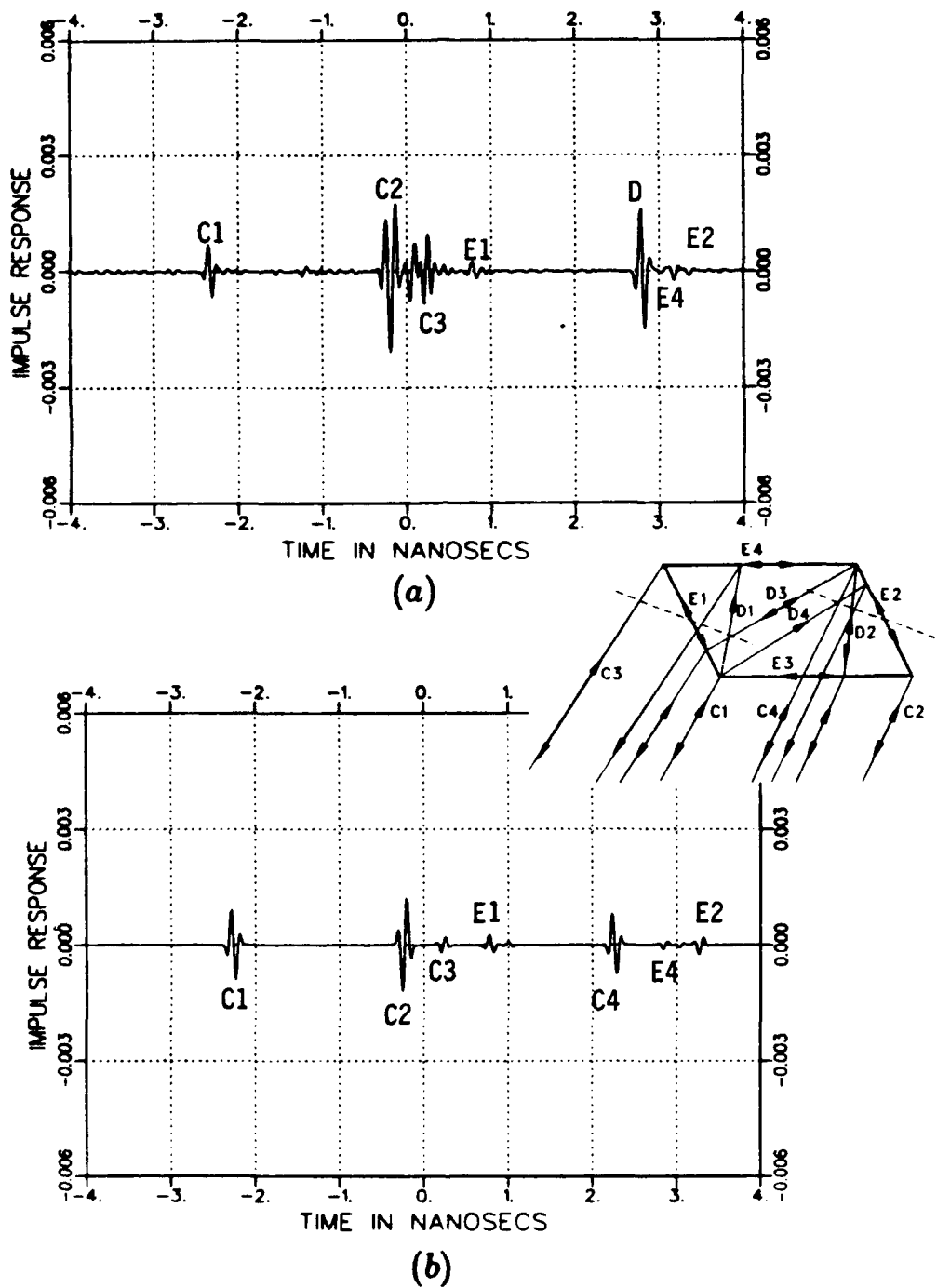


Figure 4.17: Impulse response of a 24" square plate at  $\phi = 45^\circ$  and  $\theta = 30^\circ$ . Horizontal polarization. (a) Measured, (b) Calculated.

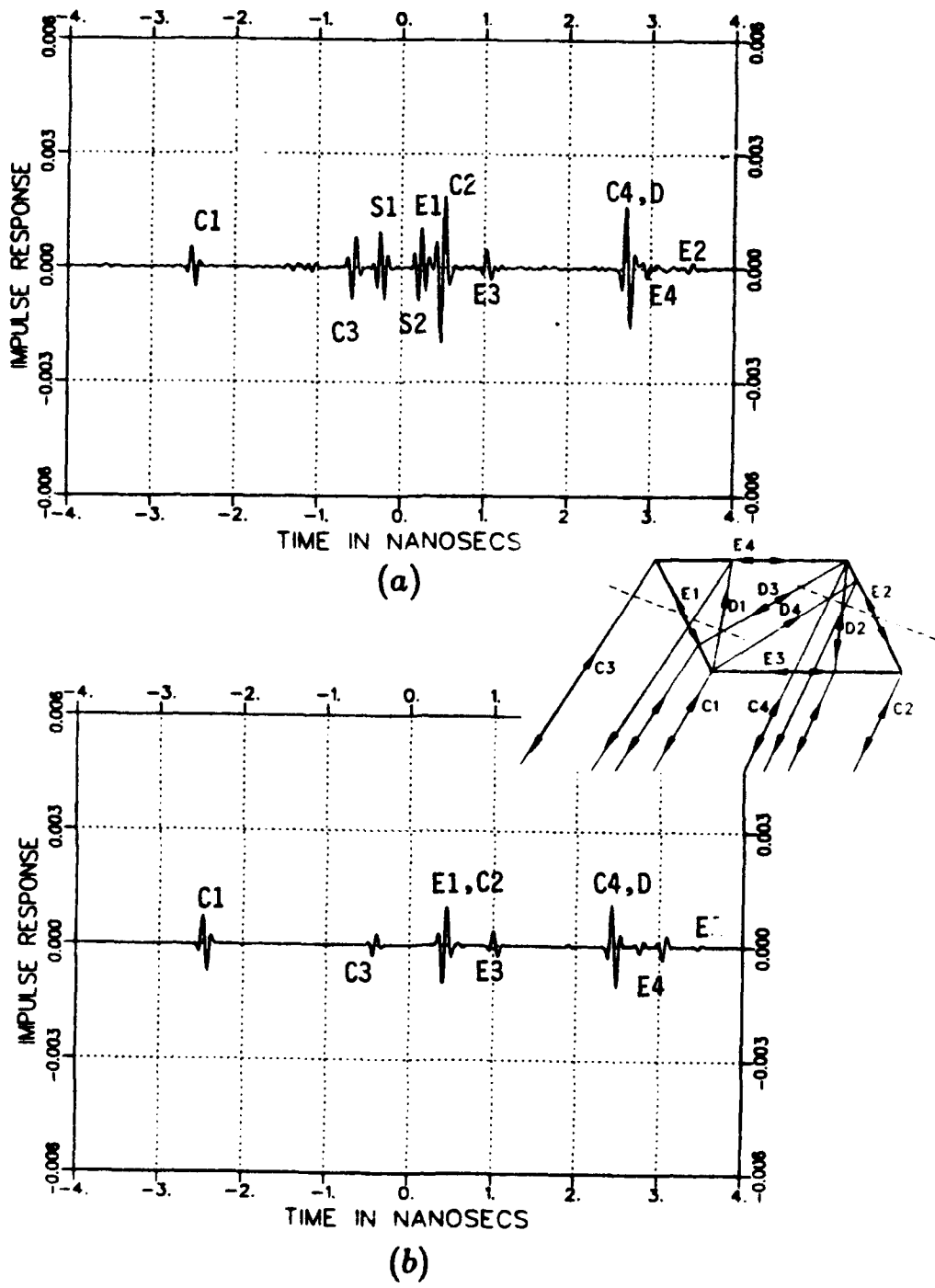


Figure 4.18: Impulse response of a 24" square plate at  $\phi = 45^\circ$  and  $\theta = 45^\circ$ . Horizontal polarization. (a) Measured, (b) Calculated.

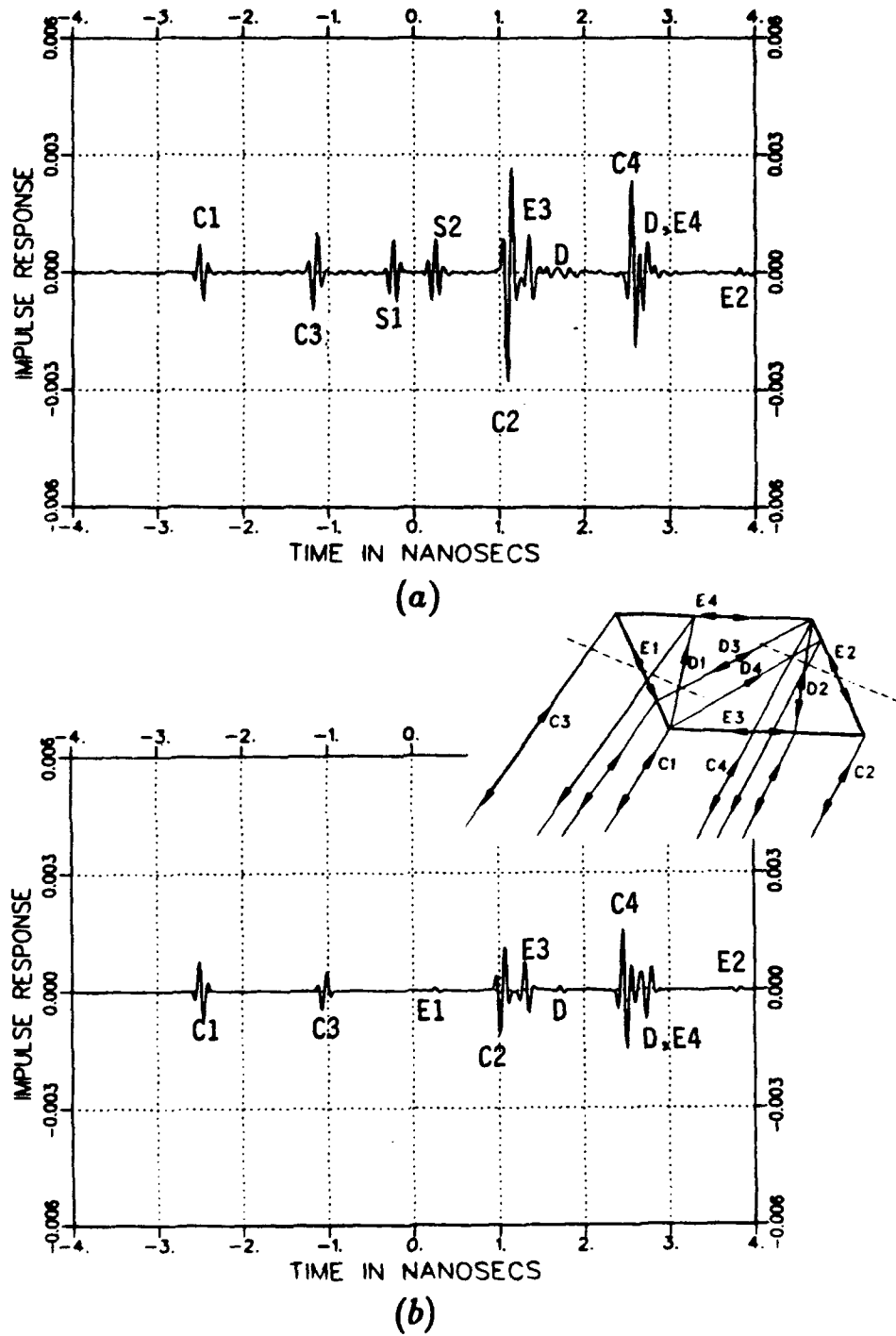


Figure 4.19: Impulse response of a 24" square plate at  $\phi = 45^\circ$  and  $\theta = 60^\circ$ . Horizontal polarization. (a) Measured, (b) Calculated.

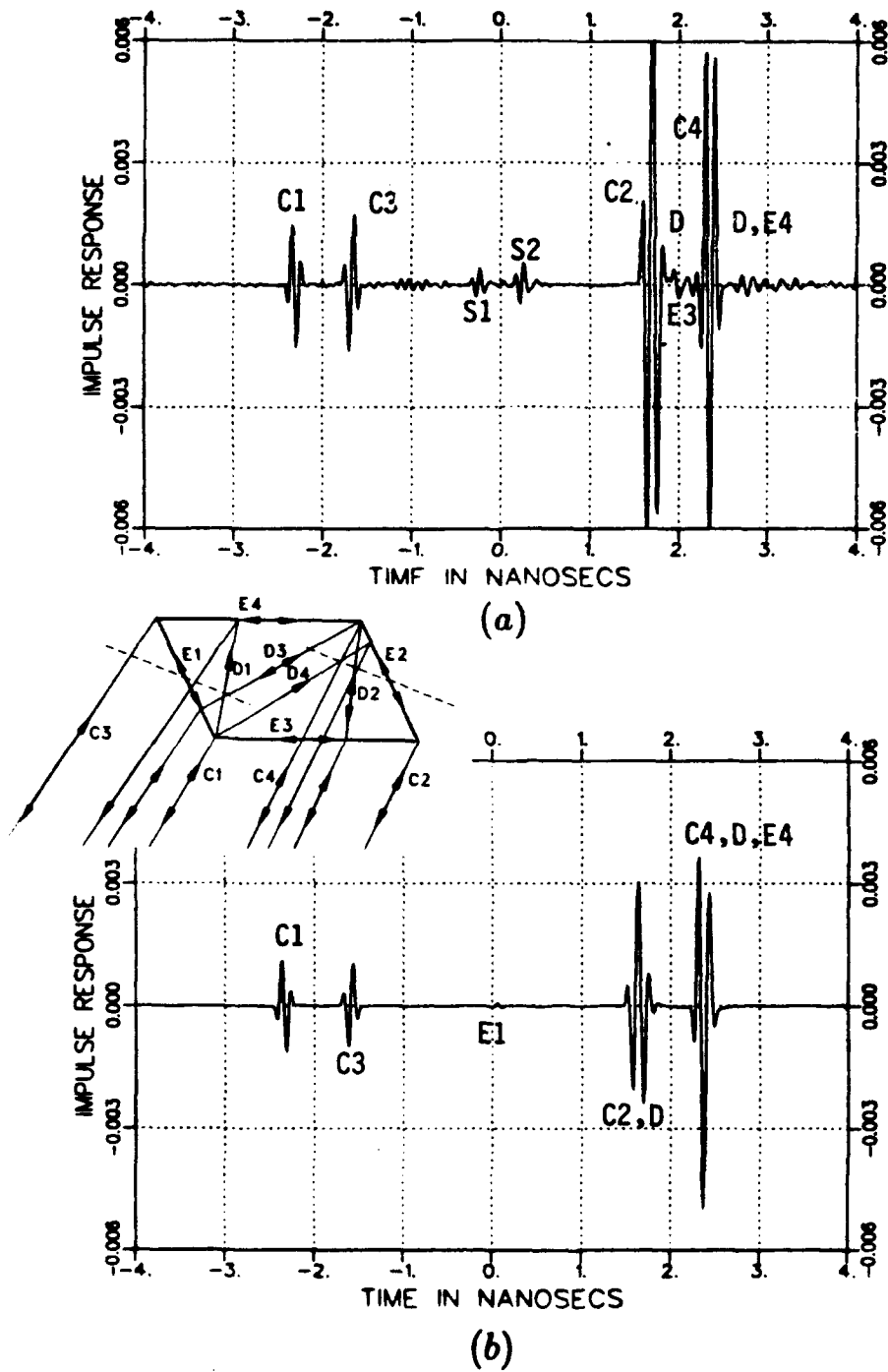


Figure 4.20: Impulse response of a 24" square plate at  $\phi = 45^\circ$  and  $\theta = 75^\circ$ . Horizontal polarization. (a) Measured, (b) Calculated.

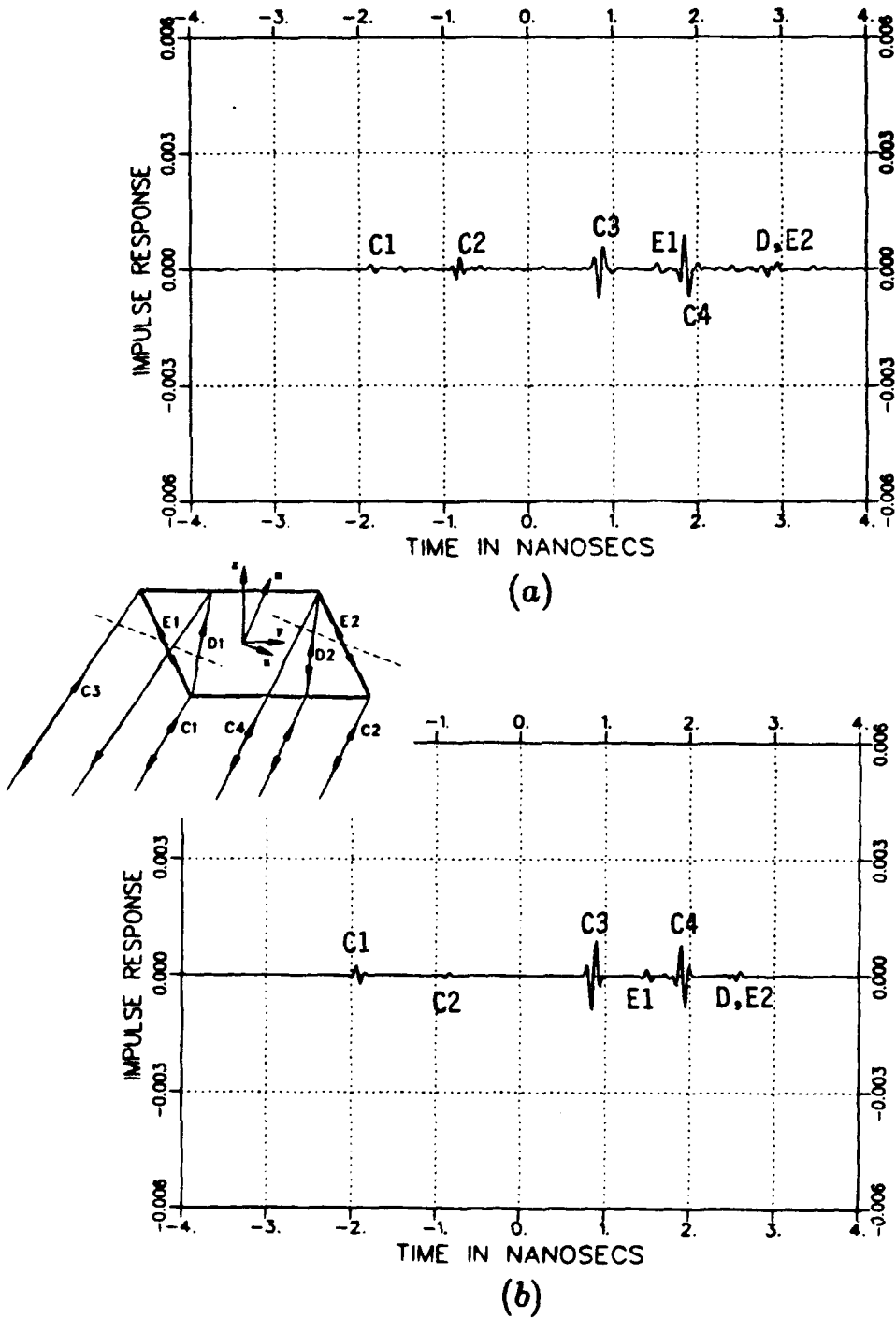


Figure 4.21: Impulse response of a 24" square plate at  $\phi = 45^\circ$  and  $\theta = 15^\circ$ . Cross polarization (a) Measured, (b) Calculated.

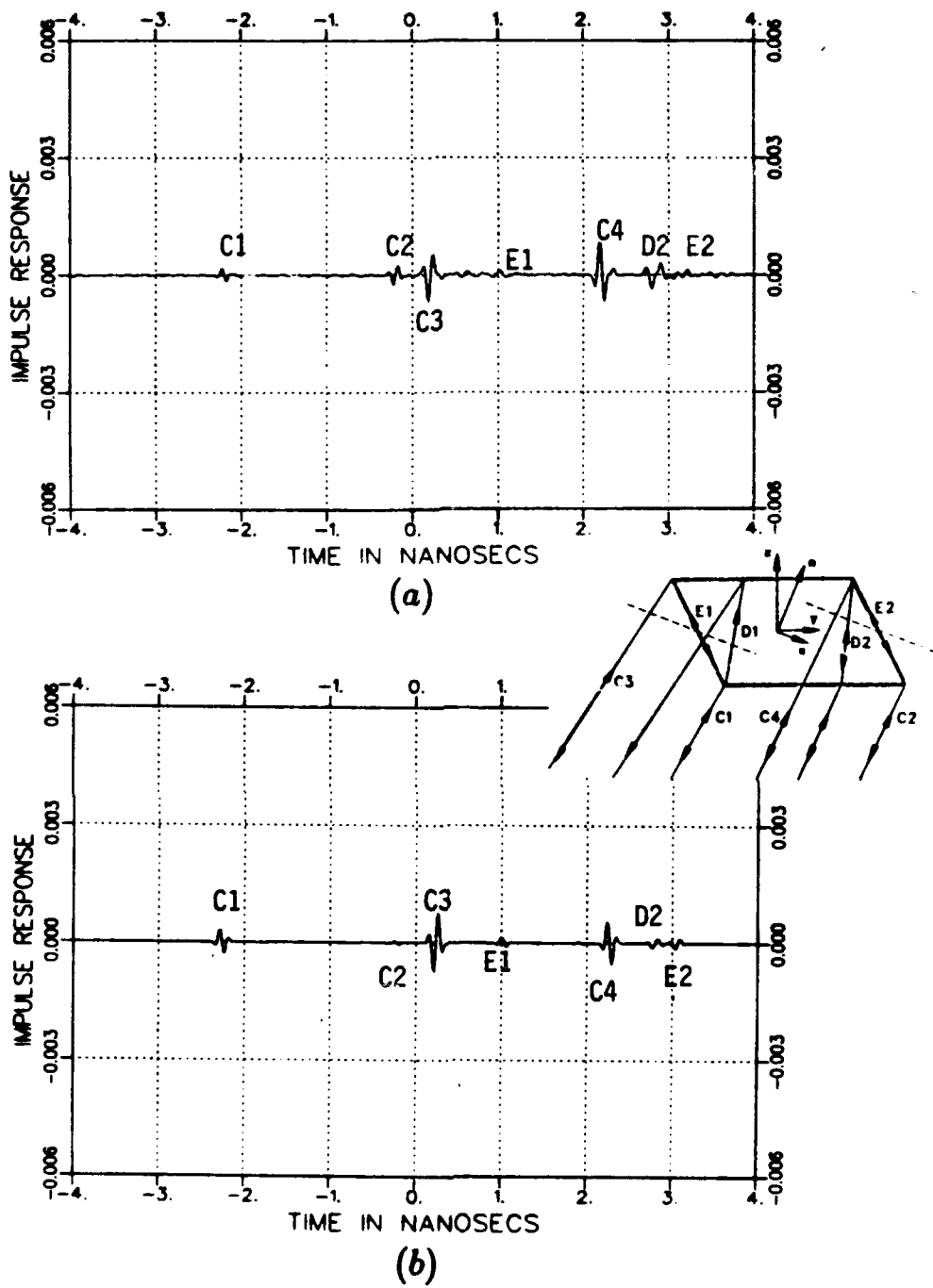
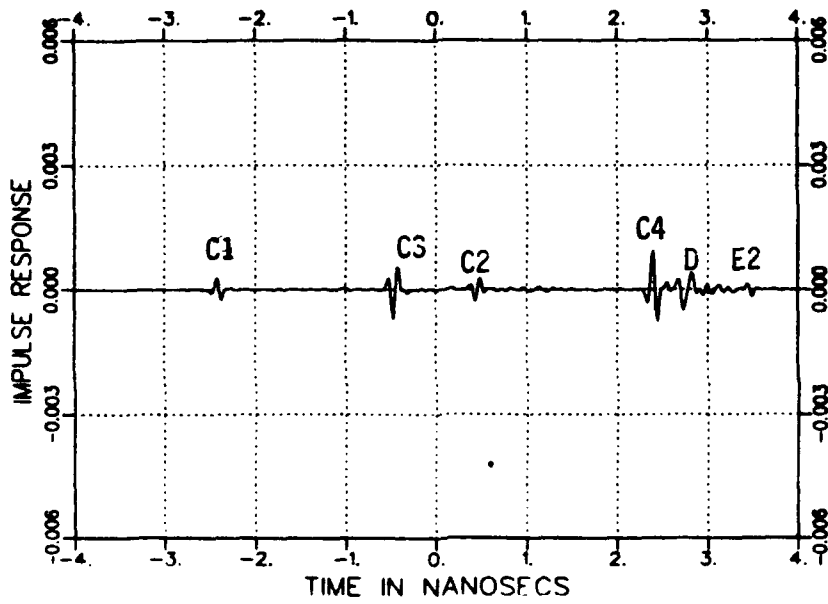
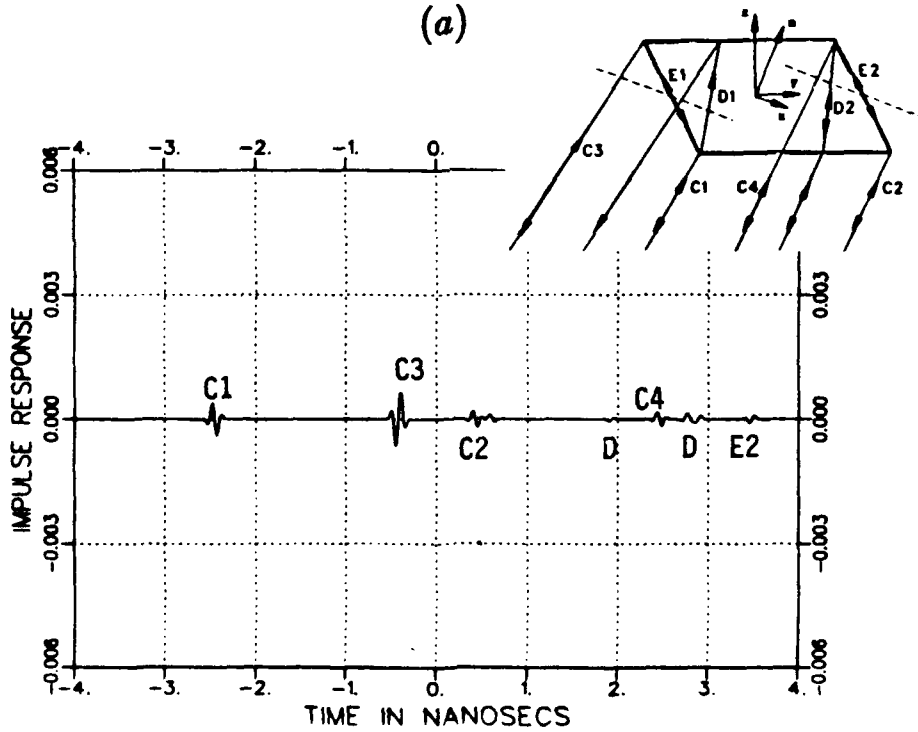


Figure 4.22: Impulse response of a 24" square plate at  $\phi = 45^\circ$  and  $\theta = 30^\circ$ . Cross polarization. (a) Measured, (b) Calculated.



(a)



(b)

Figure 4.23: Impulse response of a 24" square plate at  $\phi = 45^\circ$  and  $\theta = 45^\circ$ . Cross polarization. (a) Measured, (b) Calculated.

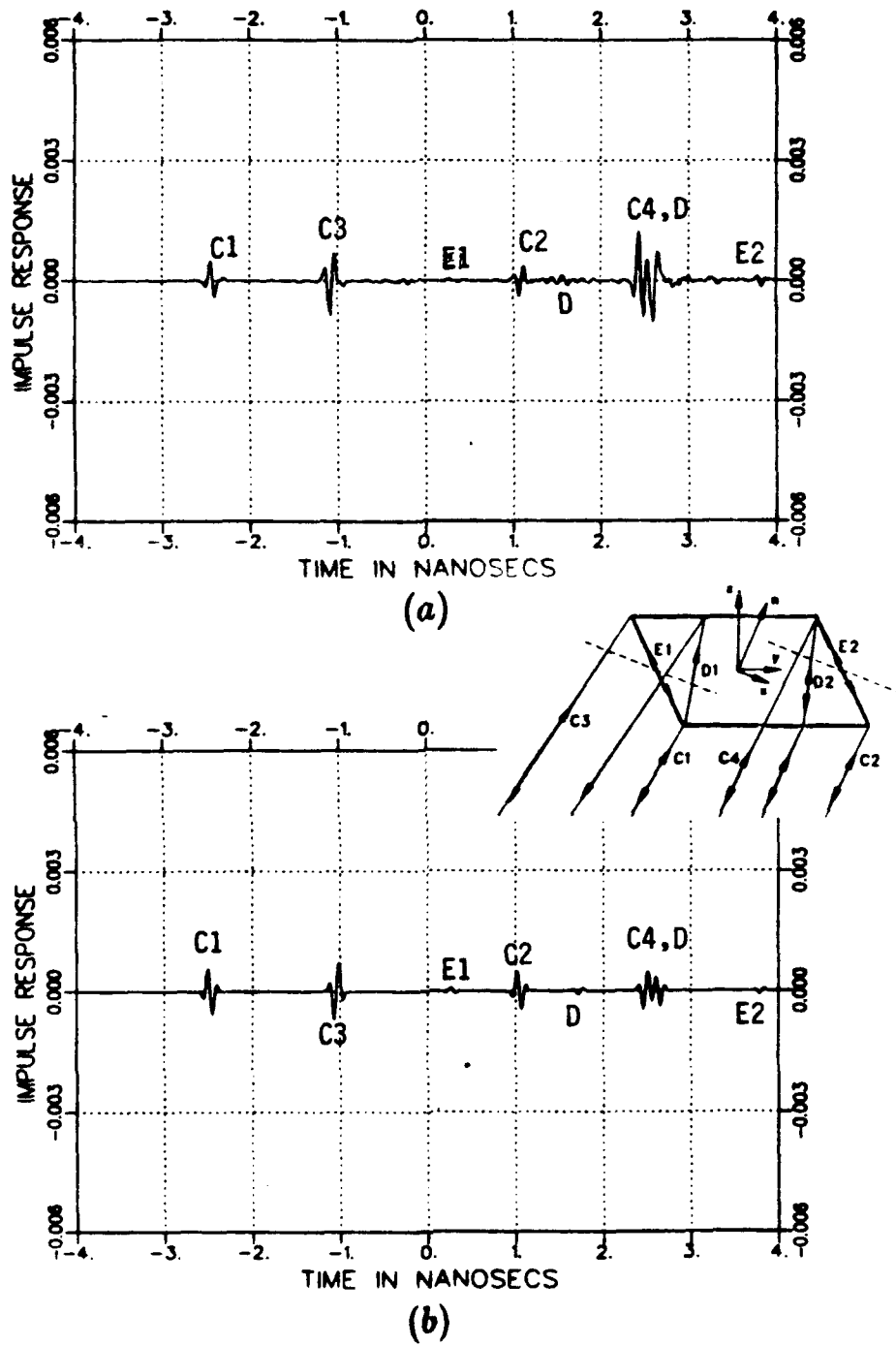


Figure 4.24: Impulse response of a 24" square plate at  $\phi = 45^\circ$  and  $\theta = 60^\circ$ . Cross polarization. (a) Measured, (b) Calculated.

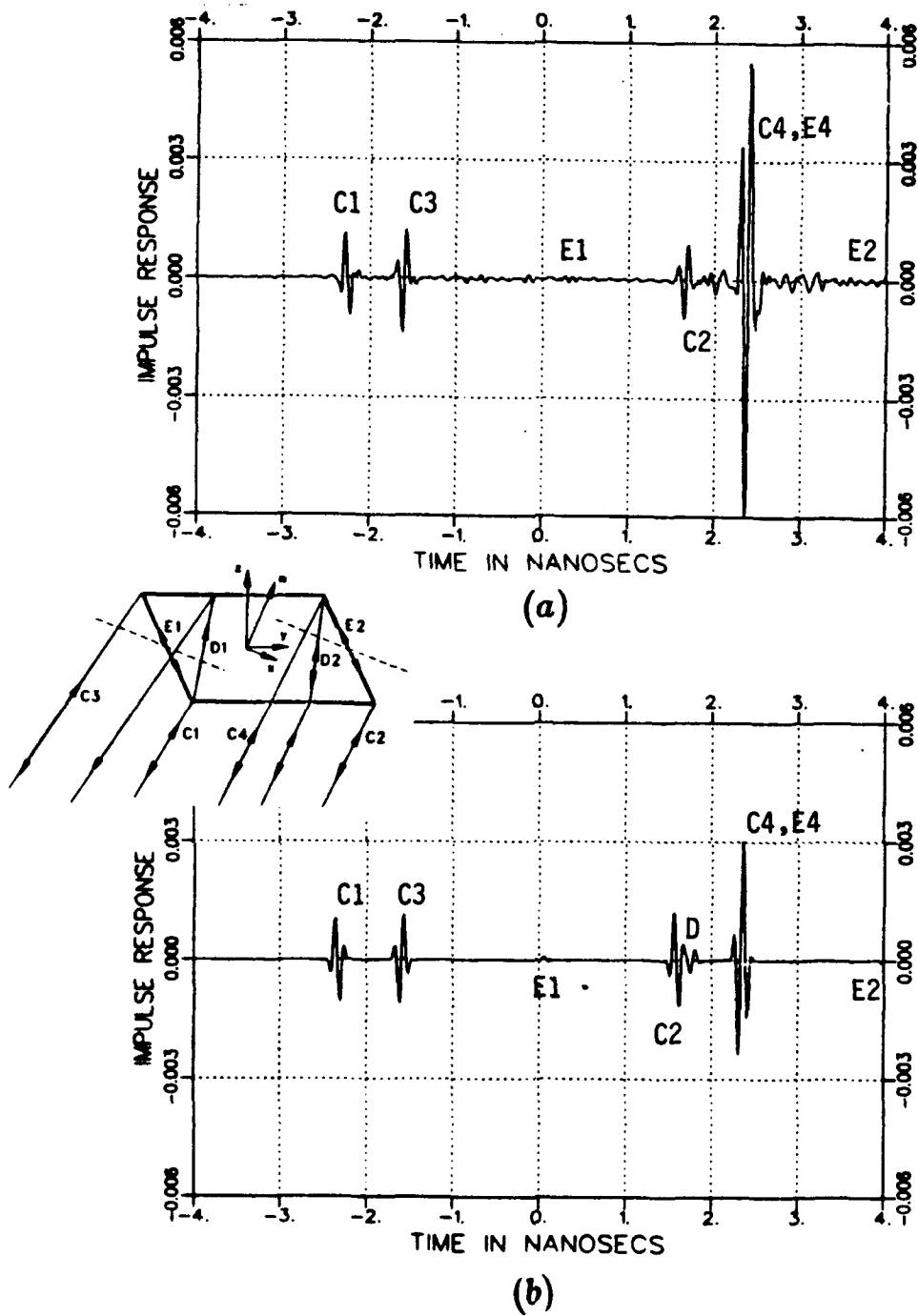


Figure 4.25: Impulse response of a 24" square plate at  $\phi = 45^\circ$  and  $\theta = 75^\circ$ . Cross polarization. (a) Measured, (b) Calculated.

## Chapter 5

# A Uniform Ray Approximation for the Interaction Between Edges of Three-Dimensional Polyhedral Structures

### 5.1 Introduction

A uniform ray representation of the interaction between edges of the three-dimensional far field region scattering by a flat plate structure is investigated. This is accomplished by (i) postulating an approximation of the induced surface current on each face composing the object, and (ii) integrating the approximate current, either in closed form, or asymptotically in terms of the well tabulated edge transition function. Specifically, the surface current on each plate composing the structure is approximated, in addition to the usual Physical Optics surface current, by a non-uniform current excited by each edge of the plate, which is derived from the canonical solution (integral representation) to the infinite wedge problem, and truncated at edges of the plate. The superposition of a secondary non-uniform current, which can be asymptotically represented by a Michaeli's fringe equivalent source, excited by doubly diffracted rays, is also studied as an additive correction to the first order solution.

## 5.2 A brief review of Michaeli's equivalent currents

A plane wave illuminates the infinite conducting wedge of Fig. 5.1. For convenience, we restrict our attention to face 1 of the wedge. The total current is the superposition of the well known Physical Optics current

$$\vec{j}^{po}(x, z) = 2\hat{n} \times \vec{H}^i(x, y, z)|_{v=0} \quad (5.1)$$

and a non-uniform component, which is in essence the current excited by

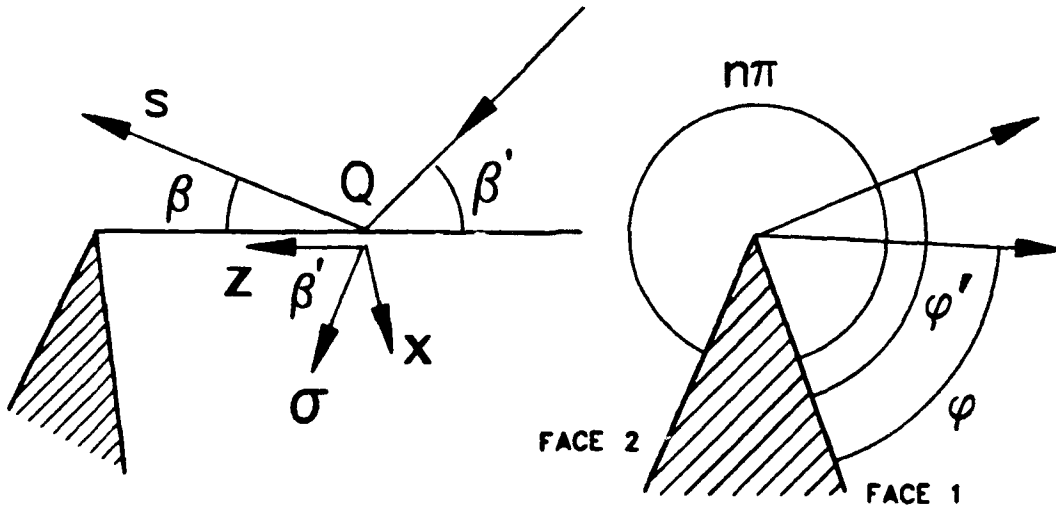


Figure 5.1: Infinite wedge illuminated by a plane wave.

the diffracted fields; it is depicted in Fig. 5.2 and explicitly described by the equations

$$j_e^{nu}(x, z) = \frac{jH_{0z}^i \exp(-jkz \cos \beta')}{4\pi n} \cdot \sum_{p,q=1}^2 \int_{\Gamma_q} \cot \left( \frac{\xi + (-1)^p \phi'}{2n} \right) \exp(-jkz \sin \beta' \cos \xi) d\xi, \quad (5.2)$$

$$j_z^{nu}(x, z) = -\frac{j \exp(-jkz \cos \beta')}{4\pi n}$$

$$\begin{aligned} & \cdot \sum_{p,q=1}^2 \int_{\Gamma_q} [(-1)^p Y E_{0z}^i \csc \beta' \sin \xi + H_{0z}^i \cot \beta' \cos \xi] \\ & \cdot \cot \left( \frac{\xi + (-1)^p \phi'}{2n} \right) \exp(-jkx \sin \beta' \cos \xi) d\xi. \quad (5.3) \end{aligned}$$

The various geometric parameters involved in the above expressions are

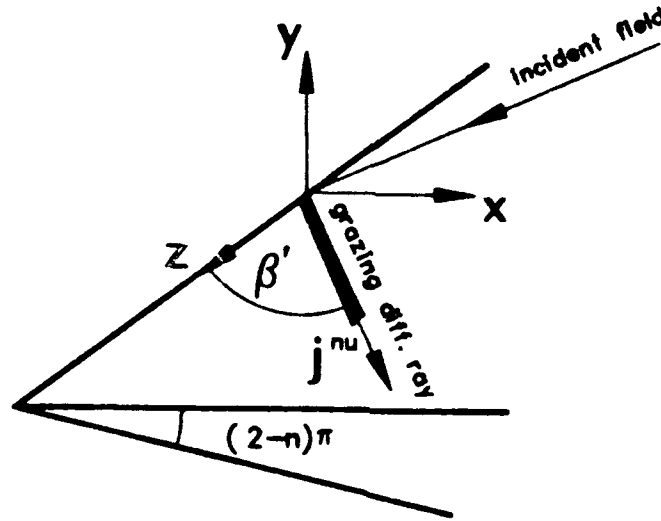


Figure 5.2: Non-uniform component of the current at the wedge.

shown in Fig. 5.1. The contours  $\Gamma_q$ ,  $q = 1, 2$ , are the steepest descent  $SDP(\pm\pi)$  paths through the saddle points at  $\xi = \pm\pi$  (Fig. 5.3). Eqs. (5.2), (5.3) in the case of the half plane, reduce to the expressions

$$\begin{aligned} j_x^{nu}(x, z) = & -\frac{4 \exp(j\pi/4)}{\sqrt{\pi} \sin \beta'} \exp[jk(x \sin \beta' \cos \phi' - z \cos \beta')] \\ & \cdot \left\{ (Y E_{0z}^i \sin \phi' - H_{0z}^i \cos \beta' \cos \phi') \right. \\ & \cdot F_-(\sqrt{2kx \sin \beta'} |\cos \frac{\phi'}{2}|) \text{sign}(\cos \frac{\phi'}{2}) \\ & + \frac{j}{\sqrt{2kx \sin \beta'}} \left( Y E_{0z}^i \sin \frac{\phi'}{2} - H_{0z}^i \cos \beta' \cos \frac{\phi'}{2} \right) \\ & \left. \cdot \exp(-2jkx \sin \beta' \cos^2 \frac{\phi'}{2}) \right\}, \quad (5.4) \end{aligned}$$

$$j_z^{nu}(x, z) = -\frac{4 \exp(j\pi/4) H_{0z}^i}{\sqrt{\pi}} \exp[jk(x \sin \beta' \cos \phi' - z \cos \beta')] \cdot F_-(\sqrt{2kx \sin \beta'} |\cos \frac{\phi'}{2}|) \text{sign}(\cos \frac{\phi'}{2}), \quad (5.5)$$

that involve the ordinary Fresnel integral

$$F_-(x) = \int_x^{+\infty} \exp(-jt^2) dt. \quad (5.6)$$

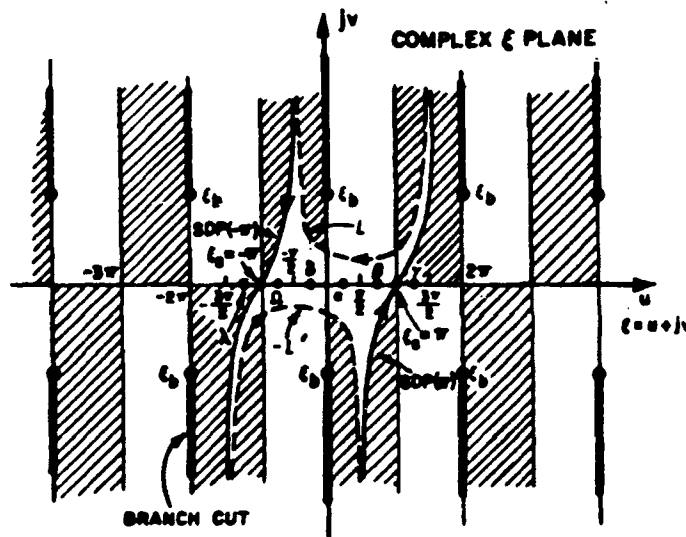


Figure 5.3: Steepest descent paths in the complex  $\xi$  plane (from [Pathak and Kouyoumjian, 1971]).

Accordingly, one relates a non-uniform field with the above currents. Provided that the smallest distance of the field point from the surface of the wedge is sufficiently large, the field associated with  $\vec{j}^{nu}$  can be approximated by

$$\vec{E}^{nu} \approx jkZ \int_{S_1} \hat{R} \times \hat{R} \times \vec{j}^{nu} \frac{\exp(-jkR)}{4\pi R} ds, \quad (5.7)$$

with  $S_1$  denoting the area of face 1 of the wedge. It has been shown by Michaeli [18,7] that the above surface integral can be reduced, via a linear

phase approximation, to a line integral of line magnetic and electric equivalent sources along the edge of the wedge. If one introduces the oblique system of coordinates related with the diffracted rays that graze the wedge surface, the electric and magnetic fringe edge currents evaluated at the point  $Q$  of the edge equal

$$I^{nu}(Q) = \frac{2j}{k} \left[ i_e^{nu}(\beta, \phi; \beta', \phi'; n) Y E_z^i(Q) + i_h^{nu}(\beta, \phi; \beta', \phi'; n) H_z^i(Q) \right] \quad (5.8)$$

and

$$M^{nu}(Q) = \frac{2j}{k} m_h^{nu}(\beta, \phi; \beta', \phi'; n) Z H_z^i(Q), \quad (5.9)$$

respectively, where

$$i_e^{nu}(\beta, \phi; \beta', \phi'; n) = -\frac{1}{\sin^2 \beta'} \left\{ \frac{\sin \phi' U(\pi - \phi')}{\mu + \cos \phi'} - \frac{1}{2n} \left[ \cot \left( \frac{\pi - (\gamma - \phi')}{2n} \right) - \cot \left( \frac{\pi - (\gamma + \phi')}{2n} \right) \right] \right\}, \quad (5.10)$$

$$i_h^{nu}(\beta, \phi; \beta', \phi'; n) = \frac{1}{\sin \beta'} \left\{ \frac{\cot \beta \cos \phi + \cot \beta' \cos \phi'}{\mu + \cos \phi'} U(\pi - \phi') + \frac{\mu \cot \beta' - \cot \beta \cos \phi}{2n \sin \gamma} \left[ \cot \left( \frac{\pi - (\gamma - \phi')}{2n} \right) + \cot \left( \frac{\pi - (\gamma + \phi')}{2n} \right) \right] \right\} - \frac{\cot \beta'}{n \sin \beta'}, \quad (5.11)$$

$$m_h^{nu}(\beta, \phi; \beta', \phi'; n) = \frac{\sin \phi}{\sin \beta \sin \beta'} \left\{ \frac{U(\pi - \phi')}{\mu + \cos \phi'} - \frac{1}{2n \sin \gamma} \left[ \cot \left( \frac{\pi - (\gamma - \phi')}{2n} \right) + \cot \left( \frac{\pi - (\gamma + \phi')}{2n} \right) \right] \right\}. \quad (5.12)$$

The expressions for the edge currents pertinent to the other face of the wedge are obtained by means of a simple transformation. The parameter

$\mu$  equals

$$\mu = \frac{\cos \psi - \cos^2 \beta'}{\sin^2 \beta'}, \quad (5.13)$$

with

$$\cos \psi = \hat{s}^d \cdot \hat{\sigma} = \sin \beta' \sin \beta \cos \phi + \cos \beta' \cos \beta, \quad (5.14)$$

and  $\hat{\sigma}$  is the unit vector in the direction of the grazing diffracted rays, whereas the angle  $\gamma$  is defined by

$$\mu = \cos \gamma, \quad (5.15)$$

along with the (arbitrary) choice of the branch, e.g., of that depicted in Fig. 5.4. This particular branch selection yields

$$\gamma = -j \ln(\mu + \sqrt{\mu^2 - 1}) \quad (5.16)$$

with

$$\sqrt{\mu^2 - 1} = \begin{cases} |\sqrt{\mu^2 - 1}| & ; |\mu| > 1 \\ j|\sqrt{1 - \mu^2}| & ; |\mu| < 1 \end{cases} \quad (5.17)$$

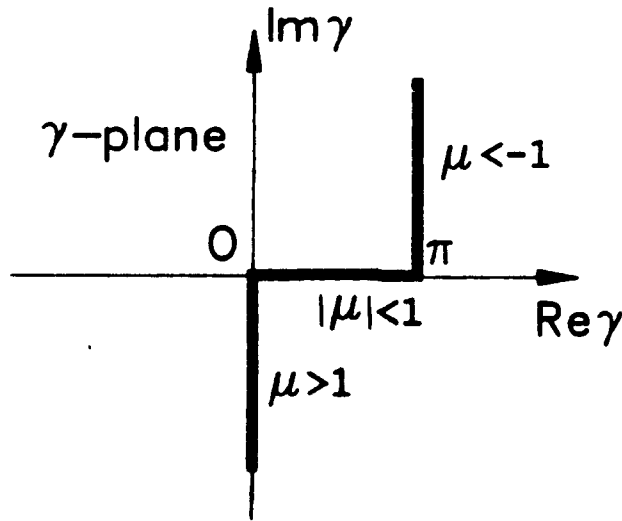


Figure 5.4: The complex  $\gamma$  plane.

It becomes clear from eqs. (5.8), (5.9) and eqs. (5.10)-(5.12) that the only circumstance under which the non-uniform edge equivalent currents

become singular is when  $\psi = 0$  (or  $\mu = 1$ ), which imply that  $\hat{\sigma} = \hat{s}$ . This singularity is integrable, unless simultaneously  $\phi' = \pi$ , which occurs at glancing incidence and forward scattering observation (Ufimtsev's singularity [14]). It should be noted, however, that Ufimtsev's singularity is eliminated when one integrates the non-uniform currents along a finite path in the  $\hat{\sigma}$  direction.

Michaeli's total currents on the other hand exhibit discontinuities as a result of the non-uniform asymptotic approximation of the physical optics surface currents. In general, for an infinite wedge, it is impossible to obtain uniform total edge currents if linear phase approximation is introduced for the reduction of the surface radiation integral to a line integral along the edges. Therefore, for the infinite wedge case one has to assume finite distances of the observation point from the edge and introduce a quadrature phase approximation, which will yield the expressions

$$I^{po}(Q) = \frac{2jU(\pi - \phi')}{k \sin^2 \beta'(\mu + \cos \phi')} \left[ Y E_z^i(Q) \sin \phi' - H_z^i(Q) \sin \beta'(\cot \beta \cos \phi + \cot \beta' \cos \phi') \right] \cdot F \left[ \frac{ks \sin^4 \beta'(\mu + \cos \phi')^2}{2 \sin^2 \psi} \right], \quad (5.18)$$

$$M^{po}(Q) = -\frac{2jZ H_z^i(Q) U(\pi - \phi') \sin \phi}{k \sin \beta' \sin \beta(\mu + \cos \phi')} F \left[ \frac{ks \sin^4 \beta'(\mu + \cos \phi')^2}{2 \sin^2 \psi} \right], \quad (5.19)$$

where  $F(\cdot)$  is the familiar edge transition function. Besides, in case of finite bodies, one may integrate directly and efficiently the Physical Optics surface currents [38].

### 5.3 Higher order terms using non-uniform surface wedge currents

The total surface current on each plate of the structure is approximated, as before, by the Physical Optics current and a non-uniform current excited by each edge of a given plate. The approximation is, in some respects, similar

with Michaeli's secondary equivalent current development [39]. However, the latter is restricted in the definition of a secondary edge current, which is then integrated numerically and, in addition, no explicit expression for the corner effect is given. Here, an attempt is made to present the total solution in terms of ray contributions, corresponding to tip, tip-to-edge and edge-to-tip diffracted rays. These rays result from the asymptotic surface current integration and, in general, do not satisfy Fermat's principle and, further, radiate as if the body was not present and, therefore, they are not shadowed. Nevertheless, the final solution is expected to be as efficient as GTD in high frequency calculations.

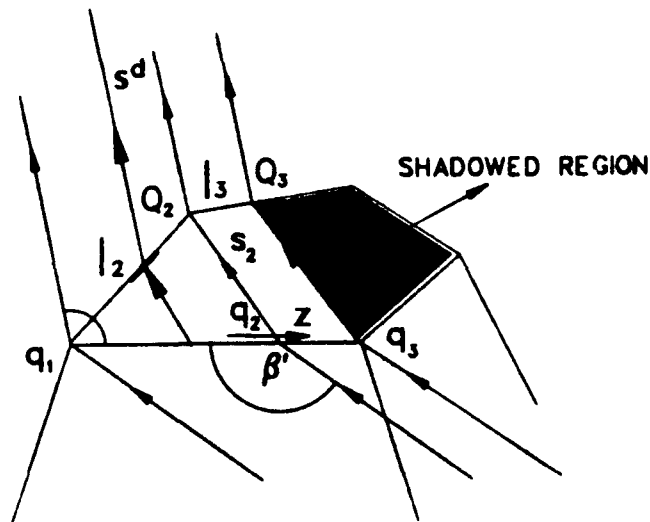


Figure 5.5: Non-uniform current excited by an edge and associated ray contributions at a polygonal structure illuminated by a plane wave.

Referring to Fig. 5.5, the exact non-uniform surface currents excited by edge (1) are truncated by edge (2), provided that at least part of edge (2) is illuminated by the diffracted rays emanating from edge (1) that graze the surface of the plate. Our analysis is restricted to the study of the non-uniform current emanating from edge (1) of the illustrated face of the object; similar arguments apply for any other edge of this plate and for any other plate of the body. The possible existence of shadow boundaries of the non-uniform surface current associated with each edge should be

emphasized. The discontinuities of the surface non-uniform current should be normally (in a PTD sense) compensated by an analogous discontinuous behavior of a tip excited current, which, however, remains unknown and it is not included.

One establishes the oblique coordinate system  $(\hat{\sigma}, \hat{\tau})$ , with  $\hat{\sigma}$  pointing to the direction of the grazing diffracted rays from edge (1) and  $\hat{\tau}$  being parallel to the edge vector. It is related with the edge (1) fixed cartesian system of coordinates via the linear transformation

$$x_1 = \sigma \sin \beta'_1, \quad z_1 = \tau + \sigma \cos \beta'_1. \quad (5.20)$$

Note that subscript 1 in the angles should imply reference to edge (1) fixed coordinate system. The field pertinent again to the non-uniform current emanating from edge (1) over the shown face of the object, and consistent with our postulate for the total current, is written as

$$\begin{aligned} \vec{E}^{nu} \approx & jkZ \sin \beta'_1 \frac{\exp(-jks)}{4\pi s} \hat{s}^d \times \hat{s}^d \times \\ & \int_{\tau_1}^{\tau_2} \int_0^{\sigma(\tau)} \vec{j}^{nu}(\sigma', \tau') \exp(jk\hat{s}^d \cdot \vec{r}') d\sigma' d\tau', \end{aligned} \quad (5.21)$$

since, in the far field,

$$R \approx s - \hat{s}^d \cdot (\sigma' \hat{\sigma} + \tau' \hat{\tau}) = s - \sigma \cos \psi - \tau \cos \beta_1, \quad (5.22)$$

with  $s$  being the distance from a fixed reference point on edge (1). Hence, one obtains

$$E_{\beta_1}^{nu} = -\frac{jkZ \sin \beta'_1 \exp(-jks)}{4\pi s} (\cos \beta_1 \cos \phi_1 I_x - \sin \beta_1 I_z), \quad (5.23)$$

$$E_{\phi_1}^{nu} = \frac{jkZ \sin \beta'_1 \exp(-jks)}{4\pi s} \sin \phi_1 I_x, \quad (5.24)$$

in which

$$I_{x,z} = \int_{\tau_1}^{\tau_2} \int_0^{\sigma(\tau)} j_{x,z}^{nu}(\sigma', \tau') \exp[jk(\sigma \cos \psi + \tau \cos \beta_1)] d\sigma' d\tau' \quad (5.25)$$

or

$$\begin{aligned} I_{x,z} = & J_{x,z} - K_{x,z} = \int_{\tau_1}^{\tau_2} \left( \int_0^{+\infty} - \int_{\sigma(\tau)}^{+\infty} \right) j_{x,z}^{nu}(\sigma', \tau') \\ & \cdot \exp[jk(\sigma \cos \psi + \tau \cos \beta_1)] d\sigma' d\tau'. \end{aligned} \quad (5.26)$$

The integrals  $J_{e,z}$  correspond to an edge (1) contribution to the non-uniform field. The latter is the field radiated by the Michaeli's fringe equivalent current and equals

$$\vec{E}^{(1)nu} = \vec{E}_2^{(1)nu} - \vec{E}_1^{(1)nu}, \quad (5.27)$$

with

$$\vec{E}_m^{(1)nu} = \frac{\sin \beta_1}{4\pi(\cos \beta_1 - \cos \beta'_1)} \left[ \hat{\beta}_1 Z I^{nu}(q_m) - \hat{\phi}_1 M^{nu}(q_m) \right] \frac{\exp[-jk(s - \hat{s}^d \cdot \vec{r}_{Q_m})]}{s}, \quad (5.28)$$

The edge currents  $I^{nu}$  and  $M^{nu}$  have been defined by eqs. (5.8)-(5.9) and

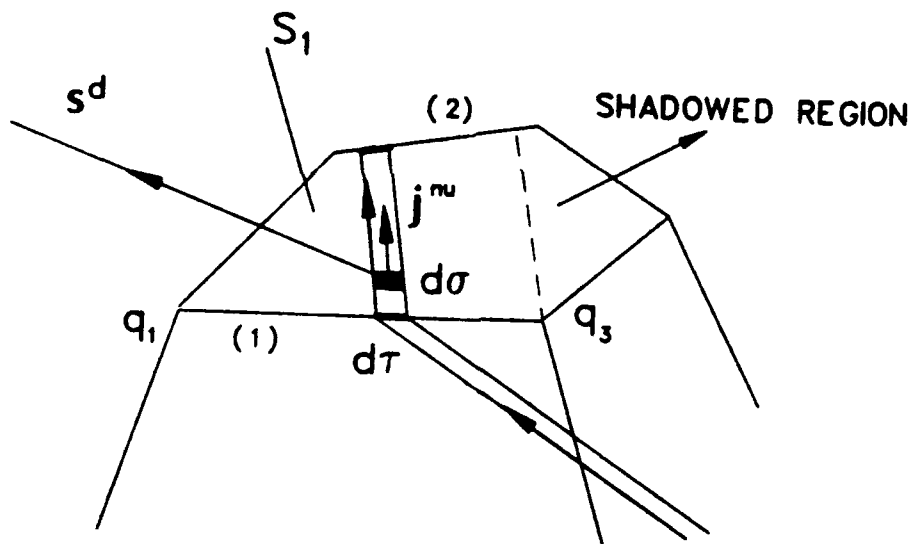


Figure 5.6: Geometry for the surface current integration.

(5.10)-(5.12). The field of eq. (5.28), when superimposed to the Physical Optics contribution is equivalent to the GTD corner diffraction recently developed by Brinkley and Marhefka [2].

On the other hand, the integrals  $K_{e,z}$ , corresponding to a truncation effect of the primary non-uniform current, with the use of eqs. (5.2) and

(5.3), are written explicitly as

$$K_z = \frac{jH_{0z}^i}{4\pi n_1} \sum_{p,q=1}^2 \int_{\Gamma_q} \cot\left(\frac{\xi + (-1)^p \phi_1'}{2n_1}\right) K(\xi) d\xi, \quad (5.29)$$

$$K_z = \frac{-j}{4\pi n_1} \sum_{p,q=1}^2 \int_{\Gamma_q} [(-1)^p Y E_{0z}^i \csc \beta_1' \sin \xi + H_{0z}^i \cot \beta_1' \cos \xi] \cot\left(\frac{\xi + (-1)^p \phi_1'}{2n_1}\right) K(\xi) d\xi, \quad (5.30)$$

where  $K(\xi)$  denotes the simple integral

$$K(\xi) = \int_{\tau_1}^{\tau_2} \exp[jk\tau'(\cos \beta_1 - \cos \beta_1')] \cdot \int_{\sigma(\tau')}^{+\infty} \exp[jk\sigma' \sin^2 \beta_1'(\mu + \cos \xi)] d\sigma' d\tau', \quad (5.31)$$

which can be trivially evaluated. It can be easily seen that

$$\sigma(\tau') = \tau' \sin \alpha / \sin(\beta_1' - \alpha) + B, \quad (5.32)$$

where  $\alpha$  is the angle between edge (2) and edge (1) in the counterclockwise direction and  $B$  is a constant. Hence,

$$K(\xi) = K_2(\xi) - K_1(\xi), \quad (5.33)$$

with

$$K_m(\xi) = \frac{\sin(\beta_1' - \alpha)}{k^2 \sin \alpha \sin^4 \beta_1'} \frac{\exp[jks_m \sin^2 \beta_1' \cos^2(\xi/2)]}{(\mu + \cos \xi)(\nu + \cos \xi)} \cdot \exp[jk(\hat{s}^i \cdot \vec{r}_{q_m} - s_m + \hat{s}^d \cdot \vec{r}_{Q_m})], \quad m = 1, 2, \quad (5.34)$$

where  $s_m = |q_m \vec{Q}_m|$ ,  $\mu$  has been defined by eq. (5.13), while

$$\begin{aligned} \nu &= \cos \delta = \mu + \frac{\sin(\beta_1' - \alpha)}{\sin \alpha \sin^2 \beta_1'} (\cos \beta_1 - \cos \beta_1') \\ &= \frac{\sin \alpha \sin \beta_1 \cos \phi_1 + \cos \alpha (\cos \beta_1 - \cos \beta_1')}{\sin \alpha \sin \beta_1'}. \end{aligned} \quad (5.35)$$

Incorporating eq. (5.34) into eqs. (5.29) and (5.30) one obtains

$$K_{(m)x} = \frac{-2 \sin(\beta'_1 - \alpha) H_z^i(q_m)}{k^2 \sin^4 \beta'_1} W_m^{(1)}(\beta_1, \phi_1; \beta'_1, \phi'_1) \cdot \exp[jk(\hat{s}^d \cdot \vec{r}_{Q_m} - s_m)], \quad (5.36)$$

$$K_{(m)z} = \frac{2 \sin(\beta'_1 - \alpha)}{k^2 \sin^5 \beta'_1} \left[ Y E_z^i(q_m) W_m^{(2)}(\beta_1, \phi_1; \beta'_1, \phi'_1) + H_z^i(q_m) \cos \beta'_1 W_m^{(3)}(\beta_1, \phi_1; \beta'_1, \phi'_1) \right] \cdot \exp[jk(\hat{s}^d \cdot \vec{r}_{Q_m} - s_m)]. \quad (5.37)$$

In the above expressions:

$$W_m^{(1)}(\beta, \phi; \beta', \phi') = \frac{1}{8n_1 \pi j \sin \alpha} \sum_{p=1}^2 \int_{\Gamma_1 + \Gamma_2} \frac{\cot \left( \frac{\xi + (-1)^p \phi'}{2n_1} \right) \exp[2jk s_m \cos^2(\xi/2)]}{(\mu + \cos \xi)(\nu + \cos \xi)}, \quad (5.38)$$

$$W_m^{(2)}(\beta, \phi; \beta', \phi') = \frac{1}{8n_1 \pi j \sin \alpha} \sum_{p=1}^2 (-1)^p \int_{\Gamma_1 + \Gamma_2} \frac{\sin \xi \cot \left( \frac{\xi + (-1)^p \phi'}{2n_1} \right) \exp[2jk s_m \cos^2(\xi/2)]}{(\mu + \cos \xi)(\nu + \cos \xi)}, \quad (5.39)$$

and

$$W_m^{(3)}(\beta, \phi; \beta', \phi') = \frac{1}{8n_1 \pi j \sin \alpha} \sum_{p=1}^2 \int_{\Gamma_1 + \Gamma_2} \frac{\cos \xi \cot \left( \frac{\xi + (-1)^p \phi'}{2n_1} \right) \exp[2jk s_m \cos^2(\xi/2)]}{(\mu + \cos \xi)(\nu + \cos \xi)}. \quad (5.40)$$

The pertinent field quantities related with the truncation effect read

$$\begin{aligned}
 E_{(m)\beta_1}^{(2)nu} = & -\frac{j \sin(\beta'_1 - \alpha)}{2\pi k \sin^3 \beta'_1} \left\{ E_z^i(q_m) \frac{\sin \beta_1}{\sin \beta'_1} W_m^{(2)}(\beta_1, \phi_1; \beta'_1, \phi'_1) \right. \\
 & + Z H_z^i(q_m) \left[ \cos \beta_1 \cos \phi_1 W_m^{(1)}(\beta_1, \phi_1; \beta'_1, \phi'_1) \right. \\
 & \left. \left. + \sin \beta_1 \cot \beta'_1 W_m^{(3)}(\beta_1, \phi_1; \beta'_1, \phi'_1) \right] \right\} \\
 & \frac{\exp[-jk(s + s_m - \hat{s}^d \cdot \vec{r}_{Q_m})]}{s}, \tag{5.41}
 \end{aligned}$$

and

$$\begin{aligned}
 E_{(m)\phi_1}^{(2)nu} = & \frac{j Z H_z^i(q_m) \sin(\beta'_1 - \alpha) \sin \phi_1}{2\pi k \sin^3 \beta'_1} W_m^{(1)}(\beta_1, \phi_1; \beta'_1, \phi'_1) \\
 & \frac{\exp[-jk(s + s_m - \hat{s}^d \cdot \vec{r}_{Q_m})]}{s}. \tag{5.42}
 \end{aligned}$$

It should be noted that the distance between  $q_m$  and  $Q_m$  -denoted by  $s_m$ - may be zero in case of adjacent edges or large when  $q_m$  and  $Q_m$  do not coalesce. Thus, the integrals  $W_m^{(1)}$ ,  $W_m^{(2)}$  and  $W_m^{(3)}$  can be evaluated in closed form when  $s_m = 0$  via the Cauchy's residue theorem and asymptotically for large values of  $s_m$  via the extended Pauli-Clemmow method of steepest descent. In the former case, one obtains

$$\begin{aligned}
 W_m^{(1)}(\beta, \phi; \beta', \phi') = & \frac{U(\pi - \phi')}{\sin \alpha(\mu + \cos \phi')(\nu + \cos \phi')} \\
 & \frac{\sin^2 \beta'}{n_1 \sin(\beta' - \alpha)(\cos \beta - \cos \beta')} \\
 & \left[ \frac{\csc \gamma \sin \left( \frac{\pi - \gamma}{n_1} \right)}{\cos \frac{\phi'}{n_1} - \cos \left( \frac{\pi - \gamma}{n_1} \right)} - \frac{\csc \delta \sin \left( \frac{\pi - \delta}{n_1} \right)}{\cos \frac{\phi'}{n_1} - \cos \left( \frac{\pi - \delta}{n_1} \right)} \right], \tag{5.43}
 \end{aligned}$$

$$\begin{aligned}
 W_m^{(2)}(\beta, \phi; \beta', \phi') = & -\frac{U(\pi - \phi') \sin \phi'}{\sin \alpha(\mu + \cos \phi')(\nu + \cos \phi')} \\
 & + \frac{\sin^2 \beta' \sin \frac{\phi'}{n_1}}{n_1 \sin(\beta' - \alpha)(\cos \beta - \cos \beta')}
 \end{aligned}$$

$$\left[ \frac{\sin\left(\frac{\pi-\gamma}{n_1}\right)}{\cos\frac{\phi'}{n_1} - \cos\left(\frac{\pi-\gamma}{n_1}\right)} - \frac{\sin\left(\frac{\pi-\delta}{n_1}\right)}{\cos\frac{\phi'}{n_1} - \cos\left(\frac{\pi-\delta}{n_1}\right)} \right], \quad (5.44)$$

$$W_m^{(3)}(\beta, \phi; \beta', \phi') = \frac{U(\pi - \phi') \cos \phi'}{\sin \alpha (\mu + \cos \phi') (\nu + \cos \phi')} + \frac{\sin^2 \beta'}{n_1 \sin(\beta' - \alpha) (\cos \beta - \cos \beta')} \cdot \left[ \frac{\cot \gamma \sin\left(\frac{\pi-\gamma}{n_1}\right)}{\cos\frac{\phi'}{n_1} - \cos\left(\frac{\pi-\gamma}{n_1}\right)} - \frac{\cot \delta \sin\left(\frac{\pi-\delta}{n_1}\right)}{\cos\frac{\phi'}{n_1} - \cos\left(\frac{\pi-\delta}{n_1}\right)} \right], \quad (5.45)$$

whereas, a uniform asymptotic expansion of these integrals, with an error that does not exceed  $O(1/\kappa_m)$ , with  $\kappa_m = ks_m \sin^2 \beta$ , yields

$$W_m^{(1)}(\beta, \phi; \beta', \phi') \approx \frac{\exp(-j\pi/4)}{4n_1 \sqrt{2\pi ks_m} \sin \alpha \sin \beta'} \cdot \sum_{p,q=1}^2 a_{pq} \cot\left(\frac{\pi + (-1)^{p+q+1}\phi'}{2n_1}\right) \cdot \left[ \frac{F(\kappa_m a_{pq})}{a_{pq}(a_{pq} - c)(a_{pq} - d)} + \frac{F(\kappa_m c)}{c(c - a_{pq})(c - d)} + \frac{F(\kappa_m d)}{d(d - a_{pq})(d - c)} \right], \quad (5.46)$$

$$W_m^{(2)}(\beta, \phi; \beta', \phi') \approx 0, \quad (5.47)$$

$$W_m^{(3)}(\beta, \phi; \beta', \phi') \approx -W_m^{(1)}(\beta, \phi; \beta', \phi'), \quad (5.48)$$

in which

$$c = 1 - \mu, \quad d = 1 - \nu, \quad (5.49)$$

and

$$a_{pq} = 1 + \cos[2n_1 N_{pq} \pi - (-1)^p \phi'], \quad (5.50)$$

where  $N_{pq}$  integers most nearly satisfying the equations

$$2n_1 N_{pq} \pi - (-1)^p \phi' = (-1)^{q+1} \pi. \quad (5.51)$$

One can, with no difficulty [40], obtain higher order terms of the asymptotic expansion of the integrals (5.38) - (5.40).

## 5.4 Secondary non-uniform edge equivalent currents

The analysis of the radiation of the first order non-uniform currents by edge (1) merely included the effect of truncation of these currents by the other edges of the plate. Of equivalent significance is the contribution from a secondary effect which arises from the non-uniform currents that are excited by edge (2) due to the field diffracted by edge (1) that grazes the plate and illuminates a section of edge (2), as illustrated in Fig. 5.7.

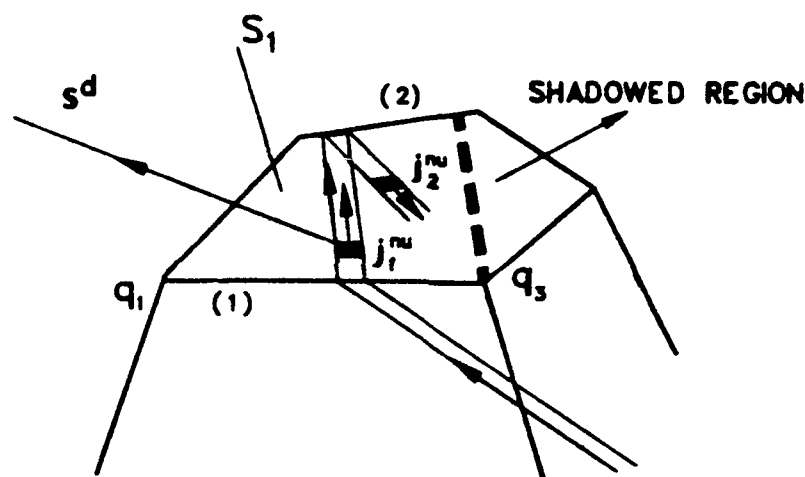


Figure 5.7: The secondary non-uniform current.

A similar approximation has been developed by Sikta [11], who considered a secondary edge current induced by the field diffracted by edge (1). However, his development has been based on a modified version of Ryan and Peters equivalent currents [17], and though it provided reasonable results for several flat plate geometries, it is questioned conceptually [39]. A natural modification of Sikta's idea, within the frame of an asymptotic PTD approach, is the additive correction of the solution developed in Section 3.1 by the radiation of secondary non-uniform equivalent sources along edge (2), which at each point are proportional to the tangential component

(to edge (2)) magnetic field diffracted by edge (1) and evaluated via UTD.

Referring to Michaeli [7], the non-uniform current along edge (2) excited by the UTD diffracted field from edge (1) can be written in the form

$$I^{d,nu}(z_2) = \frac{2j}{k} i_h^{nu}(\beta_2, \phi_2; \beta'_2, 0; n_2) \frac{\vec{H}^d(z_2) \cdot \hat{z}_2}{2} \quad (5.52)$$

and

$$M^{d,nu}(z_2) = \frac{2j}{k} m_h^{nu}(\beta_2, \phi_2; \beta'_2, 0; n_2) \frac{\vec{H}^d(z_2) \cdot \hat{z}_2}{2}, \quad (5.53)$$

where  $i_h^{nu}(\beta'_2, 0; \beta_2, \phi_2)$  and  $m_h^{nu}(\beta'_2, 0; \beta_2, \phi_2)$  are determined from eqs. (5.11) and (5.12), while the magnetic component  $\vec{H}^d$  of the UTD diffracted field from edge (1) equals

$$\begin{aligned} \vec{H}^d = & \frac{-Y E_{\phi'_1}^i \exp(-j\pi/4)}{n_1 \sqrt{2\pi k}} \left[ \cot\left(\frac{\pi - \phi'_1}{2n_1}\right) F[k\sigma \sin^2 \beta'_1 a^+(\phi'_1)] \right. \\ & \left. + \cot\left(\frac{\pi + \phi'_1}{2n_1}\right) F[k\sigma \sin^2 \beta'_1 a^-(\phi'_1)] \right] \frac{\exp(-jk\sigma)}{\sqrt{\sigma}} \hat{\beta}_1, \quad (5.54) \end{aligned}$$

where [16]

$$a^\pm(\phi'_1) = 1 + \cos(2n_1 N^\pm \pi \pm \phi'_1) \quad (5.55)$$

and  $N^\pm$  integers most nearly satisfying

$$2n_1 N^\pm \pi \pm \phi'_1 = \pi. \quad (5.56)$$

It should be also noted that a factor of 1/2 has been introduced in eqs. (5.52) and (5.53) due to grazing incidence.

Accordingly, the field associated with the secondary non-uniform equivalent currents defined by eqs. (5.52), (5.53) is given by

$$\begin{aligned} \vec{E}^{d,nu} \approx & jkZ \sin \beta_2 \frac{\exp(-jks)}{4\pi s} \\ & \cdot \int_{l_2} [\hat{\beta}_2 Z I^{d,nu}(z_2) - \hat{\phi}_2 M^{d,nu}(z_2)] \exp[jk\hat{s}^d \cdot \vec{r}^i(z_2)] dz_2 \quad (5.57) \end{aligned}$$

where the integration takes place along the illuminated (by the rays diffracted from edge (1)) section of edge (2). The above expression involves

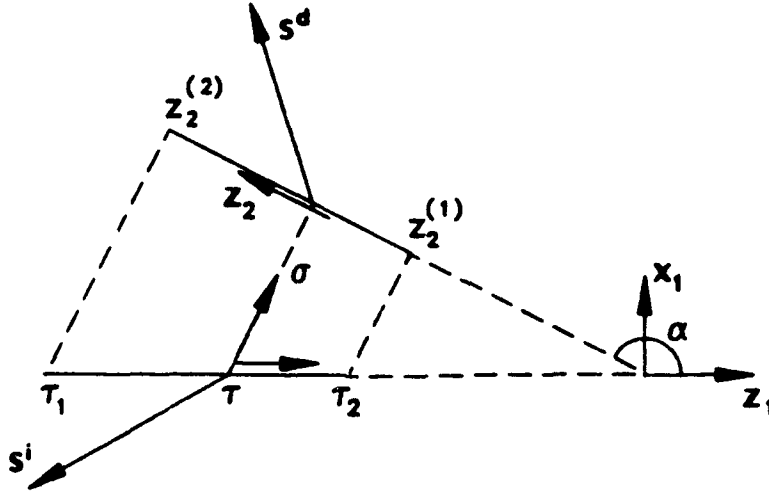


Figure 5.8: Non-parallel edges geometry.

integrals of the form

$$I = \int_{z_2^{(1)}}^{z_2^{(2)}} \frac{F[k\sigma(z_2) \sin^2 \beta'_1 a(\phi'_1)]}{\sqrt{\sigma(z_2)}} \exp\{jk[\hat{s}^i \cdot \vec{r}(z_2) - \sigma(z_2) + \hat{s}^d \cdot \vec{r}'(z_2)]\} dz_2. \quad (5.58)$$

Although the UTD diffracted field from edge (1) is not a valid approximation when a corner is approached, because either the edge itself is approached or, at the tip, the field structure is more involved than a simple superposition of singly and multiply diffracted rays, the closed form integration of  $I$  is not expected to yield a different result from a numerical integration along an interval that excludes a small region close to the tip, due to the regularity of the integrands. Besides, closed form results provide the necessary insight for the assesment of the solution and the possibility of plausible heuristic modifications.

If the edges are parallel the integration in eq. (5.58) is trivial. Let us consider the interaction between two non-parallel edge as shown in Fig. 5.8. One can integrate along the direction  $\hat{\tau}$  as shown in Fig. 5.6 by performing a simple linear transformation of variables. Since  $\sigma(\tau) = A\tau$ , where

$$A = \frac{\sin \alpha}{\sin(\beta'_1 - \alpha)},$$

and using the explicit definition of the  $F(\cdot)$  function, as well as the fact

$$\hat{s}^i \cdot \vec{r}(\tau) - \sigma(\tau) + \hat{s}^d \cdot \vec{r}^i(\tau) = \frac{\tau \sin \alpha \sin^2 \beta'_1}{\sin(\beta'_1 - \alpha)} (\nu - 1)$$

eq. (5.58) becomes

$$I = \frac{\sin \beta'_1}{\sin \beta'_2} 2j \sqrt{k \sin^2 \beta'_1 a(\phi'_1)} \int_{\tau_1}^{\tau_2} \exp\{jkA\tau \sin^2 \beta'_1 [a(\phi'_1) - (1 - \nu)]\} \int_{\sqrt{kA\tau a(\phi'_1) \sin^2 \beta'_1}}^{+\infty} \exp(-jv^2) dv d\tau, \quad (5.59)$$

where  $\cos \beta'_2 = \hat{z}_2 \cdot \hat{\sigma}$ .

The surface integral

$$J = \int_{\tau_1}^{\tau_2} \exp(j\eta\tau) \int_{\sqrt{\zeta\tau}}^{+\infty} \exp(-jv^2) dv d\tau \quad (5.60)$$

can be written as

$$J = J_2 - J_1, \quad (5.61)$$

with

$$J_m = \int_{v_m}^{+\infty} \exp(-jv^2) \int_{\tau_m}^{v^2/\zeta} \exp(j\eta\tau) d\tau dv. \quad (5.62)$$

The latter can be expressed in closed form in terms of the standard Fresnel integral as follows:

$$J_m = \frac{1}{j\eta} \left\{ \frac{1}{|1 - \eta/\zeta|} \int_{v_m \sqrt{|1 - \eta/\zeta|}}^{+\infty} \exp(\mp v^2) - \exp(j\eta\tau_m) \int_{v_m}^{+\infty} \exp(-jv^2) dv \right\}, \quad 1 - \eta/\zeta \gtrless 0. \quad (5.63)$$

Application of the above result into eq. (5.59) yields

$$I = I_2 - I_1, \quad (5.64)$$

where

$$\begin{aligned}
I_m = & \frac{\sin \beta'_1}{\sin \beta'_2} 2j \sqrt{ka(\phi'_1) \sin^2 \beta'_1} \frac{1}{jkA \sin^2 \beta'_1 [a(\phi'_1) - (1 - \nu)]} \\
& \cdot \left\{ \sqrt{\frac{a(\phi'_1)}{|1 - \nu|}} \int_{\sqrt{ks_m \sin^2 \beta'_1 |1 - \nu|}}^{+\infty} \exp(\mp jt^2) dt \right. \\
& \left. - \exp\{jk s_m \sin^2 \beta'_1 [a(\phi'_1) - (1 - \nu)]\} \int_{\sqrt{ks_m \sin^2 \beta'_1 a(\phi'_1)}}^{+\infty} \exp(-jt^2) dt \right\} \\
& 1 - \nu \geq 0
\end{aligned} \tag{5.65}$$

One can simplify the above expression in terms of the edge transition function, namely

$$I_m = \frac{-j \sin(\beta'_1 - \alpha)}{k \sin \alpha \sin \beta'_1 \sin \beta'_2 (1 - \nu) \sqrt{s_m}} F^d(\kappa_m; a(\phi'_1), 1 - \nu), \tag{5.66}$$

where  $\kappa_m = ks_m \sin^2 \beta'_1$  and

$$F^d(\kappa; a_1, a_2) = \frac{a_1 F(\kappa a_2) - a_2 F(\kappa a_1)}{a_1 - a_2}. \tag{5.67}$$

Substituting the result (5.66) into eq. (5.57) one obtains two terms associated with the end points of the line radiation integral, namely

$$\vec{E}^{d,nu} = \vec{E}_2^{d,nu} - \vec{E}_1^{d,nu}, \tag{5.68}$$

in which

$$\begin{aligned}
\vec{E}_m^{d,nu} = & E_{\phi'_1}^i(q_m) \frac{\exp(j\pi/4) \sin(\beta'_1 - \alpha) \sin \beta_2}{2n_1 (2\pi k)^{3/2} \sin \alpha \sin \beta'_1 (1 - \nu)} \\
& \cdot [\hat{\beta}_2 i_h^{nu}(\beta_2, \phi_2; \beta'_2, 0; n_2) - \hat{\phi}_2 m_h^{nu}(\beta_2, \phi_2; \beta'_2, 0; n_2)] \\
& \cdot \left\{ \cot\left(\frac{\pi - \phi'_1}{2n_1}\right) F^d(\kappa_m; \alpha^+(\phi'_1), 1 - \nu) \right. \\
& \left. + \cot\left(\frac{\pi + \phi'_1}{2n_1}\right) F^d(\kappa_m; \alpha^-(\phi'_1), 1 - \nu) \right\} \\
& \frac{\exp[-jk(s_m - \hat{s}^d \cdot \vec{r}_{q_m})]}{\sqrt{s_m}}.
\end{aligned} \tag{5.69}$$

When the points  $Q_m$  and  $q_m$  coalesce, as in the case of adjacent edges one can repeat a similar analysis to identify a corner effect pertinent to the secondary non-uniform current. However, since the integrals involve regular functions one can simply take the limit of the field in eq. (5.69) as  $s_m \rightarrow 0$ . It can thus be trivially shown that for  $s_m = 0$

$$\begin{aligned} \vec{E}_m^{d,nu} = & \frac{j \sin(\beta'_1 - \alpha) \sin \beta_2}{4\sqrt{2n_1} \pi k \sin \alpha (1 - \nu)} \left[ \hat{\beta}_2 i_h^{nu}(\beta_2, \phi_2; \beta'_2, 0; n_2) \right. \\ & \left. - \hat{\phi}_2 m_h^{nu}(\beta_2, \phi_2; \beta'_2, 0; n_2) \right] \\ & \cdot \left\{ \cot \left( \frac{\pi - \phi'_1}{2n_1} \right) F^c(a^+(\phi'_1), 1 - \nu) \right. \\ & \left. + \cot \left( \frac{\pi + \phi'_1}{2n_1} \right) F^c(a^-(\phi'_1), 1 - \nu) \right\} \\ & \cdot \frac{\exp[-jk(s_m - \hat{s}^d \cdot \vec{r}_{Q_m})]}{s}, \end{aligned} \quad (5.70)$$

where

$$F^c(a^\pm, 1 - \nu) = \frac{\sqrt{a^\pm} \sqrt{1 - \nu}}{\sqrt{a^\pm} + \sqrt{1 - \nu}}, \quad (5.71)$$

along with the following selection of the branch:

$$\sqrt{1 - \nu} = \begin{cases} |\sqrt{1 - \nu}| & ; 1 - \nu > 0 \\ -j|\sqrt{1 - \nu}| & ; 1 - \nu < 0 \end{cases} \quad (5.72)$$

It should be noted that the apparent singularity in eqs. (5.69) and (5.70) when  $\nu \rightarrow 1$  is canceled by an analogous singularity of the second term composing the total interaction between any pair of edges.

## 5.5 Numerical results and discussion

The effect of the truncation effect of the primary non-uniform current, outlined in Sec. 5.3, as well as the contribution of the secondary non-uniform current, presented in Sec. 5.4, has been investigated in monostatic and bistatic cross section computations of several plate geometries and they have been compared against the corner diffraction solution [2] as well as the Method of Moments. It should be emphasized that the approach is not

complete in many aspects. For instance, from a PTD point of view particular components of the currents (e.g., a rigorous tip excited current, an edge wave current, currents excited by multiply bouncing rays, etc.) have not been included. Further, the predicted fields due to the inexact depiction of the currents do not satisfy reciprocity. However, the present solution appears as a computational efficient means to accurately approximate in several cases the scattered fields.

The two levels of approximation of the currents and the associated fields are indicated as "asymptotic solution" and "asymptotic solution +" at the plots. In Figs. 5.9 and 5.10 the effect of the incorporation of the higher order current effects is evident away from broadside. It should be noted that for principal plane observation only a  $\hat{\phi}$  polarized incident wave is expected to excite higher order interactions between opposite edges of the square plate, and, indeed, this is the case where the superposition of secondary effects improve the pattern. On the contrary, the corner diffraction solution is adequate in the  $\hat{\theta}$  polarized case. The minor discrepancy when grazing incidence is approached may be attributed to a slope effect which has not been incorporated at the time.

The effect of the primary non-uniform wedge current is also clear in bistatic pattern calculations for the same  $5\lambda$  square plate. The secondary current appears of minor importance in this example, except in the case of the  $\sigma_{\theta\phi}$  cross-section. When the plate becomes smaller and the incident field is closer to the plane of the plate, the contribution from doubly diffracted rays predicted via the presented asymptotic analysis becomes more significant as shown in Figs. 5.15-5.18 where the bistatic cross section of a  $2\lambda$  square plate is studied.

Sikta's triangle is another example where the method is outlined. Although the solution has a remarkable effect in the sidelobes close to broadside and when nose-on incidence is approached, it fails to predict the appreciable field at the vicinity of the  $\phi = 150^\circ$  angle for the  $\hat{\phi}$  polarization. This discrepancy may arise either because of an inaccurate prediction of the corner diffracted field from the back tip, or due to a strong tip-to-edge diffracted ray (which is not included due to the two-dimensional and non-reciprocal nature of our approximation), or, finally, by travelling waves along the edges of the triangle.

Future work on the same level should focus on a more rigorous development of the secondary non-uniform current using concepts of the Spectral

Theory of Diffraction. This should enable the study of slope effects and should lead into a more symmetric solution. The truncation of the secondary non-uniform by adjacent corner is also under investigation. Further, careful study of the individual ray mechanisms constituting the total solution may enable heuristic modifications, based on empirical arguments, and corrections in certain regions of deficiency. A more involved study should concentrate in direct or indirect approaches towards the investigation of the corner phenomenon.

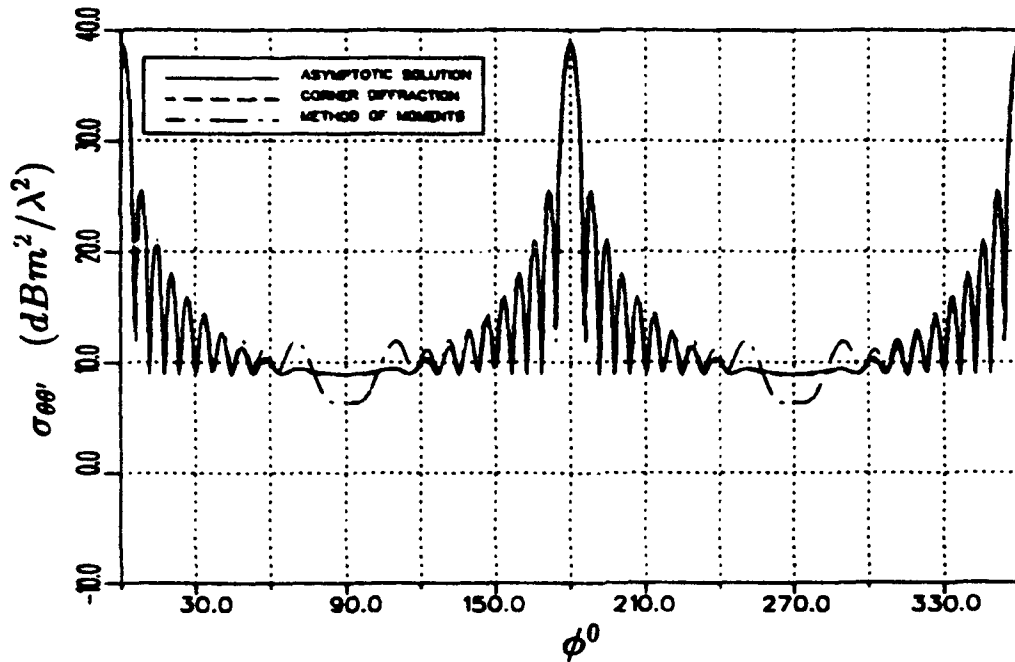


Figure 5.9: Principal plane RCS  $\sigma_{\theta\theta'}$  of a  $5\lambda$  square plate.

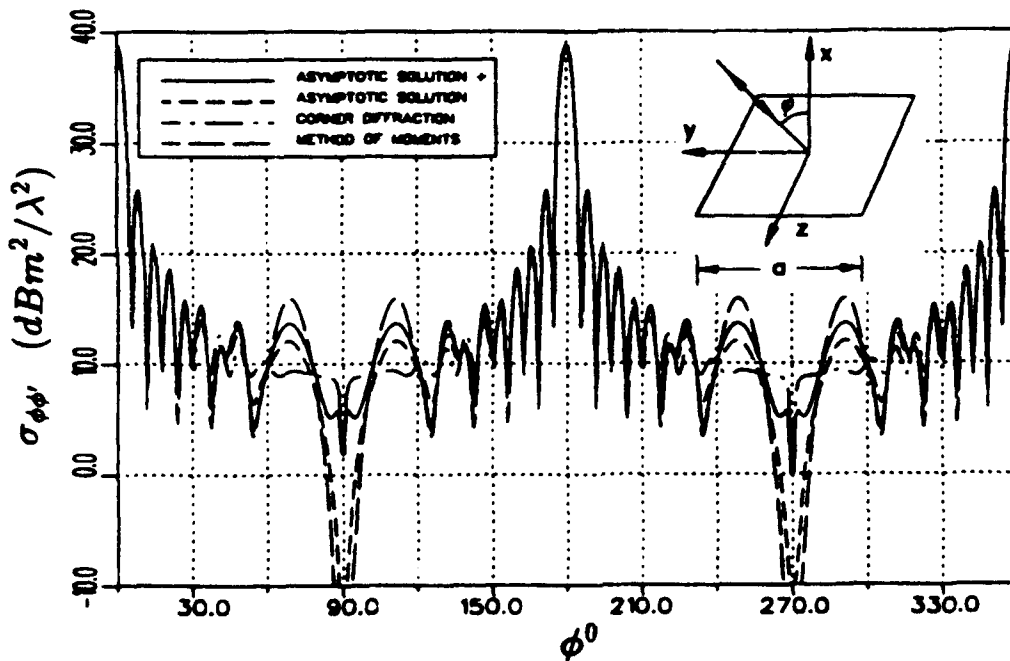


Figure 5.10: Principal plane RCS  $\sigma_{\phi\phi'}$  of a  $5\lambda$  square plate.

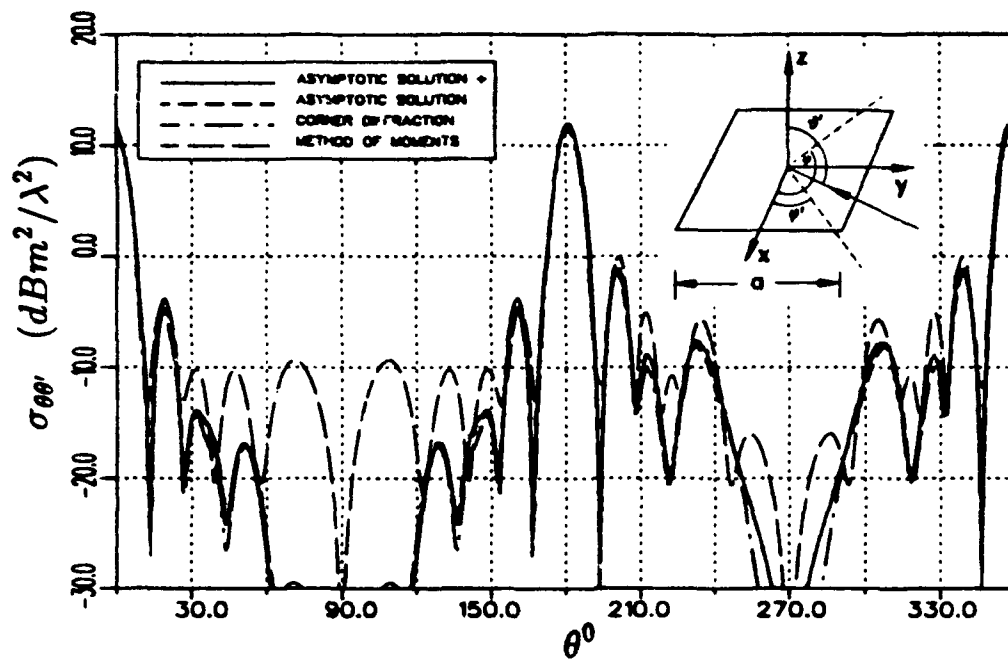


Figure 5.11: Bistatic cross section  $\sigma_{\theta\theta'}$  of a  $5\lambda$  square plate for  $\theta' = 45^\circ$  and  $\phi' = 0^\circ$  at  $\phi = 60^\circ$ .

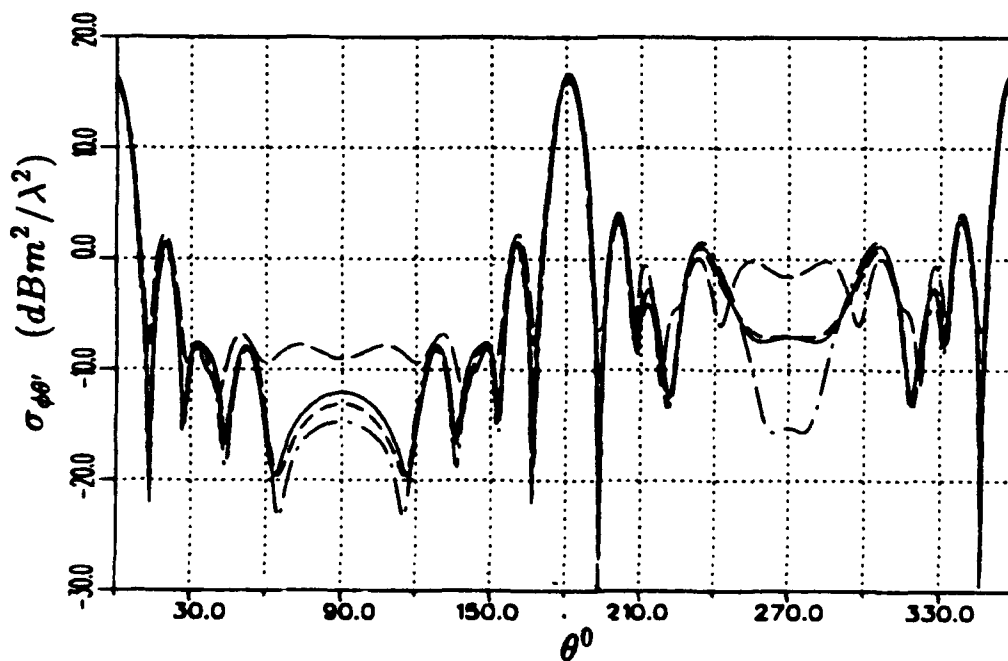


Figure 5.12: Bistatic cross section  $\sigma_{\phi\phi'}$  of a  $5\lambda$  square plate for  $\theta' = 45^\circ$  and  $\phi' = 0^\circ$  at  $\phi = 60^\circ$ .

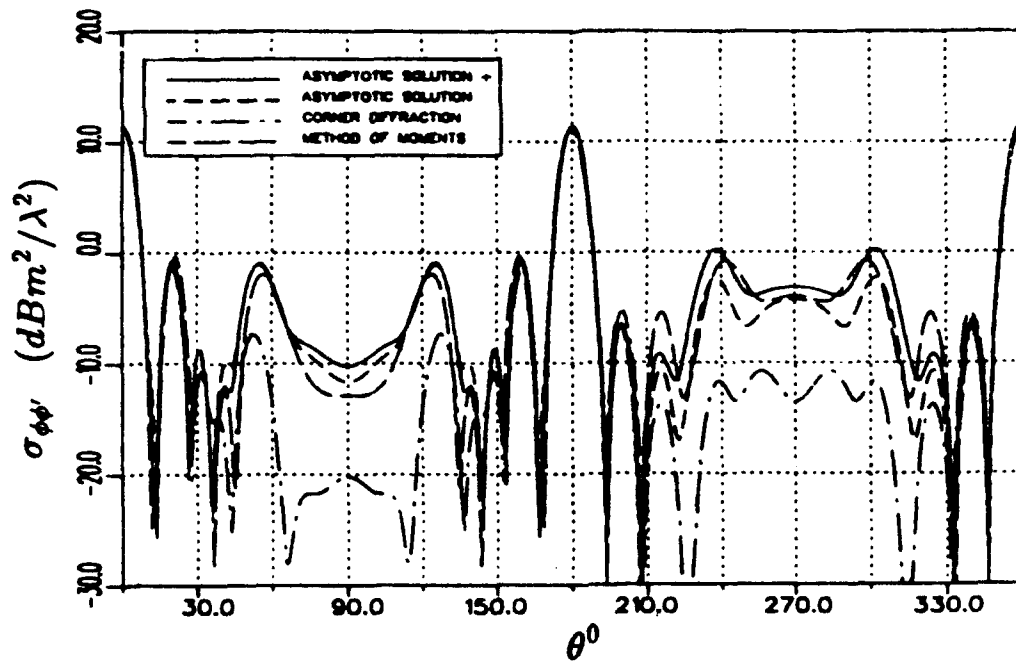


Figure 5.13: Bistatic cross section  $\sigma_{\phi\phi'}$  of a  $5\lambda$  square plate for  $\theta' = 45^\circ$  and  $\phi' = 0^\circ$  at  $\phi = 60^\circ$ .

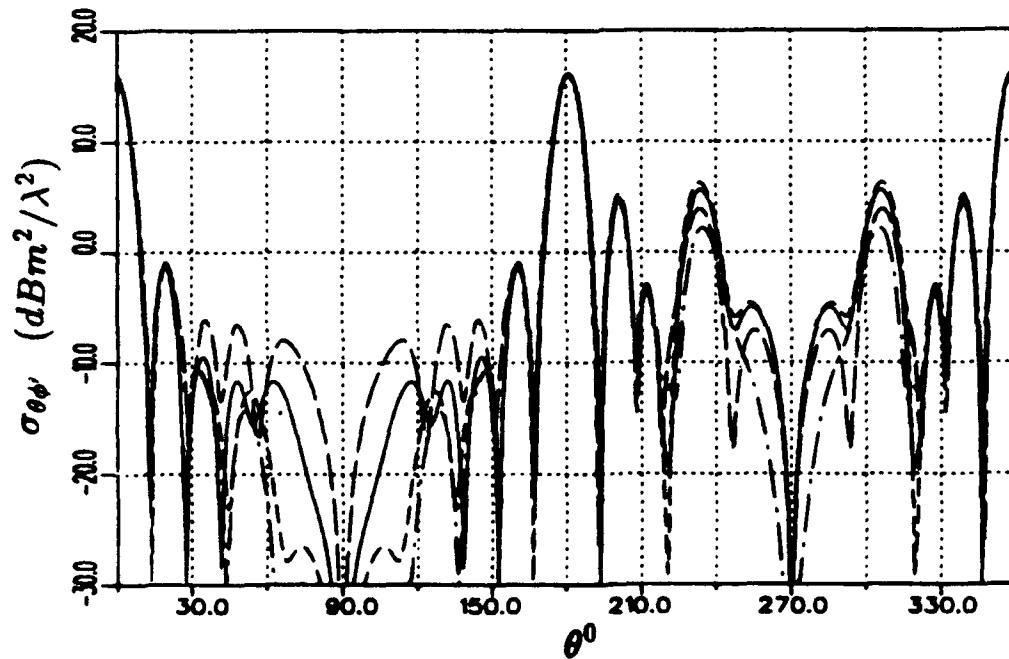


Figure 5.14: Bistatic cross section  $\sigma_{\theta\phi'}$  of a  $5\lambda$  square plate for  $\theta' = 45^\circ$  and  $\phi' = 0^\circ$  at  $\phi = 60^\circ$ .

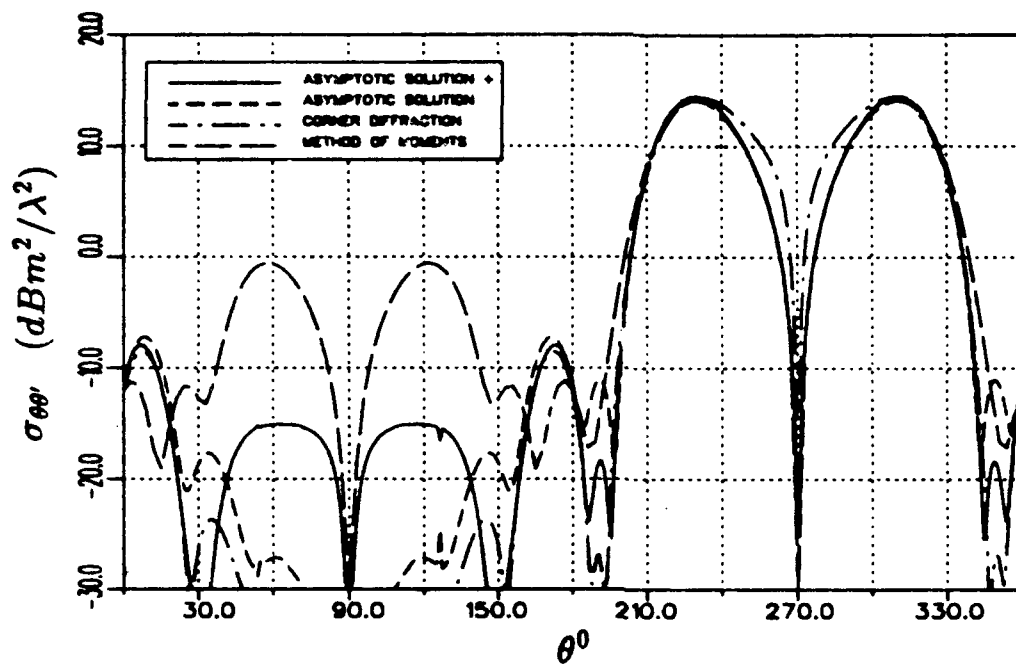


Figure 5.15: Bistatic cross section  $\sigma_{\theta\theta'}$  of a  $2\lambda$  square plate for  $\theta' = 60^\circ$  and  $\phi' = 45^\circ$  at  $\phi = 60^\circ$ .

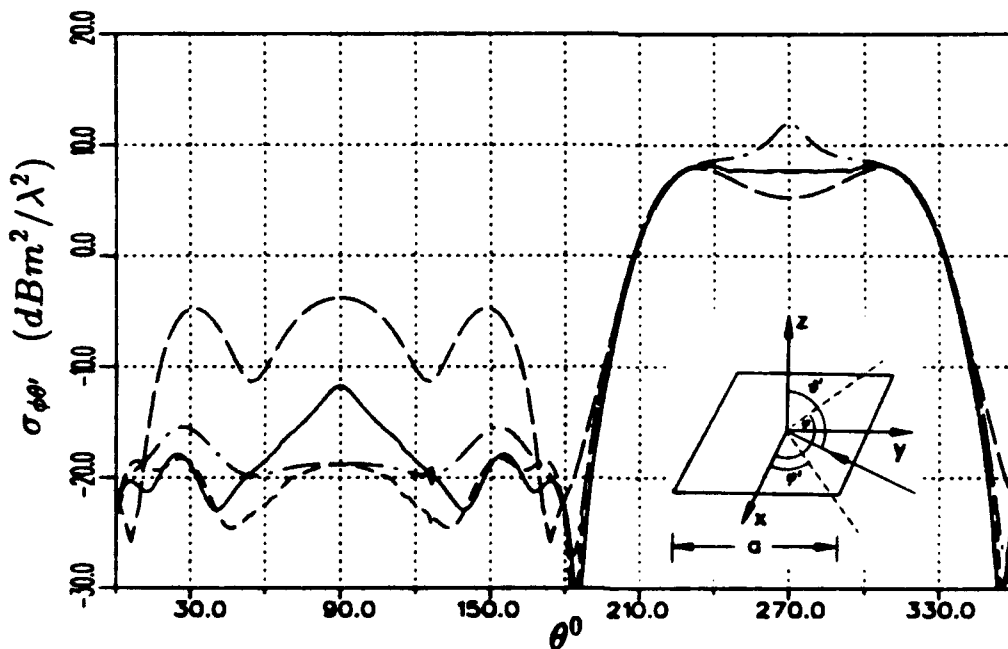


Figure 5.16: Bistatic cross section  $\sigma_{\phi\theta'}$  of a  $2\lambda$  square plate for  $\theta' = 60^\circ$  and  $\phi' = 45^\circ$  at  $\phi = 60^\circ$ .

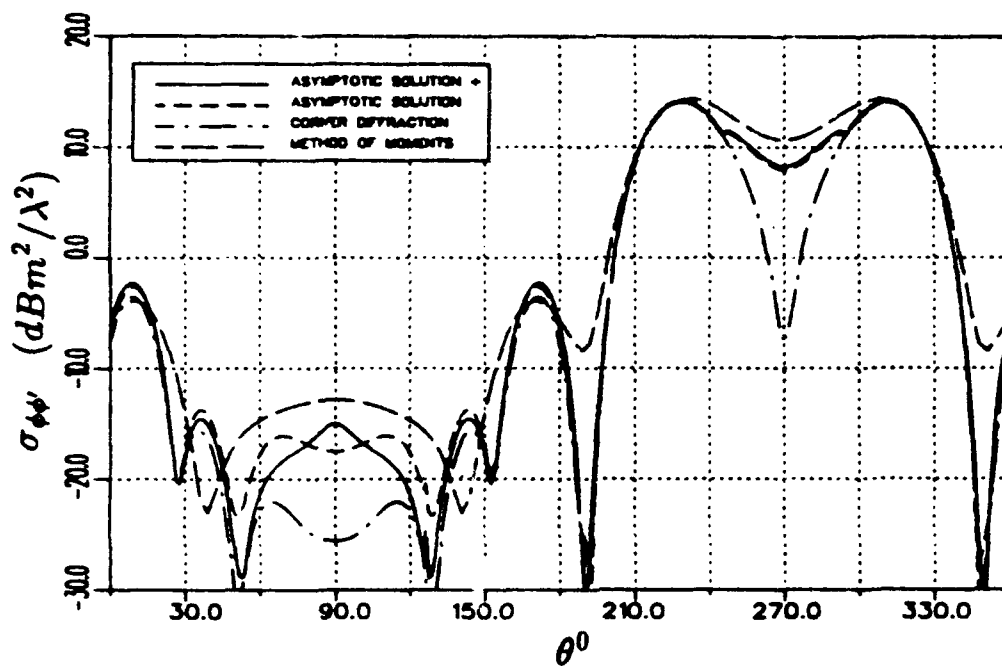


Figure 5.17: Bistatic cross section  $\sigma_{\phi\psi}$  of a  $2\lambda$  square plate for  $\theta' = 60^\circ$  and  $\phi' = 45^\circ$  at  $\phi = 60^\circ$ .

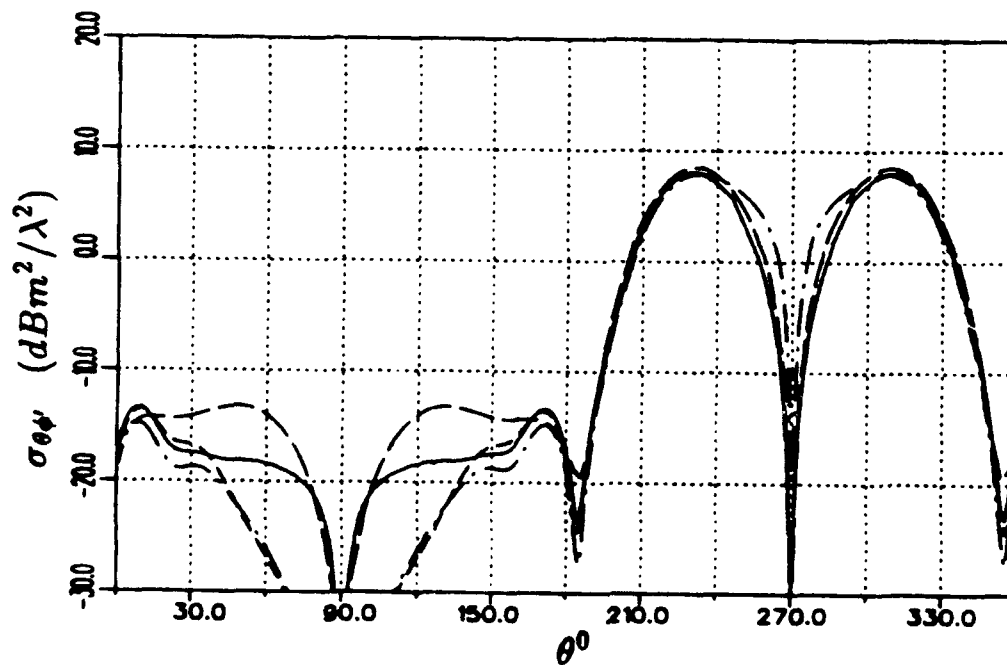


Figure 5.18: Bistatic cross section  $\sigma_{\theta\phi}$  of a  $2\lambda$  square plate for  $\theta' = 60^\circ$  and  $\phi' = 45^\circ$  at  $\phi = 60^\circ$ .

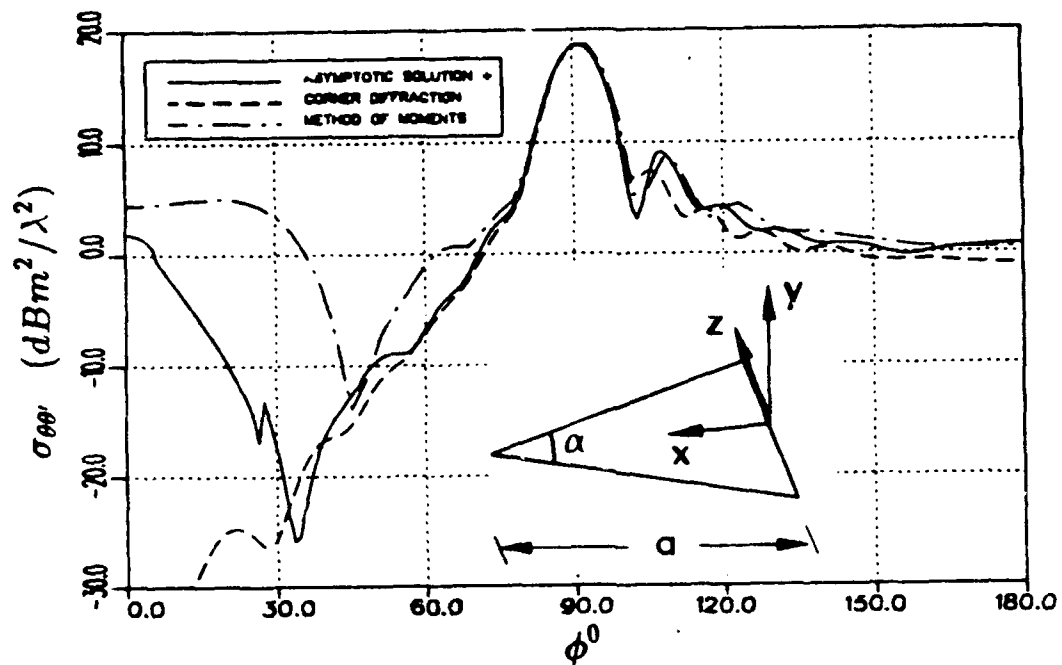


Figure 5.19: RCS  $\sigma_{\theta\theta}$  of Sikta's triangle with  $a = 3\lambda$  and  $\alpha = 30^\circ$  at  $\theta = 90^\circ$ .

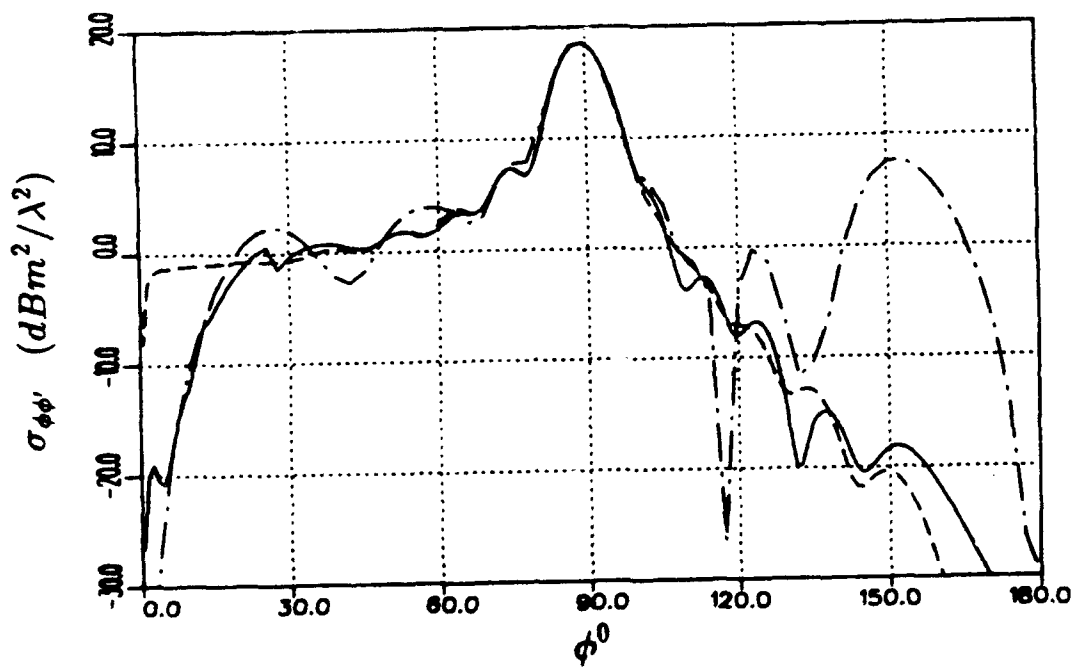


Figure 5.20: RCS  $\sigma_{\phi\phi}$  of Sikta's triangle with  $a = 3\lambda$  and  $\alpha = 30^\circ$  at  $\theta = 90^\circ$ .

# Chapter 6

## Summary

This report summarizes the major theoretical studies pertaining to the scattering from flat plate structures. A new far zone corner diffraction coefficient has been developed and tested against existing solutions, method of moments, and measurements. It has been shown to be very useful and accurate for backscatter and especially for bistatic scattering where many of the previous methods give less accurate results. A new method for determining an edge wave - vertex diffraction coefficient for dipole excitation near an edge has also been developed. It is tested against method of moments and measurements with excellent results. This is an intermediate step for determining a far zone edge wave solution. This edge wave solution for plane wave incidence has been approximately developed by relating the first corner as if it is a source of the edge waves and the use of reciprocity. It is tested against method of moments and high resolution time domain measurements for a plate. The higher order diffractions across the face of the plates has also been developed. It includes corner to edge, edge to corner, and corner to corner type diffraction mechanisms. It is based on the truncation of the edge generated currents at opposite edges making up a plate structure.

The theories in this study have been developed in such a way as to be useful for efficient algorithms to be used in user oriented computer codes. They have been included in a simple user oriented code called the Radar Cross Section - Basic Scattering Code (RCS-BSC Version 2). It allows the use of multiple edged flat plate structures that can be put together to make polyhedral shapes. It also allows composite elliptic cone frustum shapes

and ellipsoids to model curved surfaces. Monostatic or bistatic results for the complete scattering matrix are obtained. The input of the shapes is based on a simple command word system.

## Appendix A

# Asymptotic Evaluation of an Integral for Edge Waves

We outline the uniform asymptotic approximation of the integral

$$I_{-p}(k) = \int_0^{\infty} t^{p-1} G(t) \exp\{jkg(t)\} dt, \quad (\text{A.1})$$

for  $\Re(p) > 0$ , in terms of the large parameter  $k$ . (To assure convergence of intermediate integrals, let the parameter  $k$  have a small negative imaginary part.) In eq. (A.1),  $G(t)$  is a slowly varying regular function of  $t$ . For our purposes, and without loss of generality, it is assumed that  $g'(0) = \text{sign}(t_s)|g'(0)|$ , with  $g'(t_s) = 0$ , and  $g''(t) < 0$ , for every  $t$ . For  $t_s > 0$  the major contribution to the integral arises from the vicinity of the stationary phase point ( $t = t_s$ ) and the end point, which coincides with the branch point singularity of the integrand.

In the particular case  $p = 1/2$ , one introduces the transformation  $\xi = \sqrt{t}$  and with  $H(\xi) = G(\xi^2)$ ,  $h(\xi) = g(\xi^2)$  rewrites eq. (A.1) as

$$I_{-1/2}(k) = 2 \int_0^{\infty} H(\xi) \exp\{jkh(\xi)\}, \quad (\text{A.2})$$

where, now,  $h(\xi)$  exhibits three collinear, equidistant saddle points at  $\xi_0 = 0$ ,  $\xi_{1,2} = \pm\sqrt{t_s}$ . This case is treated in detail in [41]. Specifically, introducing the transformation

$$h(\xi) = a_0 - (a + s^2)^2, \quad (\text{A.3})$$

with

$$a_0 = h(\xi_{1,2}) = g(t_s),$$

$$a = -\text{sign}(t_s) \sqrt{h(\xi_{1,2}) - h(0)} = -\text{sign}(t_s) \sqrt{g(t_s) - g(0)},$$

and from the definition of the parabolic cylinder function

$$D_{-p}(z) = \frac{\exp(-z^2/4)}{\Gamma(p)} \int_0^\infty t^{p-1} \exp(-zt - t^2/2) dt, \quad \Re(p) > 0, \quad (\text{A.4})$$

and the formula [42]

$$D_{-p}(z) = \exp(jp\pi) D_{-p}(-z) + \frac{\sqrt{2\pi}}{\Gamma(p)} \exp\{j(p-1)\pi/2\} D_{p-1}(jz), \quad (\text{A.5})$$

$$I_{-1/2}(k) \approx \frac{\sqrt{\pi} \exp(-j\pi/8)}{(2k)^{1/4}} \exp\{jk(a_0 - a^2/2)\} \sqrt{2|a|} \cdot \begin{cases} \frac{G(0)}{\sqrt{|g'(0)|}} j D_{-1/2}[\exp(j\pi/4)|a|\sqrt{2k}] \\ + \frac{G(t_s)}{\sqrt{|t_s g''(t_s)|}} \sqrt{2} \exp(-j\pi/4) D_{-1/2}[\exp(-j\pi/4)|a|\sqrt{2k}]; & t_s > 0 \\ \frac{G(0)}{\sqrt{|g'(0)|}} D_{-1/2}[\exp(j\pi/4)|a|\sqrt{2k}]; & t_s < 0 \end{cases} \quad (\text{A.6})$$

It should be noted [41] that, when  $a$  is small,

$$\frac{d\xi}{ds} \Big|_{s=0} = \sqrt{\frac{2|a|}{|g'(0)|}} \approx \sqrt{\frac{2|a|}{|t_s g''(t_s)|}} \approx \left[ \frac{2}{|g''(0)|} \right]^{1/4}. \quad (\text{A.7})$$

In the more general case of arbitrary  $p$ , a rather heuristic approach has been implemented. For instance, the derivation of the end point contribution is obtained by introducing the expansion

$$g(t) \approx g(0) + g'(0)t + \frac{g''(0)}{2}t^2. \quad (\text{A.8})$$

The resulting canonical integral can be expressed in terms of the parabolic cylinder function of order  $-p$ . Thus,

$$I_{-p}^0(k) \approx G(0) \Gamma(p) (2k)^{-p/2} \exp(-jp\pi/4) \exp\{jk[g(0) + a^2/2]\} \cdot \left[ \frac{|g'(0)|}{2|a|} \right]^{-p} \begin{cases} \exp(jp\pi) D_{-p}[\exp(j\pi/4)|a|\sqrt{2k}]; & t_s > 0 \\ D_{-p}[\exp(j\pi/4)|a|\sqrt{2k}]; & t_s < 0 \end{cases}. \quad (\text{A.9})$$

# Bibliography

- [1] R. J. Marhefka, "Radar cross section - basic scattering code, RCS - BSC (version 2), user's manual," Technical Report 718295-15, The Ohio State University ElectroScience Laboratory, Department of Electrical Engineering, Jan. 1990. Prepared under Contract No. F33615-86-K-1023 for Wright Patterson Air Force Base.
- [2] T. J. Brinkley and R. J. Marhefka, "Far zone bistatic scattering from flat plates," Technical Report 718295-8, The Ohio State University ElectroScience Laboratory, Department of Electrical Engineering, July 1988. Prepared under Contract No. F33615-86-K-1023 for Wright Patterson Air Force Base.
- [3] R. J. Marhefka and T. J. Brinkley, "Comparison of methods for far zone scattering from a flat plate and cube," *Applied Computational Electromagnetic Society Journal and Newsletter*, vol. 3, pp. 57-78, Fall 1988.
- [4] L. P. Ivriissimtzis and R. J. Marhefka, "Edge wave edge and vertex diffraction," Technical Report 718295-9, The Ohio State University ElectroScience Laboratory, Department of Electrical Engineering, July 1988. Prepared under Contract No. F33615-86-K-1023 for Wright Patterson Air Force Base.
- [5] L. P. Ivriissimtzis and R. J. Marhefka, "Edge wave vertex- and edge-diffraction,". To appear in *Radio Science*.
- [6] F. A. Sikta, W. D. Burnside, T. T. Chu, and L. Peters, Jr., "First-order equivalent current and corner diffraction scattering from flat plate structures," *IEEE Trans. Antennas Propagat.*, vol. AP-31, pp. 584-589, July 1983.

- [7] A. Michaeli, "Elimination of infinities in equivalent edge currents, Part I: fringe current components," *IEEE Trans. Antennas Propagat.*, vol. AP-34, pp. 912-918, 1986.
- [8] E. H. Newman and R. L. Dilsavor, "A user's manual for the electromagnetic surface patch code: ESP Version III," Technical Report 716148-19, The Ohio State University ElectroScience Laboratory, Department of Electrical Engineering, May 1987.
- [9] A. C. Ludwig, "Backscattering from a cube," *Applied Computational Electromagnetic Society Journal and Newsletter*, vol. 2, pp. 55-73, Fall 1987.
- [10] R. Tiberio, G. Manara, G. Pelosi, and R. G. Kouyoumjian, "High-frequency electromagnetic scattering of plane waves from double wedges," *IEEE Trans. Antennas Propagat.*, vol. 37, pp. 1172-1180, Sep. 1989.
- [11] F. A. Sikta and L. Peters, Jr., "UTD analysis of electromagnetic scattering by flat plate structures," Technical Report 711930-2, The Ohio State University ElectroScience Laboratory, Department of Electrical Engineering, 1981.
- [12] R. J. Marhefka and J. W. Silvestro, "Near zone - basic scattering code, user's manual with space station applications," Technical Report 716199-13, The Ohio State University ElectroScience Laboratory, Department of Electrical Engineering, March 1989. Prepared under Grant No. NSG 1498 for National Aeronautics & Space Administration, Langley Research Center.
- [13] E. H. Newman and R. J. Marhefka, "An overview of MM and UTD methods at The Ohio State University," *Proc. IEEE*, vol. 77, pp. 700-708, May 1989.
- [14] P. Y. Ufimtsev, "Method of edge waves in the physical theory of diffraction," Tech. Rep. Document ID No. FTD-HC-23-259-71, Air Force Systems Command Foreign Tech. Div., 1971. (Translation from the Russian "Method Krayevykh voin v fizicheskoy teorii difraktsii," Soviet Radio Publication House, Moscow, 1962).

- [15] J. B. Keller, "Geometrical theory of diffraction," *J. Opt. Soc. of America*, vol. 52, pp. 116-130, Feb. 1962.
- [16] R. G. Kouyoumjian and P. H. Pathak, "A uniform geometrical theory of diffraction for an edge in a perfectly conducting surface," *Proc. IEEE*, vol. 62, pp. 1448-1461, 1974.
- [17] C. E. Ryan, Jr. and L. Peters, Jr., "Evaluation of edge-diffracted fields including equivalent currents for the caustic regions," *IEEE Trans. Antennas Propagat.*, vol. AP-7, pp. 292-299, 1969.
- [18] A. Michaeli, "Equivalent edge currents for arbitrary aspects of observation," *IEEE Trans. Antennas Propagat.*, vol. AP-32, pp. 252-258, 1984.
- [19] K. M. Mitzner, "Incremental length diffraction coefficients," Tech. Rep. No. AFAL-TR-73-296, Northrop Corp., Aircraft Division, Apr. 1974.
- [20] E. F. Knott, "The relationship between Mitzner's ILDC and Michaeli's equivalent currents," *IEEE Trans. Antennas Propagat.*, vol. AP-33, pp. 112-114, 1985.
- [21] P. Y. Ufimtsev and D. I. Butorin, "Explicit expressions for an acoustic edge wave scattered by an infinitesimal edge element," *Sov. Phys. Acous.*, vol. 34, pp. 283-287, July-August 1986.
- [22] P. Y. Ufimtsev, "A new mathematical formulation of the physical theory of diffraction,". Submitted for publication.
- [23] O. M. Buyukdura, R. J. Marhefka, and W. Ebihara, "Radar cross section studies, Phase III," Technical Report 716622-1, The Ohio State University ElectroScience Laboratory, Department of Electrical Engineering, Apr. 1986. Prepared under Contract No. NO429A-84-C-0363 for Pacific Missile Test Center.
- [24] W. B. Gordon, "Far-field approximations to the Kirchoff-Helmholtz representations of scattered fields," *IEEE Trans. Antennas Propagat.*, pp. 590-592, July 1975.

- [25] O. M. Buyukdura. Personal communication.
- [26] A. K. Dominek. Personal communication.
- [27] L. Krauss and L. M. Levine, "Diffraction by an elliptic cone," *Commun. Pure Appl. Math.*, vol. XIV, pp. 49-68, 1961.
- [28] J. Radlow, "Diffraction by a quarter plane," *Arch. Rational Mech. Anal.*, vol. 8, pp. 139-158, 1961.
- [29] J. Radlow, "Note on the diffraction at a corner," *Arch. Rational Mech. Anal.*, vol. 19, pp. 62-70, 1964.
- [30] R. S. Satterwhite and R. G. Kouyoumjian, "Electromagnetic diffraction by a perfectly conducting plane angular section," Tech. Rep. 2183-2, The Ohio State University ElectroScience Laboratory, Department of Electrical Engineering, 1970.
- [31] R. G. Kouyoumjian, P. H. Pathak, and W. D. Burnside, "A uniform GTD for the diffraction by edges, vertices and convex surfaces," in *Theoretical Methods for Determining the Interaction of Electromagnetic Waves with Structures*, (J. K. Skwirzynski, ed.), pp. 497-561, Sijthoff and Noordhoff, 1981.
- [32] O. M. Buyukdura, *Radiation from Sources and Scatterers Near the Edge of a Perfectly Conducting Wedge*. PhD thesis, Ohio State University, Department of Electrical Engineering, 1984.
- [33] R. F. Harrington, *Time-Harmonic Electromagnetic Fields*. McGraw-Hill, 1961.
- [34] L. W. Pearson, "The electromagnetic edge wave due to a point source of current radiating in the presence of a conducting wedge," *IEEE Trans. Antennas Propagat.*, vol. 34, pp. 1125-1132, Sep. 1986.
- [35] D. S. Jones and M. Kline, "Asymptotic expansion of multiple integrals and the method of stationary phase," *J. Math. Phys.*, vol. 37, pp. 1-28, 1958.

- [36] P. H. Pathak and R. G. Kouyoumjian, "A dyadic diffraction coefficient for a perfectly conducting wedge," Technical Report 2183-4, The Ohio State University ElectroScience Laboratory, Department of Electrical Engineering, 1970.
- [37] A. Dominek, J. D. Young, and S. Scarborough. Personal Communication.
- [38] R. J. Marhefka, "Computer code for radar cross section of convex plate and cone frustrum structures," Tech. Rep., The Ohio State University ElectroScience Laboratory, Department of Electrical Engineering, 1986.
- [39] A. Michaeli, "Equivalent currents for second-order diffraction by the edges of perfectly conducting polygonal surfaces," *IEEE Trans. Antennas Propagat.*, vol. AP-35, pp. 183-190, 1987.
- [40] R. H. Schafer and R. G. Kouyoumjian, "Higher order terms in the saddle point approximation," *Proc. IEEE*, vol. 55, no. 8, pp. 1496-1497, 1967.
- [41] L. B. Felsen and N. Marcuvitz, *Radiation and Scattering of Waves*. Englewood Cliffs, NJ: Prentice-Hall, Inc., 1973.
- [42] I. S. Gradshteyn and I. M. Ryzhik, *Table of Integral, Series, and Products*. Academic Press, Inc., 1980.